

MEMS 3-D SCAN MIRROR FOR AN ENDOSCOPIC CONFOCAL MICROSCOPE

by

Yuhe Shao

A dissertation submitted in partial fulfillment
of the requirements for the degree

of

Doctor of Philosophy

in

Engineering

MONTANA STATE UNIVERSITY
Bozeman, Montana

November, 2005

©COPYRIGHT

by

Yuhe Shao

2005

All Rights Reserved

APPROVAL

of a dissertation submitted by

Yuhe Shao

This dissertation has been read by each member of the dissertation committee and has been found to be satisfactory regarding content, English usage, format, citations, bibliographic style, and consistency, and is ready for submission to the College of Graduate Studies.

Dr. David L. Dickensheets

Approved for the Department of Electrical and Computer Engineering

Dr. James N. Peterson

Approved for the College of Graduate Studies

Dr. Joseph J. Fedock

STATEMENT OF PERMISSION TO USE

In presenting this dissertation in partial fulfillment of the requirements for a doctoral degree at Montana State University, I agree that the Library shall make it available to borrowers under rules of the Library. I further agree that copying of this dissertation is allowable only for scholarly purposes, consistent with “fair use” as prescribed in the U.S. Copyright Law. Requests for extensive copying or reproduction of this dissertation should be referred to ProQuest Information and Learning, 300 North Zeeb Road, Ann Arbor, Michigan 48106, to whom I have granted “the exclusive right to reproduce and distribute my dissertation in and from microform along with the non-exclusive right to reproduce and distribute my abstract in any format in whole or in part.”

Yuhe Shao

November 14, 2005

ACKNOWLEDGEMENTS

First and foremost, I would like to express my sincere thanks to my advisor, Dr. David Dickensheets. In the last four years, I benefited so much from his guidance, support, discussion and scientific insight. The most important thing I learned from him is how to deal with challenges in research, to solve them and go on. Without his encouragement and guidance, successful completion of this project would be unimaginable.

I would like to thank Dr. Joseph Shaw, Dr. Todd Kaiser and Dr. Ross Snider for serving on my advisory committee and for their advice. I also thank them for offering interesting classes. I would also thank Dr. Dennis Aig for being my CGS representative.

I would like to thank my friends and colleagues for their assistance and discussion while I have been working on this project. Many thanks to Phil Himmer, Jeff Lutzenberger, Nabil El Ferradi and Marshall Overcast. Especial thanks to Phil. His mastery of microfabrication skills made working in the cleanroom full of fun.

Most importantly, I am grateful to my parents, my wife and my sister, for their love, care and support whenever and wherever.

TABLE OF CONTENTS

1. INTRODUCTION	1
MEMS Scanners	2
Deformable Membrane Mirrors	3
MEMS 3-D Scan Mirror	5
Target Applications of the 3-D Mirror	6
2. DESIGN OF THE MEMS 3-D MIRROR	8
Architecture Design	8
Torsional Plate Architecture.....	9
Deformable Membrane Architecture.....	12
Target Specifications.....	13
Mechanical Design for Biaxial Scanning.....	15
Circular Torsional Plate Model for Uniaxial Scanning.....	15
Device Mechanical Model for Biaxial Scanning	18
Torsion Behavior Analysis Using the Device Mechanical Model	21
Cross Coupling of Biaxial Scanning.....	26
Comments.....	27
Mechanical Design for the Deformable Membrane.....	28
Mechanical Plate Theory.....	29
Finite Element Analysis (FEA)	32
Design Parameters of the Deformable Membrane	33
Dynamic Distortion of the Deformable Membrane	36
Optical Issues of the Deformable Membrane.....	37
Wavefront Aberration Theory	38
On-axis Imaging.....	40
3. FABRICATION OF THE MEMS 3-D MIRROR.....	42
Introduction to Silicon Micromachining Technology.....	42
Modified Surface Micromachining	45
Design of Photo Masks	46
Masks for a Single Mirror	46
Masks for Batch Fabrication of Mirrors on 4-inch Wafers	49
Batch Fabrication Process.....	51
Post-fabrication Release Process.....	57
4. CHARACTERIZATION OF THE MEMS 3-D MIRROR	60
Characterization of the Torsional Plate.....	60

TABLE OF CONTENTS – CONTINUED

Drive Electrodes.....	61
Method of Measuring Angular Displacement.....	62
Dependence of Resonant Frequency on DC Bias	63
Frequency Response.....	65
One-sided DC Drive.....	66
Quasi-static Scan.....	67
Resonant Scan	69
Simultaneous Biaxial Scanning.....	71
Deriving Mechanical Parameters from Measured Torsion Behavior.....	73
Summary	77
Characterization of the Deformable Membrane.....	77
Imaging Interferometer	78
Phase-shift Interferometry.....	80
Membrane Deflection Measurement.....	81
Spherical Aberration Measurement.....	83
Initial Shape of the Membrane	84
Lateral and Depth Resolutions of the 3-D Mirror.....	85
Lateral Resolution	86
Depth Resolution.....	86
Three-Dimensional Beam Position Demonstration	88
 5. CONFOCAL IMAGING USING THE 3-D MIRROR.....	 91
Introduction to Confocal Laser Scanning Microscopy	91
Tabletop Confocal Microscope Using the 3-D Mirror.....	94
Imaging Performance Calculation.....	95
Imaging Experiment.....	97
Incorporate the 3-D Mirror into a Miniature Confocal Microscope	99
Micro Objective Lens.....	99
Imaging Experiment.....	101
 6. CONCLUSION.....	 104
Summary of the 3-D Mirror Performance.....	104
Future Work	106
Design and Process Variations for Mirror Performance Improvement.....	106
Packaging of the Endoscopic Confocal Microscope.....	107
Potential Applications	110
 REFERENCES CITED.....	 111

LIST OF TABLES

Table	Page
2-1. Target mechanical and optical specifications of the 3-D mirror	14
2-2. Material properties of silicon and silicon nitride.....	18
2-3. Geometrical dimensions of the 3-D mirror.....	19
2-4. Material and geometrical parameters and affected performance characteristics.....	29
2-5. Material properties of silicon nitride	33
2-6. Design parameters of the deformable membrane	33
2-7. Primary (Seidel) aberrations.....	39
4-1. Measured Q-factors of the inner and outer scanning axes.....	66
4-2. Dependence of torsion behavior on mechanical parameters	74
4-3. Experimental and theoretical values of the mechanical parameters.....	75
5-1. Comparison of conventional and confocal microscopes	93
5-2. Specifications of the four elements of the objective lens	100

LIST OF FIGURES

Figure	Page
1-1. Schematic of the MSU endoscopic confocal laser scanning microscope.....	6
2-1. 3-D mirror concept	9
2-2. Architecture of the 3-D mirror.....	10
2-3. Deformable membrane with different perimeters	13
2-4. Circular plate rotating about the y-axis	15
2-5. Illustration of the mirror dimensions.....	19
2-6. Dependence of resonant frequency on silicon nitride film thickness.....	22
2-7. Dependence of resonant frequency on hinge width.....	23
2-8. Dependence of resonant frequency on hinge length.....	23
2-9. Dependence of resonant frequency on DC bias.....	23
2-10. Angular displacement versus one-sided DC voltage.....	24
2-11. Angular displacement versus differential voltage	25
2-12. Cross coupling effect on the inner axis	27
2-13. Effect of boundary condition on surface shape	31
2-14. Effect of initial stress on surface shape	31
2-15. Comparison of membrane deflections of two silicon nitride recipes	35
2-16. Influence of silicon nitride film thickness on membrane deflection	36
2-17. Coordinate system used to describe wavefront aberrations.....	39
3-1. Process steps to create a structural layer	43

LIST OF FIGURES – CONTINUED

3-2. Modified surface micromachining process for creating a cavity of variable depth	46
3-3. Photo masks of the 3-D mirror	49
3-4. Standard 4-inch photo mask layout	50
3-5. Fabrication process flow of the 3-D mirror	52
3-6. Scanning electron micrographs of a released 3-D mirror	59
4-1. Four-quadrant drive electrodes for biaxial scanning	61
4-2. Setup for measuring angular displacements	62
4-3. Dependence of resonant frequency on DC bias.....	63
4-4. Frequency response measurement.....	65
4-5. Tilt angle versus one-sided DC voltage.....	66
4-6. Peak-to-peak mechanical scan angle versus differential voltage amplitude at quasi-static scan.....	67
4-7. Illustration of linearization of two-sided drive	68
4-8. Peak-to-peak mechanical scan angle versus differential voltage amplitude at resonant scan	70
4-9. Rectangular and distorted scan patterns	71
4-10. Simultaneously biaxial scan	72
4-11. Optical profilometer setup using a Mirau interferometer objective lens.....	79
4-12. Schematic of the Mirau interferometer.....	79
4-13. Surface interference images.....	82
4-14. Surface line-profiles of the deformable membrane	82

LIST OF FIGURES – CONTINUED

4-15. Membrane deflection/focal length versus actuation voltage	83
4-16. Optical spherical aberration with uniform loading.....	84
4-17. Initial surface shape of the membrane	85
4-18. Setup for testing biaxial scanning with focus control.....	88
4-19. Lissajous scan patterns	89
5-1. Optical arrangements of conventional and confocal microscopes	92
5-2. Tabletop confocal microscope using the 3-D mirror as the beam scanning and focus control device.....	94
5-3. Images taken with the CLSM	97
5-4. Images of a grating with 50 μm high steps taken with the CLSM	98
5-5. Four-element 0.4 NA, 4X, achromatic, water immersion micro objective lens.....	99
5-6. Demonstration miniature confocal microscope.....	102
5-7. Images taken with the miniature confocal microscope	103
6-1. Rendering of the 3-D mirror and the ferrule/carrier	108
6-2. A ferrule with gold electrodes and traces	108
6-3. Current and new photo masks for patterning ferrules	109

ABSTRACT

Optical MEMS is at a very exciting stage and has become an enabling technology for a variety of applications in telecommunications and high-resolution display and imaging. Among many novel MEMS devices, MEMS scanners and deformable membrane mirrors are especially useful for scanned-beam imaging systems. MEMS scanners are usually used for laser beam scanning. Deformable mirrors provide an approach to modify the optical wavefront adaptively. In optical microsystems, packaging is often a critical part of the system design. Combining functionalities at a single device can reduce complexity of the system. Biaxial beam scanning and focus control are combined together in the MEMS 3-D scan mirror. The mirror surface is made of a gold-coated silicon nitride deformable membrane and works as a positive lens of variable focal length. The membrane sits on a torsional plate that can scan about two orthogonal axes. This architecture is able to move the focus of a laser beam throughout a three-dimensional space with a single optical surface. The overall size of the 3-D mirror is 1.5 mm with a usable optical aperture of 0.7 mm. Both the inner and outer scanning axes achieved more than 5° zero-to-peak mechanical scan angles; the deformable membrane achieved a maximum center displacement of more than $3.7 \mu\text{m}$, corresponding to an adjustable focal length from infinity to approximately 8 mm. For a confocal laser scanning microscope with illumination wavelength at 500 nm, they provide $N_x = N_y = 488$ resolvable spots for lateral resolution, and $N_z = 32$ depth-of-focus distances for depth resolution. To drive the 3-D mirror, the inner axis is operated near resonance (~ 650 Hz); and the outer axis quasi-statically. Operating the outer axis at 2 Hz provides a line resolution of 325 lines/frame at a refresh rate of 2 frames/second. The performance of the 3-D mirror is well matched to the intended application of endoscopic confocal microscopy, and similar devices could prove useful in a variety of optical microsystems needing beam scanning and focus control. This dissertation describes the design, fabrication, characterization, imaging experiment and target applications of the MEMS 3-D scan mirror.

CHAPTER 1

INTRODUCTION

The field of optical MEMS (Micro-Electro-Mechanical Systems) and optical microsystems is at a very exciting and fast-growing stage. Optical MEMS has become an enabling technology for a variety of applications in telecommunication, high-resolution display and imaging. Among many novel MEMS devices, MEMS scanners used to re-direct an optical beam and deformable membrane mirrors used to focus an optical beam are especially useful for scanned-beam imaging systems. It is anticipated that the performance of silicon-based MEMS scanners will exceed that of traditional metal-based scanners due to better material properties of silicon. In addition, MEMS scanners allow more compact system design and lower the cost. Deformable membrane mirrors provide an intelligent approach to modify the optical wavefront arbitrarily, allowing corrections of time-variant and/or space-variant optical aberrations adaptively, which is referred to as adaptive optics. This dissertation describes a novel MEMS device, referred to as 3-D mirror, which is able to move the focus of a laser beam in three dimensions. The MEMS mirror is realized by incorporating a variable-focus deformable membrane mirror into a biaxial scanner. Optical microsystems needing both beam scanning and focus control will benefit from such a MEMS device.

MEMS Scanners

MEMS scanners have been developed for more than two decades and have become important building blocks for many optical microsystems. Scanned-beam display and imaging is one of many fields to which MEMS scanners can contribute. Well-known applications include laser-based display systems [1-3] and confocal laser scanning microscopes [4-6]. A variety of other applications can also benefit from MEMS scanners. They include optical disk read/write heads [7], bar-code readers [8], fiber-optic switches [9-11], optical cross-connects [12] and many other components for fiber-optic telecommunication systems.

A circular mirror of diameter D has a far-field diffraction-limited angular spot size $\sim \lambda/D$, thus a scan angle θ produces a number of resolvable spots of $K\theta D/\lambda$, where K is a constant determined by the system configuration. Therefore, the scan-angle-mirror-size-product (θD) can be regarded as a resolution figure of merit for MEMS scanners. In scanned-beam display and imaging systems, the horizontal and vertical scan frequencies determine the line scan rate and frame refresh rate. MEMS scanners have achieved a θD value of more than 9 deg-mm, and scan frequency about 20 kHz [2], which correspond to SVGA specifications (800x600 pixels, 60 Hz frame rate, 20 kHz horizontal frequency).

To date, steel-based mechanical scanners still have better performance than silicon-based MEMS scanners due to some engineering design tradeoffs and fabrication related issues that have not been understood and resolved completely. However, it is reasonable to believe that MEMS scanners will surpass traditional scanners because silicon has better mechanical properties than steel and allows for higher frequency and

resolution. In addition, MEMS technology offers low-cost, high-volume fabrication capability and allows biaxial scanner implementation.

Technologies used to build MEMS scanners include SOI (silicon on insulator), bulk micromachining [13, 14] and surface micromachining [15, 16]. Stiff mirrors made using SOI or bulk micromachining dominate over thin film mirrors made using surface micromachining because of much lower dynamic distortion at high scanning frequency.

Deformable Membrane Mirrors

Micromachined deformable membrane mirrors were developed for adaptive optics in recent years. A deformable mirror consists of a thin membrane suspended over an array of electrostatic electrodes. The membrane may be made of a layer of silicon nitride Si_nN_m deposited by LPCVD (low pressure chemical vapor deposition). In the simplest case, the membrane is coated with a thin layer of metal (e.g., aluminum, gold) to provide sufficient reflectance in the visible and infrared spectrums. Small size, quick response, and smooth modal response make deformable mirrors highly suitable for real-time correction of optical wavefront aberrations [17].

Successful real-time correction of atmospheric turbulence for a telescope was accomplished by using a deformable mirror [18]. The deformable mirror used here must be able to correct arbitrary wavefront aberration because atmospheric turbulence is time-variant and random; therefore it requires a large number of actuators and complex feedback control schemes.

For applications where wavefront aberration is not random, an optimization approach combined with a lookup table can be used. A wide-field aberration correction

for scanning optical microscopy was demonstrated based on this approach [19]. The scanning beam quality was individually optimized for each pixel and the optimal control parameters were stored in a lookup table. In the operation mode, the scanning beam was corrected on-the-fly, pixel by pixel, resulting in drastic improvement of the optical resolution over the whole field of view. Another example of the optimization approach was reported on a 1xN fiber-optic switch with a deformable membrane mirror used to improve coupling efficiency for each switch channel by pre-setting the mirror shape in accordance with the lookup table storing the optimal control parameters [20].

Deformable mirrors designed to modify the wavefront arbitrarily need a large number of degrees of freedom. On the other hand, mirrors designed for a few number of specific functions can reach a much simpler design. Silicon nitride membrane mirrors designed specifically for focus control were reported [21, 24]. Mirrors were fabricated by use of a modified surface micromachining process. Spherical aberration was minimized by emulating a simple support of circular boundary using a segmented perimeter in combination with two concentric actuation electrodes providing two degrees of freedom to control the mirror shape. The two-zone actuation is also useful for correcting residual spherical aberration in the system. These mirrors were demonstrated with clear apertures from 0.3 mm to 1.5 mm, with adjustable focal lengths from infinity to several millimeters while maintaining zero primary spherical aberration. Deformable membrane mirrors were also designed to correct the primary aberrations in scanned-beam systems. Mirrors achieved sufficient speed for on-the-fly correction; thus can significantly extend the diffraction-limited field of view [40].

MEMS 3-D Scan Mirror

Both beam scanning and focus control are important functions for many optical microsystems. So called three-dimensional fiber-optic switches have a different pathlength between fibers depending on which fiber is addressed [10]. A variable-focus element could allow optimization of the coupling efficiency for each configuration of the switch. A compact confocal laser scanning microscope was demonstrated using separate MEMS devices for beam scanning and focus control [5]. In that demonstration, fast x-y beam scanning was achieved with a biaxial scanner, while static and dynamic z-axis focus position control was provided by a parabolic deformable membrane mirror.

In optical microsystems, packaging is often a critical part of the system design. Alignment of multiple active MEMS elements adds complexity, size and cost. Combining functionalities at a single optical surface can reduce complexity of the system. Biaxial beam scanning and focus control are combined together in the MEMS 3-D scan mirror that is the focus of this research. This is the first combination of scanning and focus control in a single optical MEMS device. The optical reflecting surface is made of a gold-coated, low-stress silicon nitride deformable membrane, which is suspended on a torsional plate. The deformable membrane offers focus control, while the torsional plate provides biaxial scanning. This architecture is able to move the focus of a laser beam throughout a three-dimensional space with one single optical surface. The 3-D mirror technology potentially simplifies the system design and reaches more compact instrument size. It is anticipated that optical microsystems needing both beam scanning and focus control will benefit from such a novel technology.

Target Applications of the 3-D Mirror

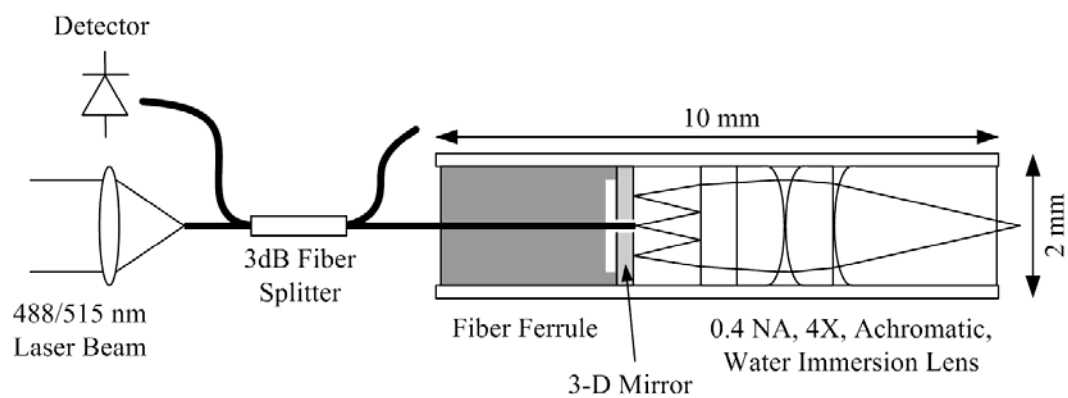


Figure 1-1. Schematic of the MSU endoscopic confocal laser scanning microscope.

The 3-D mirror technology is developed for optical microsystems needing both beam scanning and focus control, especially scanned-beam imaging systems. The 3-D mirror described in this dissertation is specifically designed for the MSU endoscopic confocal laser scanning microscope, which also serves as an example to demonstrate and study use of the 3-D mirror in optical microsystems. The endoscopic confocal microscope is designed to be only 2 mm in diameter and 10 mm in length, and can be inserted into a working channel of an endoscope, which delivers the microscope to the sample, instead of taking the sample from its natural environment to image on the microscope. *In-situ* imaging with the endoscopic microscope can visualize tissues in real-time at their natural environment, thus avoiding artifacts that can be caused by sampling, sectioning, mounting, and staining of tissues. This advantage renders the endoscopic microscope a very useful instrument for medical and biomedical applications.

The schematic of the MSU endoscopic confocal laser scanning microscope is illustrated in Figure 1-1. It is packaged within a cylindrical quartz tube. The 3-D mirror is mounted on the end of a fiber ferrule, and a small hole through the center of the 3-D mirror allows the illuminating beam from the single mode fiber to pass through it. 1.3 mm beyond the 3-D mirror, a small mirror patterned on the first element of the objective lens reflects the light beam back toward the 3-D mirror. After reflection from the 3-D mirror, the beam again propagates toward the end of the microscope, passing through the objective lens and focusing on a point of the sample. The back-scattered light retraces the optical path back to the fiber and is collected and detected to form an image, while the 3-D mirror is used to raster-scan the laser beam across the sample. Images of different layers of the sample can be obtained by changing the effective focal length of the 3-D mirror to construct a three-dimensional image. The endoscopic microscope is designed to achieve a sub-micron optical resolution with a field of view of 200 μm and a focus range of 0 – 100 μm from the last glass surface. The 3-D mirror, providing both biaxial beam scanning and focus control with one single optical surface, is the key technology making such a compact instrument possible.

The 3-D mirror described in this dissertation is specifically designed for the MSU endoscopic confocal microscope. However, similar devices could prove useful in a variety of optical microsystems needing beam pointing and focus control.

CHAPTER 2

DESIGN OF THE MEMS 3-D MIRROR

This chapter first illustrates the 3-D mirror concept and describes the device architecture and the desired device specifications. The conceptual design of the device architecture is based on silicon micromachining technology and potential applications of the 3-D mirror in optical microsystems. The overall size and the target specifications of the mirror described in this dissertation are representative for such kind of miniature devices used in optical microsystems, although they were chosen for a specific instrument – the MSU endoscopic confocal laser scanning microscope. Following the conceptual development, mechanical and optical analyses are discussed. These analyses are used to choose the detailed design parameters needed to achieve the target device specifications.

Architecture Design

The 3-D mirror concept is illustrated in Figure 2-1. The mirror surface is made of a gold-coated silicon nitride deformable membrane and works as a positive lens of variable focal length. The deformable membrane sits on a torsional plate that can scan about two orthogonal axes. Both bending of the deformable membrane and biaxial scanning are actuated electrostatically. The primary specifications of the deformable membrane are the maximum deflection and the surface shape. The maximum deflection corresponds to the adjustable range of the effective focal length while the surface shape

determines the amount of aberrations introduced to the optical wavefront by the mirror. For biaxial scanning, large mechanical scan angles and fast scanning speeds are desired because the optical resolutions and the refresh rate are determined by them when the 3-D mirror is used in a scanned-beam imaging system. The device architecture and the target specifications are proposed with these basic requirements in mind.

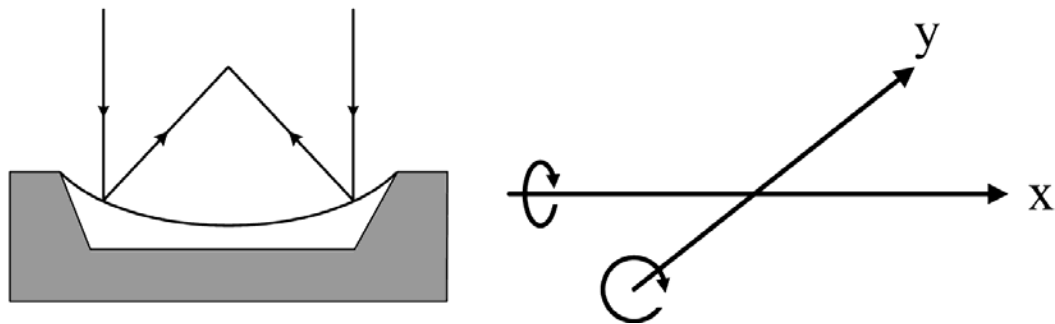


Figure 2-1. 3-D mirror concept. The mirror surface is made of a deformable membrane, which sits on a biaxial gimbal.

Torsional Plate Architecture

The architecture of the 3-D mirror is illustrated in Figure 2-2. The whole device measures 1500 μm in diameter, which is a representative size for such miniature devices used in optical microsystems, although it was tailored for a specific instrument – the MSU endoscopic confocal laser scanning microscope. The 3-D mirror mainly consists of three components – the inner mirror plate, the outer gimbal ring and the device frame. The inner plate is suspended on the outer ring with a pair of hinges on the vertical axis, and the outer ring is supported on the device frame with a second pair of hinges on the horizontal axis. The inner plate, the outer ring and the device frame are constructed from

single crystal silicon, while the hinges are made from low-stress LPCVD (low pressure chemical vapor deposition) silicon nitride. The silicon nitride hinges are flexible so the inner plate is free to rotate about the vertical axis (inner hinges) by itself, and to rotate about the horizontal axis (outer hinges) along with the outer gimbal ring.

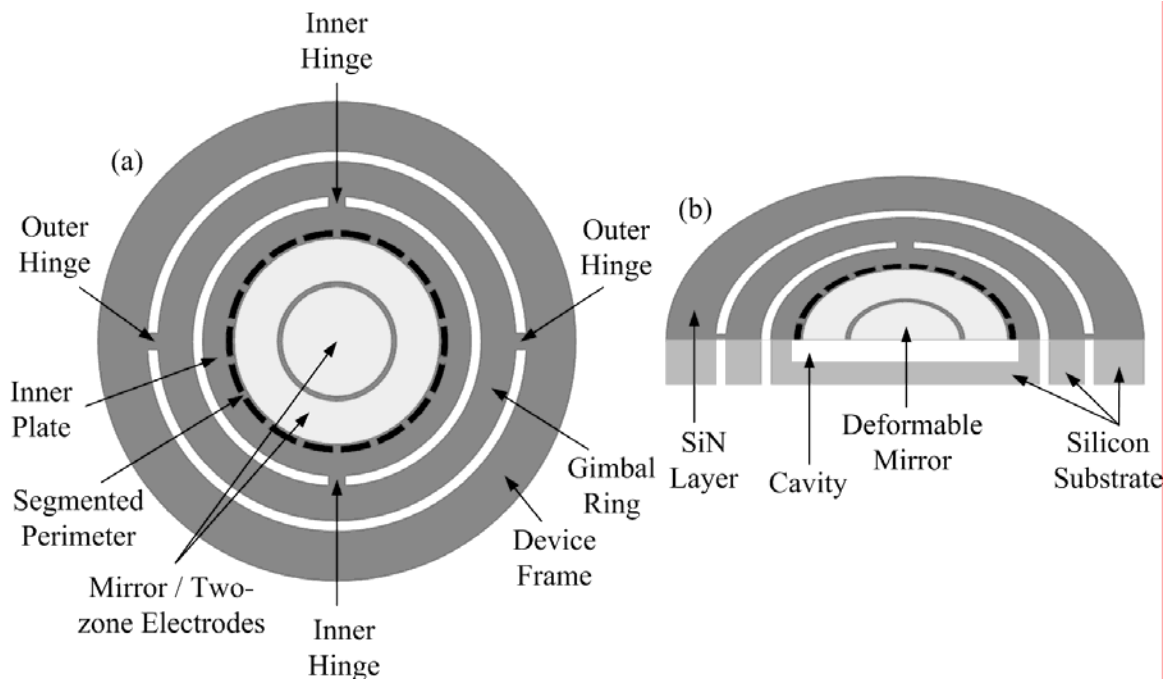


Figure 2-2. Architecture of the 3-D mirror. (a) Top view; (b) Cutaway view.

Biaxial scanning is driven electrostatically with the drive electrodes on the chip carrier beneath the 3-D mirror and the bulk silicon substrate serving as the counter electrode. The magnitude of the angular displacement results from balance between the electrostatic attractive force and the mechanical restoring force. It will be shown in the mechanical analysis section that the electrostatic force overwhelms the mechanical restoring force when the vertical displacement of the plate edge is beyond roughly one

third of the quiescent distance between the plate and the electrodes causing the plate to be in contact with the electrodes, which is referred to as snap-down. Given the maximum angular displacement of $\pm 5^\circ$ and the gimbal ring diameter of about 1 mm, the maximum edge displacement is approximately $(1000\mu\text{m}/2) \times (5^\circ / 180^\circ) \times \pi = 44\mu\text{m}$. To avoid snap-down, the distance between the mirror plate and the drive electrodes was designed to be 150 μm .

In addition to the maximum angular displacement, the scanning speed is another important specification. It is obvious that, when the 3-D mirror is used in a scanned-beam imaging system, the refresh rate is determined by the slow scan (about the outer axis) frequency, while the line resolution (number of lines per frame) is dependant on the ratio of the fast scan (about the inner axis) frequency to the slow scan frequency. The refresh rate and the line resolution can be expressed as the following equations if the fast scan is sinusoidal and the slow scan is driven by a sawtooth waveform.

$$\text{Refresh Rate} = \text{Slow Scan Frequency}$$

$$\text{Line Resolution} = \text{Fast Scan Frequency} / \text{Slow Scan Frequency}$$

For imaging applications at a refresh rate around 2 frames/second and with a resolution more than 300x300 pixels/frame, the slow scan frequency was designed to be 2 Hz and the fast scan frequency over 600 Hz. To lower the drive voltage, it is desirable to scan the inner axis at resonance, which requires the resonant frequency to be tailored to the operating frequency. Scanning about the inner axis is also near sinusoidal to maintain scanning stability and smoothness. The outer axis is driven quasi-statically and may

deviate from a sinusoidal scan if desired. A lower resonant frequency for the outer axis can yield lower-voltage actuation. However, a first resonance greater than 200 Hz will improve shock and vibration immunity and allow for more non-sinusoidal scan waveforms. Therefore a target resonance near 200 Hz was chosen for the outer axis.

Deformable Membrane Architecture

The deformable membrane on the inner plate is made of gold-coated low-stress LPCVD silicon nitride, with a cavity between it and the silicon plate, as illustrated in Figure 2-2 (b). Deformation is actuated electrostatically with two concentric annular gold electrodes patterned on top of the silicon nitride membrane, and the silicon plate providing the counter electrode. The gold layer also serves as the optical reflecting surface with a usable optical aperture of 700 μm in diameter, which was maximized for the overall device diameter of 1500 μm . The two-zone actuation electrodes provide two degrees of freedom to control the surface shape of the membrane, allowing for active control of the effective focal length and the residual spherical aberration.

The membrane boundary condition also plays a role in determining the surface shape. Mechanical plate theory indicates that a uniformly loaded membrane with a simply supported boundary achieves a more parabolic deflection than a membrane with a clamped boundary. The membrane is supported via strips of silicon nitride rather than a continuous ring to emulate a simply supported boundary. Finite-element analysis and experiments verify that two-zone actuation and segmenting of the perimeter can produce a parabolic surface throughout the focus range. Segmenting of the perimeter has the added benefit of reducing the actuation voltages required for a given deflection. Figure 2-

3 illustrates the continuous and segmented perimeters. The part inside the dashed circle is free-standing and deformable while the part outside the dashed circle is supported on the silicon plate.

The maximum center displacement of the membrane mirror was designed to be more than $3\ \mu\text{m}$ with a cavity about $10\ \mu\text{m}$ deep underneath it. The relationship of the focal length and the membrane deflection is given by $f_{mir} = D^2 / 16\delta$, where D is the diameter of the mirror and δ is the center displacement. For a mirror of $700\ \mu\text{m}$ diameter with a center displacement up to $3\ \mu\text{m}$, this provides a range of focal lengths from ∞ to $10\ \text{mm}$.

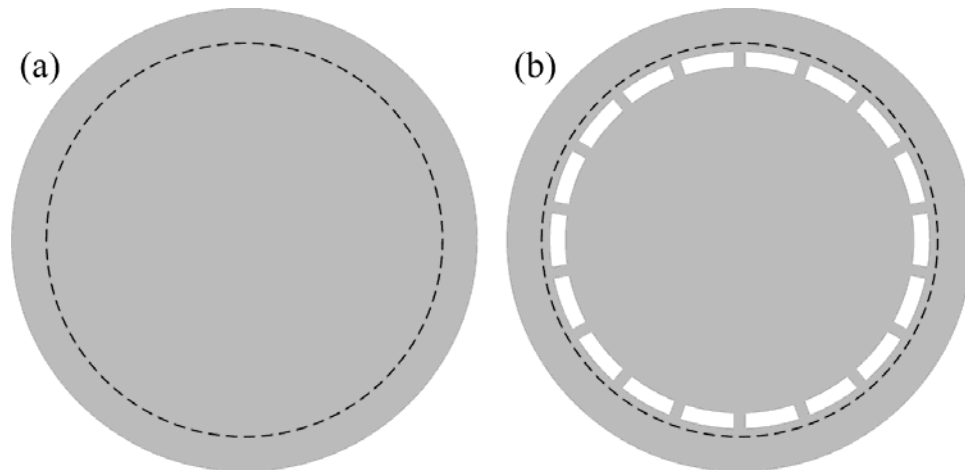


Figure 2-3. Deformable membrane with different perimeters. Dashed lines indicate extent of the cavity underneath the membrane. (a) Continuous perimeter; (b) Segmented perimeter.

Target Specifications

The target mechanical and optical specifications of the 3-D mirror are summarized in Table 2-1. As described in previous sections, they were designed along

with the device architecture according to the micromachining process and the requirements of proposed applications.

Table 2-1. Target mechanical and optical specifications of the 3-D mirror.

<p>Mirror Dimensions</p> <ul style="list-style-type: none"> – Overall device size (diameter) = 1500 μm – Useable optical aperture (diameter) = 700 μm
<p>Biaxial Scanning Specifications</p> <ul style="list-style-type: none"> – Mechanical scan angle $\theta_{\max} \geq \pm 5^\circ$, both axes (cavity $\sim 150 \mu\text{m}$). – Resonant frequency of the inner axis $f_i \geq 600 \text{ Hz}$ ($\pm 5\%$). – Resonant frequency of the outer axis $f_o \approx 200 \text{ Hz}$. – Scanning about the inner axis is near resonance to lower the drive voltage and is near sinusoidal. – Scanning about the outer axis is quasi-static ($\sim 2 \text{ Hz}$) and may deviate from a sinusoidal scan.
<p>Deformable Membrane Specifications</p> <ul style="list-style-type: none"> – Capable of 3-μm displacement at the membrane center thus providing a range of focal lengths from ∞ to 10 mm ($f_{\text{mir}} = D^2 / 16\delta$ where D is the usable aperture diameter of the mirror and δ is the center displacement). – Surface shape aberration (compared to a parabola) is less than $\lambda/20$ ($\lambda = 500 \text{ nm}$). – Two-zone actuation to provide ± 2 waves spherical aberration correction at mid-deflection, measured at 500 nm wavelength. – RMS roughness of the optical surface is less than 10 nm.

Mechanical Design for Biaxial Scanning

To construct mirrors that meet the target mechanical specifications, the influence of mechanical parameters on performance characteristics was investigated. Mechanical parameters depend on both material and geometrical properties. Material properties cannot be tailored arbitrarily because they are fixed by the choosing of materials and deposition processes used for constructing the device. On the other hand, geometrical parameters can be easily altered in the design phase. The detailed design parameters were determined by mechanical analysis in combination with micromachining process limitations, material properties and some practical concerns so that mirrors can be fabricated successfully and achieve the desired mechanical and optical performance.

Circular Torsional Plate Model for Uniaxial Scanning

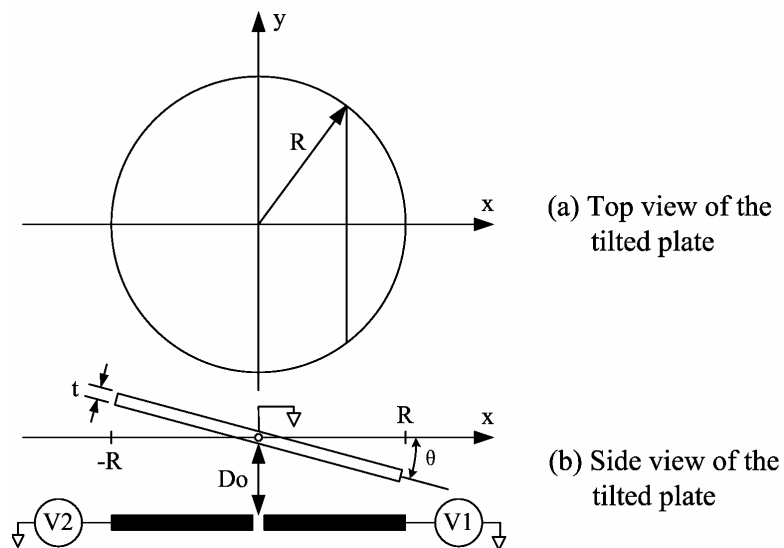


Figure 2-4. Circular plate rotating about the y-axis.

Following the work of Dickensheets Kino on the dynamic behavior of a rectangular torsional plate [4], the uniaxial dynamic behavior of the 3-D mirror is modeled as a circular torsional plate rotating about the y-axis, driven by two electrodes underneath it, as illustrated in Figure 2-4. The circular plate has a thickness of t and a radius of R and the quiescent distance between the plate and the electrodes is D_0 . The dynamic behavior of the plate is governed by the following second-order equation of motion (ignoring damping).

$$I \frac{d^2 \theta}{dt^2} = T_e - T_h \quad (2-1)$$

where $I = \pi \rho t R^4 / 4$ is the moment of inertia of the circular plate about the y-axis; T_e is the electrostatic torque driving the plate to rotate; and T_h is the mechanical restoring torque of the silicon nitride hinges.

The electrostatic torque is a nonlinear function of the drive voltages and the angular displacement θ , and can be expressed as $T_e = \int F(x) x dA$, with the approximation that the forces on the plate are normal to the drive electrodes. For small angular displacement ($\theta \rightarrow 0$), the electrostatic force per unit area is given by $F(x) = \varepsilon_0 V^2 / 2(D_0 - x\theta)^2$ and $dA = 2\sqrt{R^2 - x^2} dx$, where ε_0 is the permittivity constant in vacuum/air. The plate is driven by two electrodes V_1 and V_2 , covering full area of the plate, but separated along the y-axis. Considering the analysis above, the electrostatic torque reaches the following form.

$$T_e(V_1, V_2, \theta) = \varepsilon_0 \left[V_1^2 \int_0^R \frac{x \sqrt{R^2 - x^2}}{(D_0 - x\theta)^2} dx - V_2^2 \int_0^R \frac{x \sqrt{R^2 - x^2}}{(D_0 + x\theta)^2} dx \right] \quad (2-2)$$

The mechanical restoring torque is given by $T_h = 2K\theta$, in which the 2x factor accounts for the plate being suspended by a pair of identical hinges, and K is the spring constant depending on mechanical properties and dimensions of the hinges. For hinges with a rectangular cross section, it is given by [33]

$$K = G \frac{w\delta^3}{l} \left[\frac{1}{3} - \frac{0.21\delta}{w} \left(1 - \frac{\delta^4}{12w^4} \right) \right] \quad (2-3)$$

where G is the elastic modulus of the silicon nitride hinges in shear. It is related to Young's modulus E by Poisson's ratio ν according to $G = E/2(1+\nu)$. The parameters l , w and δ are the length, width and thickness of the hinges, respectively.

Because the electrostatic torque is proportional to the squares of the applied voltages, it is desirable to operate the device with a DC bias on the electrodes so that the voltages are unipolar and the mirror response is at the same frequency as the drive voltages rather than twice of that frequency. However, the presence of a DC bias will change the resonant frequency of the plate. This can be explored by setting $V_1 = V_2 = V_{DC}$ in equation (2-2), and expanding the resulting expression into a power series of θ as follows.

$$T_e(V_{DC}, \theta) = \frac{\pi\epsilon_0 R^4 V_{DC}^2}{4D_0^3} \theta + O(2) \quad (2-4)$$

where $O(2)$ is terms of second or higher orders of θ . Neglecting these nonlinear terms, the equation of motion becomes

$$I \frac{d^2\theta}{dt^2} = \left(\frac{\pi\epsilon_0 R^4 V_{DC}^2}{4D_0^3} - 2K \right) \theta \quad (2-5)$$

Thus the resonant frequency of the plate is given by

$$f_0 = \frac{1}{2\pi\sqrt{I}} \sqrt{2K - \frac{\pi\varepsilon_0 R^4}{4D_0^3} V_{DC}^2} \quad (2-6)$$

Device Mechanical Model for Biaxial Scanning

The circular torsional plate theory provides a starting point to study the torsion behavior of the 3-D mirror. To choose design parameters affecting the torsion behavior accurately, mechanical parameters including moments of inertia, electrostatic driving torques and mechanical restoring torques must be calculated for the actual device, which has a much more complicated architecture than a circular plate. Table 2-2 lists mechanical properties of the materials used for constructing the 3-D mirror. Table 2-3 lists the geometrical dimensions chosen to meet the biaxial scanning specifications, which were resulted from mechanical analysis of the device model in combination with micromachining process limitations and some practical concerns. Figure 2-5 illustrates definitions of the dimensions.

Table 2-2. Material properties of silicon and silicon nitride [42].

Density of Si	$\rho_{Si} = 2.33 \times 10^3 \text{ kg} / \text{m}^3$
Density of SiN	$\rho_{SiN} = 3.18 \times 10^3 \text{ kg} / \text{m}^3$
Poisson's ratio of SiN	$\nu_{SiN} = 0.24$
Young's modulus of SiN	$E_{SiN} = 2.60 \times 10^{11} \text{ Pa}$
Shear modulus of SiN	$G_{SiN} = 1.05 \times 10^{11} \text{ Pa}$
Note: $G = \frac{E}{2(1 + \nu)}$	

Table 2-3. Geometrical dimensions of the 3-D mirror.

Thickness of the Si plate	$T_{Si} = 30\ \mu m$
Thickness of the SiN film	$T_{SiN} = 1\ \mu m$
Depth of the cavity underneath the membrane	$D_{cav} = 10\ \mu m$
Radius of the cavity underneath the membrane	$R_{cav} = 373\ \mu m$
Radius of the inner mirror plate	$R_{ip} = 420\ \mu m$
Inside radius of the outer gimbal ring	$R_{opi} = 435\ \mu m$
Outside radius of the outer gimbal ring	$R_{opo} = 510\ \mu m$
Radius of the whole device	$R_{mir} = 750\ \mu m$
Width of the inner hinge	$W_{ih} = 10\ \mu m$
Length of the inner hinge	$L_{ih} = 18,23,28\ \mu m$
Width of the outer hinge	$W_{oh} = 10\ \mu m$
Length of the outer hinge	$L_{oh} = 80\ \mu m$
Distance from the mirror to the drive electrodes	$D_0 = 150\ \mu m$

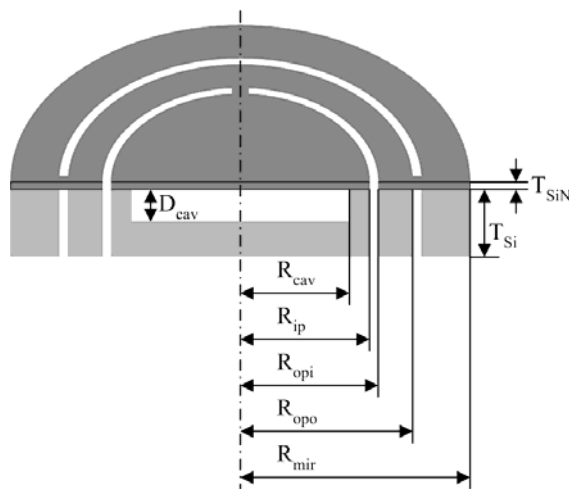


Figure 2-5. Illustration of the mirror dimensions.

Moment of Inertia. When considering rotation about the outer axis, the inner mirror plate and the outer gimbal ring are regarded as one single part and referred to as the outer plate.

$$\text{– Moment of inertia of the inner plate: } I_i = \frac{\pi}{4}(\rho_{Si}T_{Si} + \rho_{SiN}T_{SiN})R_{ip}^4 - \frac{\pi}{4}\rho_{Si}D_{cav}R_{cav}^4$$

$$\text{– Moment of inertia of the outer plate: } I_o = I_i + \frac{\pi}{4}(\rho_{Si}T_{Si} + \rho_{SiN}T_{SiN})(R_{opo}^4 - R_{opi}^4)$$

Electrostatic Torques. To simplify calculation of the electrostatic torque, a geometrical coefficient $C(R, \theta)$ is defined as follows. It is only dependant on the geometrical parameters, but not on the applied voltages. In the equations, voltage V_1 is applied to one half side of the inner plate (or the outer plate), while V_2 to the other side.

$$C(R, \theta) = \varepsilon_0 \int_0^R \frac{x\sqrt{R^2 - x^2}}{(D_0 - x\theta)^2} dx;$$

$$C_{i1}(\theta) = C(R_{ip}, \theta);$$

$$C_{o1}(\theta) = C_{i1}(\theta) + C(R_{opo}, \theta) - C(R_{opi}, \theta);$$

$$C_{i2}(\theta) = C(R_{ip}, -\theta);$$

$$C_{o2}(\theta) = C_{i2}(\theta) + C(R_{opo}, -\theta) - C(R_{opi}, -\theta).$$

$$\text{– Electrostatic torque on the inner plate: } T_{ie}(V_1, V_2, \theta) = V_1^2 C_{i1}(\theta) - V_2^2 C_{i2}(\theta)$$

$$\text{– Electrostatic torque on the outer plate: } T_{oe}(V_1, V_2, \theta) = V_1^2 C_{o1}(\theta) - V_2^2 C_{o2}(\theta)$$

Mechanical Restoring Torques. The spring constant is a function of the material properties and the hinge dimensions, while the restoring torque can be expressed as a linear function of the angular displacement.

$$K(T, W, L) = \frac{G_{SiN} WT^3}{L} \left[\frac{1}{3} - \frac{0.21T}{W} \left(1 - \frac{T^4}{12W^4} \right) \right]$$

– Restoring torque of the inner hinges: $T_{ih}(\theta) = 2K_i\theta = 2K(T_{SiN}, W_{ih}, L_{ih})\theta$

– Restoring torque of the outer hinges: $T_{oh}(\theta) = 2K_o\theta = 2K(T_{SiN}, W_{oh}, L_{oh})\theta$

Torsion Behavior Analysis Using the Device Mechanical Model

Mathematical models and equations have been developed to describe the torsion behavior of the 3-D mirror. They can be used to choose the optimum design parameters and predict the biaxial scanning performance. The material properties in Table 2-2 and the device dimensions in Table 2-3 will be used for plotting graphs in this section unless otherwise mentioned.

Resonant Frequencies. Resonant frequencies of the two orthogonal scanning axes are important characteristics and must meet the target specifications. Consider the resonant frequency of a torsional circular plate and the mechanical parameters calculated for the device model, the resonant frequencies of the device model can be expressed in the following equations for the inner and outer axes, respectively.

– Inner axis:
$$f_i = \frac{1}{2\pi\sqrt{I_i}} \sqrt{2K_i - \frac{\pi\varepsilon_0 R_{ip}^4}{4D_0^3} V_{DC}^2}$$

– Outer axis:
$$f_o = \frac{1}{2\pi\sqrt{I_o}} \sqrt{2K_o - \frac{\pi\varepsilon_0 (R_{opo}^4 - R_{opi}^4 + R_{ip}^4)}{4D_0^3} V_{DC}^2}$$

In these equations, the spring constants K_i and K_o are dependent on the hinge dimensions, which suggests that the target resonant frequencies can be achieved by

choosing appropriate hinge dimensions. Figures 2-6 ~ 2-8 plot the dependence of the resonant frequency on the hinge thickness, width and length, respectively, for the situation of no DC bias applied ($V_{DC} = 0$ volts). For plotting, parameters other than the variable were set to the values listed in Table 2-2 and Table 2-3. Along with fabrication process limitations and some practical concerns, these plots were used to choose the optimum hinge dimensions to meet the target device specifications.

In real operation, a DC bias of about 150 volts is applied to the 3-D mirror, which lowers the resonant frequencies compared to the situation of no DC bias. This issue must also be considered in designing the resonant frequencies. Figure 2-9 plots dependence of the resonant frequency on the DC bias for the inner and outer axes, respectively.

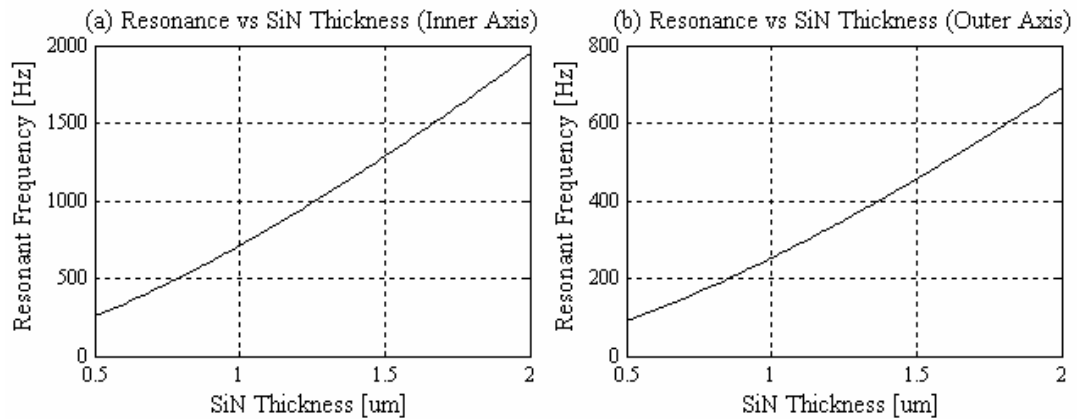


Figure 2-6. Dependence of resonant frequency on silicon nitride film thickness. $W_{ih} = 10 \mu\text{m}$, $L_{ih} = 23 \mu\text{m}$, $W_{oh} = 10 \mu\text{m}$, $L_{oh} = 80 \mu\text{m}$.

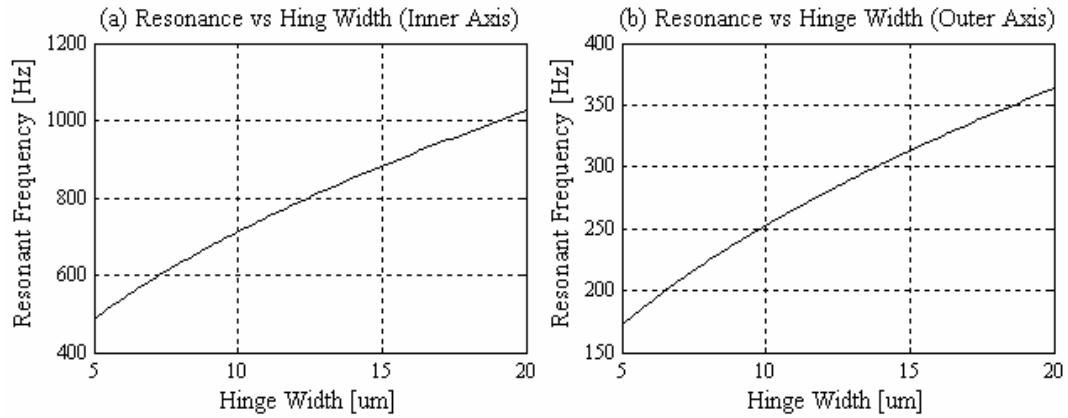


Figure 2-7. Dependence of resonant frequency on hinge width. $T_{SiN} = 1 \mu\text{m}$, $L_{ih} = 23 \mu\text{m}$, $L_{oh} = 80 \mu\text{m}$.

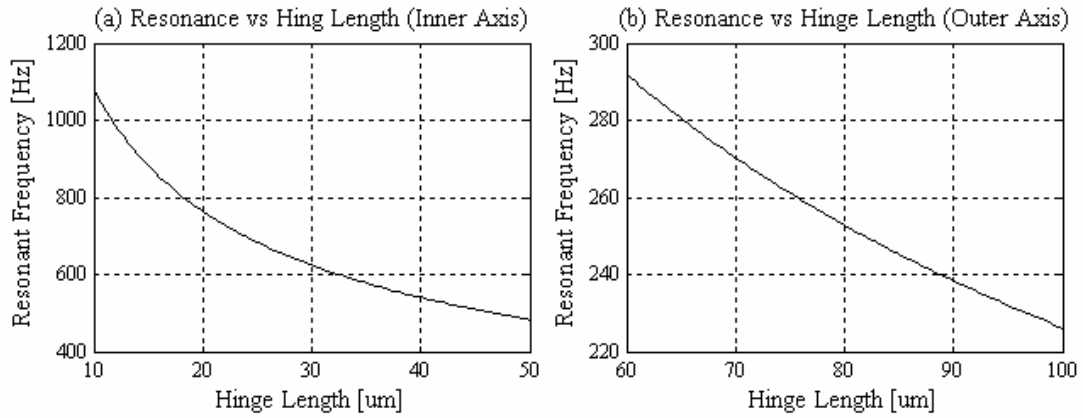


Figure 2-8. Dependence of resonant frequency on hinge length. $T_{SiN} = 1 \mu\text{m}$, $W_{ih} = 10 \mu\text{m}$, $W_{oh} = 10 \mu\text{m}$.

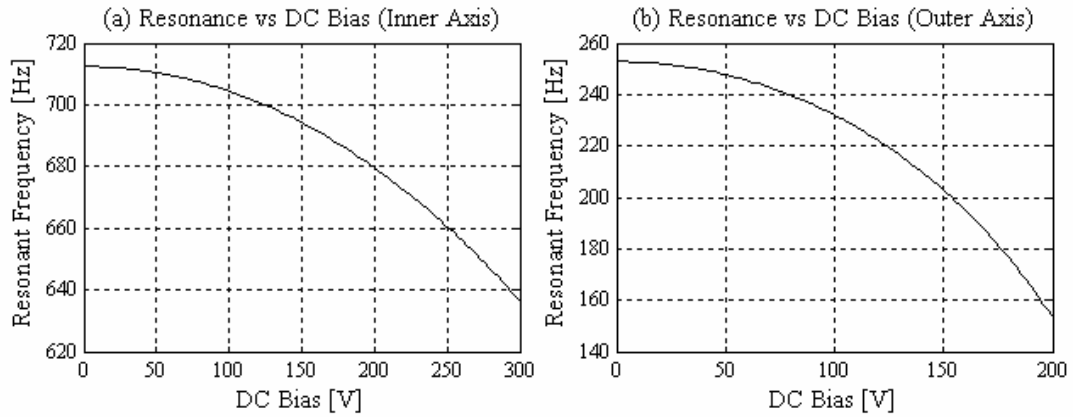


Figure 2-9. Dependence of resonant frequency on DC bias. $T_{SiN} = 1 \mu\text{m}$, $W_{ih} = 10 \mu\text{m}$, $L_{ih} = 23 \mu\text{m}$, $W_{oh} = 10 \mu\text{m}$, $L_{oh} = 80 \mu\text{m}$.

Static Response. For static or quasi-static operation, $d^2\theta/dt^2 \approx 0$, the equation of motion degrades to $T_e - T_h = 0$, which can be used to solve for the relationship between the drive voltages and the angular displacement. In the simplest case, the mirror can be driven by a DC voltage applied to half side of it. The relationship of the one-sided DC voltage and the angular displacement is given in the following equations for the inner and outer axes, respectively. Figure 2-10 plots these two equations. The quadratic-like relationship is due to the electrostatic attractive torque being proportional to the square of the drive voltage. The turn-around point in Figure 2-10 (b) represents snap-down, indicating that the mirror should not be driven beyond that point.

– Inner Axis: $V_i(\theta) = \sqrt{T_{ih}(\theta)/C_{il}(\theta)}$

– Outer Axis: $V_o(\theta) = \sqrt{T_{oh}(\theta)/C_{ol}(\theta)}$

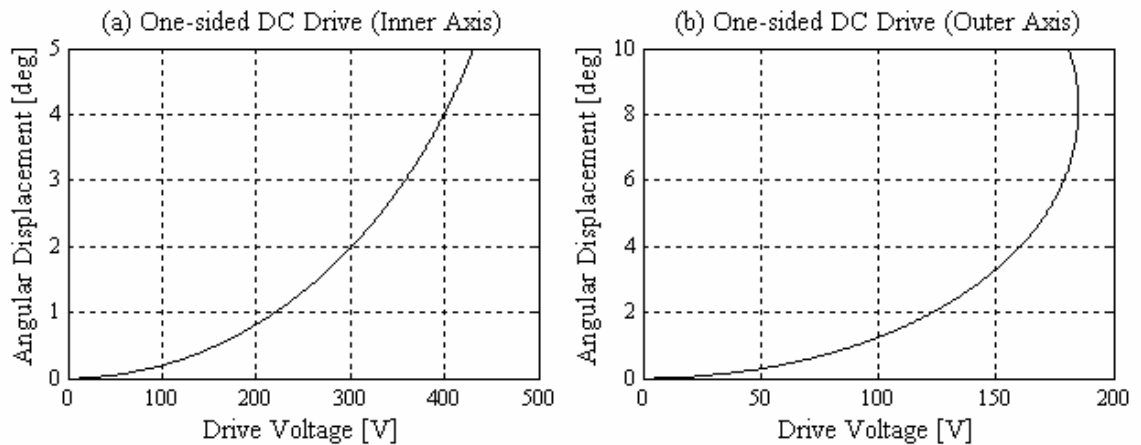


Figure 2-10. Angular displacement versus one-sided DC voltage.

In real operation, the 3-D mirror is driven with a DC bias plus a differential voltage applied to both sides of the mirror. The drive voltages have the following forms.

$$V_1 = V_{DC} + V_{diff}; \quad V_2 = V_{DC} - V_{diff}.$$

The relationship of the differential voltage and the angular displacement is given in the following equations for the inner and outer axes, respectively.

– Inner Axis:

$$V_{diff}(V_{DC}, \theta) = \frac{\sqrt{4V_{DC}^2 C_{i1}(\theta)C_{i2}(\theta) + T_{ih}(\theta)(C_{i1}(\theta) - C_{i2}(\theta))} - V_{DC}(C_{i1}(\theta) + C_{i2}(\theta))}{C_{i1}(\theta) - C_{i2}(\theta)}$$

– Outer Axis:

$$V_{diff}(V_{DC}, \theta) = \frac{\sqrt{4V_{DC}^2 C_{o1}(\theta)C_{o2}(\theta) + T_{oh}(\theta)(C_{o1}(\theta) - C_{o2}(\theta))} - V_{DC}(C_{o1}(\theta) + C_{o2}(\theta))}{C_{o1}(\theta) - C_{o2}(\theta)}$$

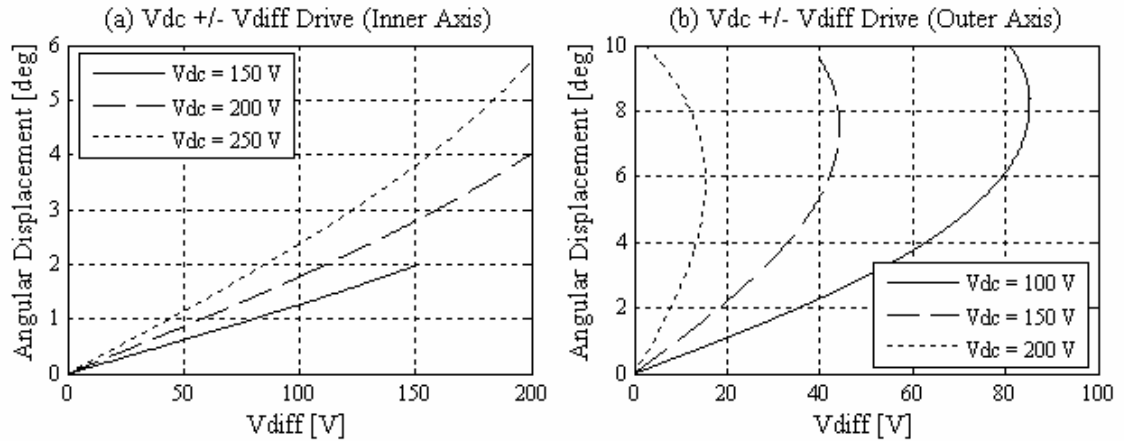


Figure 2-11. Angular displacement versus differential voltage.

Figure 2-11 plots these two equations for a set of different DC bias voltages. Again, the turn-around point in Figure 2-11 (b) represents snap-down, indicating that the mirror should not be driven beyond that point. It can be seen that, compared to one-sided drive, two-sided drive produces a very linear relationship between the angular

displacement and the differential voltage if the angular displacement is not too close to the snap-down point. The linearization results from the symmetric nature of the two-sided drive and is a desirable operating characteristic.

Figure 2-10 and Figure 2-11 suggest that, in static operation, the outer axis can rotate more than 5° with the drive voltages in a reasonable range; however, the required voltage is very high for the inner axis to reach 5° angular displacement. Fortunately, in practice, the inner axis is driven at resonance, which will lower the drive voltage down to a reasonable range.

Cross Coupling of Biaxial Scanning

In previous sections, the inner and outer axes were considered separately. However, in real operation, the two orthogonal axes are driven simultaneously. Biaxial scanning has some cross coupling between the two axes due to nonlinear dependence of the angular displacement on the mirror-electrodes distance and the drive voltages. This effect can cause the inner axis to achieve a larger angular displacement with a given drive voltage when the outer axis is rotated. A simplified model as follows can be used to estimate the magnitude of the cross coupling effect.

$$C(\theta_x, \theta_y) = \epsilon_0 \int_0^R \int_{-\pi/2}^{\pi/2} \frac{r^2 \cos(\varphi)}{2(D_0 - \theta_x r \cos(\varphi) - \theta_y r \sin(\varphi))^2} d\varphi dr ;$$

$$T_{ie}(V_{DC}, V_{diff}, \theta_x, \theta_y) = (V_{DC} + V_{diff})^2 C(\theta_x, \theta_y) - (V_{DC} - V_{diff})^2 C(-\theta_x, \theta_y) .$$

In the equation, T_{ie} is the electrostatic torque to rotate the inner axis, achieved with a DC bias V_{DC} plus a differential voltage V_{diff} as described in the last section, with the exception that the outer axis has an angular displacement of θ_y . Figure 2-12 plots the

angular displacement of the inner axis versus the differential voltage V_{diff} with $D_0 = 150$ μm and $V_{DC} = 150$ volts for the two cases of the outer axis having 0° and 5° angular displacements, respectively. It can be seen that the inner axis achieves angular displacements 4.6% larger when the outer axis has a 5° angular displacement. In biaxial scanning, this effect distorts the scan pattern from an ideal rectangle. To obtain an ideally rectangular scan pattern, the differential voltage can be adjusted according to the angular displacement of the outer axis to balance out the cross coupling effect.

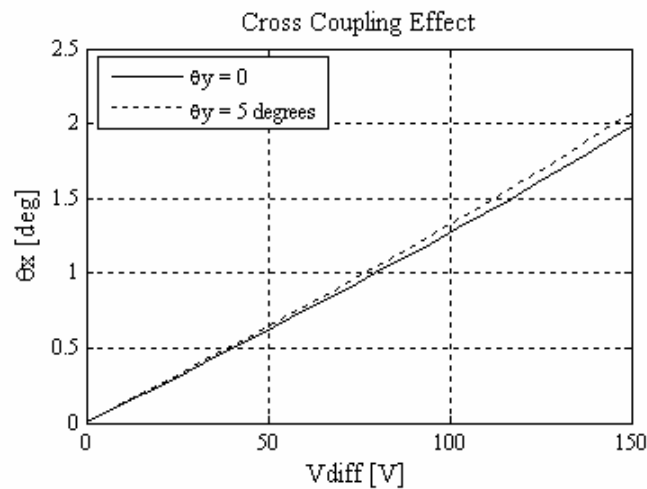


Figure 2-12. Cross coupling effect on the inner axis. $D_0 = 150$ μm , $V_{DC} = 150$ V.

Comments

One comment must be given here is that the calculated device specifications are obtained from an idealized mathematical model and a set of chosen parameters. On the other hand, the microfabrication process has some imperfect aspects, such as variation in material properties, variation in film thickness, under-cutting, etc. All of these factors can

make the actual device specifications deviate from the predicted ones. Therefore, the mechanical model provides a clue to estimate effects of the design parameters on the device performance rather than giving quantitative results. The actual device specifications must be measured by experimental characterization. In addition, it is necessary to introduce some variations to the design parameters to balance out the material and process variations and ensure that the final specifications of some devices will fall into the desired range. Based on this consideration, mirrors were built with three different values for the inner hinge length to achieve the target resonant frequency of the inner axis. The hinge thickness and width also affect the resonant frequency but there are more constraints on adjusting them than the length. Film thickness affects both deformable membrane and torsional hinges, thus it was chosen to meet requirements from both of them. The hinge width may be adjusted. However, the minimal width is limited by electrical traces overlying on the hinges.

Mechanical Design for the Deformable Membrane

A mirror surface with a variable quadratic (parabolic) curvature can provide focus control and correct field curvature while quartic and higher-order curvatures introduce spherical aberration to the wavefront. However, a controlled quartic curvature may be used to balance out spherical aberration already existing in the wavefront. In addition to surface curvatures, other performance characteristics to be considered include focal range, usable optical aperture, required actuation voltage, initial (zero voltage) curvature, etc. To construct deformable membranes that will achieve the desired performance, mechanical plate theory and finite element analysis were used to examine material and geometrical

parameters for their effects on the surface shape and other performance characteristics. Table 2-4 lists the examined material and geometrical parameters along with the affected performance characteristics of the deformable membrane. In addition to theoretical analysis, previous experimental results were also imported for choosing the optimum design parameters.

Table 2-4. Material and geometrical parameters and affected performance characteristics.

Material and geometrical parameters	Affected performance characteristics
Initial stress of silicon nitride film	Actuation voltage, spherical aberration.
Thickness of silicon nitride film	Actuation voltage, spherical aberration.
Diameter of deformable membrane	Actuation voltage, maximum usable pupil size.
Cavity depth	Actuation voltage, focal range.
Perimeter segmentation	Actuation voltage, spherical aberration.
Zonal annular electrodes	Spherical aberration.
Sacrificial PSG pad thickness	Initial (zero voltage) curvature due to edge effects.

Mechanical Plate Theory

The deformable membrane of the 3-D mirror can be modeled as a circular mechanical plate. The deflection of a circular plate with a clamped boundary was studied thoroughly by Sheplak and Dugundji [23]. Himmer extended this work for a simply supported boundary [22]. To guide design for the deformable membrane, the work of Sheplak, Dugundji and Himmer is summarized here briefly. For generality and convenience, Sheplak and Dugundji introduced two nondimensional parameters – the stress parameter k and the loading parameter P , defined as

$$k = \frac{a}{h} \sqrt{\frac{12(1-\nu^2)\sigma_0}{E}} \quad \text{and} \quad P = \frac{p_z a^4}{Eh^4},$$

where a and h are the radius and thickness of the circular plate; ν is Poisson's ratio; E is Young's modulus; σ_0 is the initial in-plane stress; and p_z is the uniform transverse load.

For small deflections, the surface shape of a circular plate is given by the following equations for a simply supported boundary and a clamped boundary, respectively.

$$\text{– Simply supported boundary:} \quad w(\xi) = 3(1-\nu^2)hP \left[\frac{2(1+\nu)(I_0(k\xi) - I_0(k))}{k^3(kI_0(k) + (\nu-1)I_1(k))} + \frac{1-\xi^2}{k^2} \right] \quad (2-7)$$

$$\text{– Clamped boundary:} \quad w(\xi) = 3(1-\nu^2)hP \left[\frac{2(I_0(k\xi) - I_0(k))}{k^3 I_1(k)} + \frac{1-\xi^2}{k^2} \right] \quad (2-8)$$

where w is the vertical displacement; $\xi = r/a$ is the normalized radial distance. $I_0(k\xi)$ and $I_1(k\xi)$ are modified Bessel functions of the first kind. For both boundary conditions, the surface shape of a pure membrane ($k \rightarrow \infty$) is ideally parabolic, while the surface shape of a pure plate ($k = 0$) deviates from a parabola.

Using equations (2-7) and (2-8), the surface shapes of circular plates with different boundaries are plotted in Figure 2-13 for no initial stress ($k = 0$). A parabolic curve is also plotted for comparison. It can be seen that the simply supported plate is much closer to the parabolic curve than the clamped plate.

Effect of the initial stress can be studied by using equations (2-7) and (2-8) for different values of the stress parameter. Figure 2-14 suggests that both the simply supported plate and the clamped plate tend to the parabolic curve with increasing initial

stress. However, with the same initial stress, the simply supported plate is more parabolic than the clamped plate.

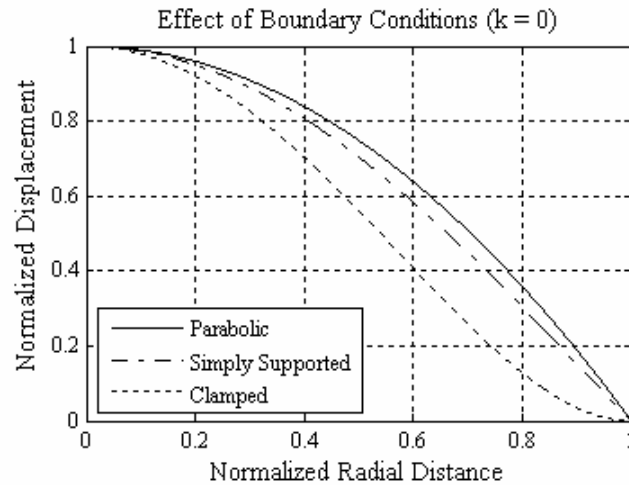


Figure 2-13. Effect of boundary condition on surface shape.

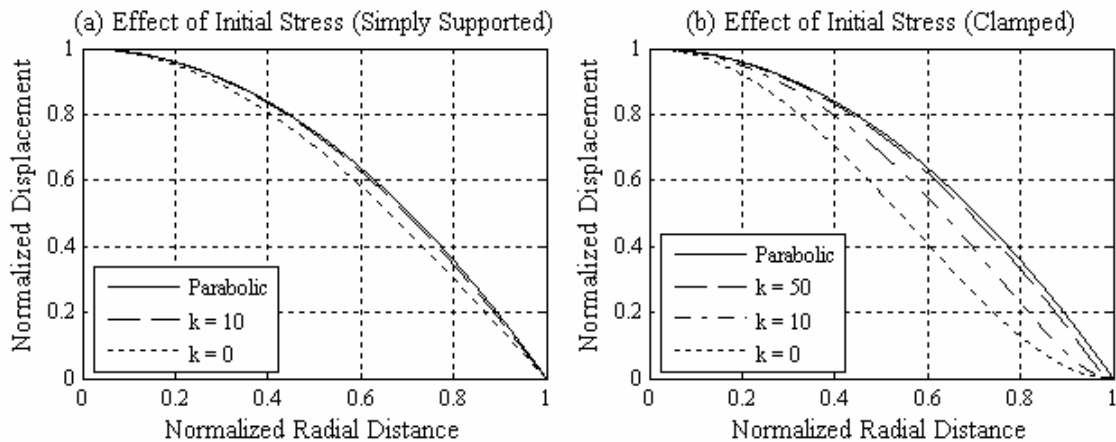


Figure 2-14. Effect of initial stress on surface shape. (a) Simply supported plate; (b) Clamped plate.

Finite Element Analysis (FEA)

The mechanical plate theory indicates that a uniformly loaded membrane with a simply supported boundary bends to surface shapes very close to a parabola. To emulate

the simply supported boundary condition, the boundary support of the deformable membrane was weakened by segmenting the perimeter. Zonal actuation with two concentric annular electrodes was incorporated as an additional design parameter to allow active control of the surface shape. The segmented perimeter and the two-zone actuation do not have analytical solutions but can be investigated with numerical methods. A finite element model of the deformable membrane was built to study and design the segmented perimeter and the two-zone concentric electrodes by Himmer [22] and Friholm [24]. This FEA model indicates that segmenting of the perimeter results in more parabolic shapes but the improvement flattens out at about 10% support. It also suggests that moving the pressure load from the inner to the outer electrode shifts the curvature from negative spherical aberration to positive aberration for approximately a 90% aperture [22]. Based on this result, the deformable membrane of the 3-D mirror employs a weakened perimeter with 10% support and a two-zone actuation to minimize and adjust the spherical aberration.

Design Parameters of the Deformable Membrane

The deformable membrane of the 3-D mirror is made of low-stress silicon nitride, which can be chosen from two deposition recipes (LSN900, LONH378) of different initial stresses (40 MPa, 150 MPa). Table 2-5 lists mechanical properties of the two silicon nitride recipes. In previous sections, material and geometrical parameters were examined theoretically for their effects on performance characteristics for the deformable membrane. These effects were also studied experimentally [22]. The optimum design

parameters given fabrication process constraints were chosen according to the theoretical and experimental studies and are listed in Table 2-6.

Table 2-5. Material properties of silicon nitride [42, 43].

Poisson's ratio	$\nu_{SiN} = 0.24$
Young's modulus	$E_{SiN} = 2.60 \times 10^{11} Pa$
Initial in-plane stress (LSN900)	$\sigma_0 = 40MPa$ (stress parameter $k = 16$)
Initial in-plane stress (LONH378)	$\sigma_0 = 150MPa$ (stress parameter $k = 30$)

Table 2-6. Design parameters of the deformable membrane.

Thickness of the SiN film	$\sim 1 \mu m$
Diameter of the inner electrode	$345 \mu m$
Inside diameter of the outer electrode	$355 \mu m$
Outside diameter of the outer electrode (Maximum usable optical aperture)	$700 \mu m$ (to meet optical design target)
Inside diameter of the segmented perimeter	$710 \mu m$
Outside diameter of the segmented perimeter	$740 \mu m$
Number of the support strips	18
Width of the support strips	2° (center arc length is $12.65 \mu m$)
Thickness of the sacrificial PSG pad	$0.2 \mu m$
Diameter of the sacrificial PSG pad (Diameter of the membrane)	$746 \mu m$
Depth of the cavity underneath the membrane	$8 \sim 12 \mu m$ (to achieve up to $4 \mu m$ center displacement)

The thickness of the silicon nitride film was chosen with consideration of both the deformable membrane and the torsional hinges; and trade-off must be made between lowering the actuation voltages and improving the device robustness. The usable optical aperture (700 μm diameter) was maximized for the overall device diameter (1500 μm). The 18 silicon nitride strips of 2° wide each on the segmented perimeter establish a 10% support on the boundary, which emulates a simply supported boundary, producing more parabolic surface shapes. The segmented perimeter has also an added advantage of reducing the actuation voltages. The two concentric annular electrodes enable actuation of the membrane with nonuniform loads, adding one more degree of freedom to control the surface shape. Finite element analysis and experiments have verified that a deformable membrane with a segmented perimeter and two-zone actuation can achieve parabolic surface shapes with the deviation less than $\lambda/20$ ($\lambda = 500 \text{ nm}$) through the full range of deflection [22]. The two-zone actuation can also be used to correct the primary spherical aberration of the optical system by adding a controlled quartic term to the surface shape. Previous experiments showed that a thicker PSG layer causes longer and steeper sidewalls on the mirror perimeter, producing larger initial curvature that is not desired. On the other hand, too thin a PSG layer can increase release etch times and then produce too much oxide layer undercut underneath the silicon nitride layer. A PSG layer thickness of 200 nm was chosen to minimize the initial curvature without significantly increasing the release times.

With the given material and geometrical parameters, influence of the stress and thickness of the silicon nitride film on the membrane deflection can be estimated by using

the mechanical plate theory. The electrostatic load is given by $p_z = \epsilon_0 V^2 / 2d^2$, where V is the actuation voltage applied to the membrane, and d is the cavity depth underneath the membrane. For a rough estimation of the deflection magnitude, the cavity depth is set to 10 μm , and the load is assumed to be uniform even when the membrane is bended. Figure 2-15 plots the center displacement of the membrane versus the actuation voltage for the two silicon nitride recipes with a film thickness of 1 μm , which suggests that the initial stress affects the membrane deflection significantly. To lower the actuation voltage, the silicon nitride recipe of 40 MPa stress was chosen. Figure 2-16 plots the center displacement versus the membrane thickness at a fixed pressure corresponding to 300 volts (30 volts/ μm). The choice of ~ 1 μm silicon nitride film thickness was made with trade-off between the deflection magnitude and the device robustness.

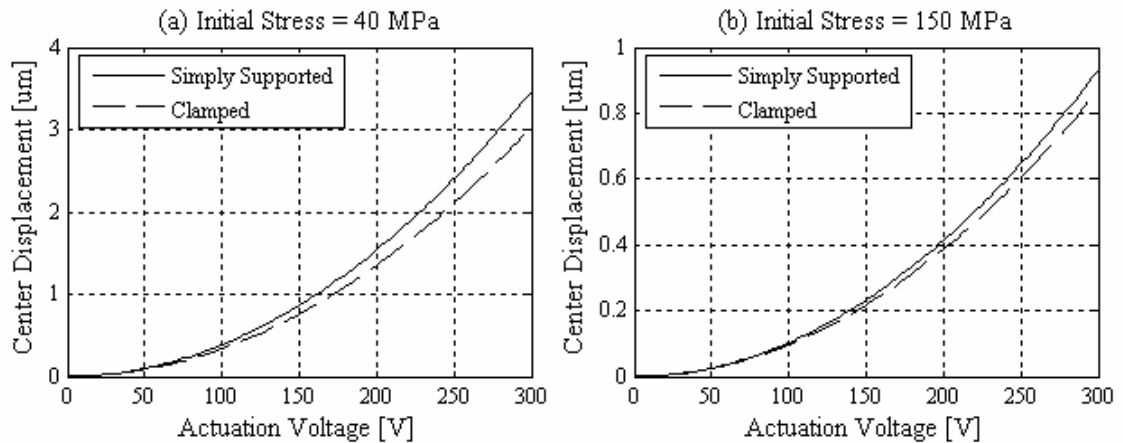


Figure 2-15. Comparison of membrane deflections of two silicon nitride recipes. Silicon nitride film thickness is set to 1 μm .

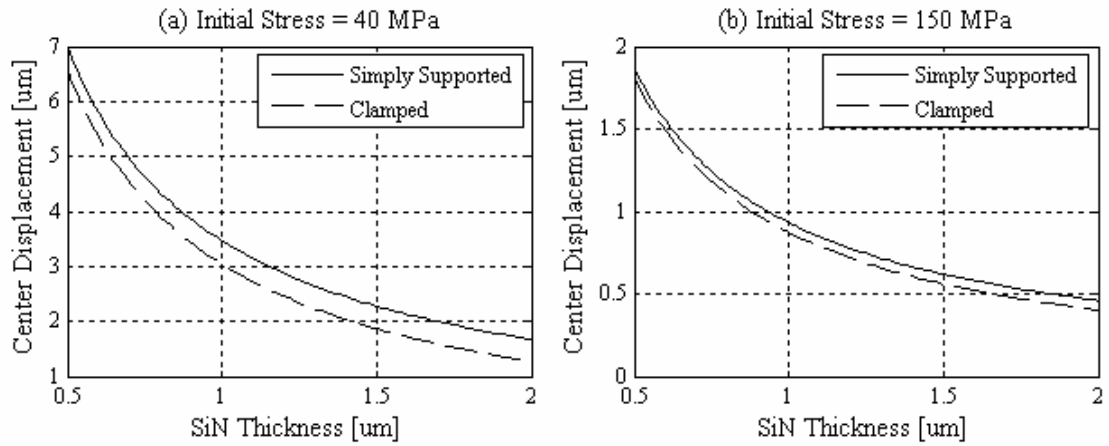


Figure 2-16. Influence of silicon nitride film thickness on membrane deflection. Actuation voltage is fixed to 300 volts.

Dynamic Distortion of the Deformable Membrane

The deformable membrane puts limitations on high speed scanning. At high scan frequencies and large scan angles the membrane may start to distort due to dynamic inertial forces, which will introduce aberrations into the optical wavefront. When the 3-D mirror is scanning uniaxially (about the inner axis), the rotation axis is stationary; and the membrane edge has a simple support. Therefore, for calculating dynamic distortion, the membrane can be modeled as a hemicircular mechanical plate with a simply supported boundary under nonuniform transverse load. For a rough estimation, the hemicircular plate is considered as a circular plate with a radius of $R/\sqrt{2}$, where R is the radius of the deformable membrane. The nonuniform load is averaged across the hemicircle to obtain an equivalent uniform load. Assuming sinusoidal angular scanning at frequency f , the load pressure raised by the inertial forces at maximum scan angle θ_{\max} is given by

$$P = \rho t x \theta_{\max} (2\pi f)^2,$$

where ρ is the density of the membrane, t is the membrane thickness, and x is the distance from the rotation axis. By averaging across the hemicircle, the equivalent uniform load is given by

$$\bar{P} = \frac{4}{3\pi} \rho t R \theta_{\max} (2\pi f)^2 .$$

Using this simplified model and equation (2-7), the dynamic distortion can be estimated. For calculation, parameters $\rho = 3.2 \text{ g/cm}^3$, $t = 1 \text{ }\mu\text{m}$, $R = 375 \text{ }\mu\text{m}$ and $\theta_{\max} = 0.087 \text{ rad (}5^\circ\text{)}$ are used. The initial in-plane stress is 40 MPa ($k = 16$). When the fast scan is running at the designed resonant frequency $f = 600 \text{ Hz}$, we calculate the average load pressure is 0.63 Pa, resulting in a negligible distortion of 0.27 nm. On the other hand, limitation on high speed scanning due to dynamic inertial forces can also be estimated using this simplified model. Assuming 500 nm illumination and a maximum acceptable membrane distortion of $\lambda/8$ ($\lambda/4$ wavefront aberration), we calculate the maximum scan frequency is about 9100 Hz.

Optical Issues of the Deformable Membrane

The deformable membrane of the 3-D mirror is axially symmetric, so its surface shape can be expanded to a Taylor series in the following form.

$$s(r) = a_0 + a_2 r^2 + a_4 r^4 + a_6 r^6 + \dots .$$

This series contains only even-order terms because of the axially symmetric nature of the surface. By neglecting the sixth- and higher-order terms, the surface shape is approximated to a fourth-degree polynomial.

$$s(r) = a_2 r^2 + a_4 r^4,$$

where the zero-order term is not included because it does not affect the surface shape.

The second-order term a_2 relates to the effective focal length according to $f = 1/4a_2$, while the fourth-order term a_4 represents the primary spherical aberration that will be introduced to the wavefront by the membrane mirror. On the other hand, a controlled fourth-order term also can be used to zero out the primary spherical aberration already existing in the system. Finite element analysis and previous experiments show that the two-zone actuation with 10% segmentation can compensate spherical aberrations up to 4 waves at 500 nm illumination [22]. The 3-D mirror is mainly designed for scanned-beam imaging systems, where spherical aberration is important since it is dependent on the depth of imaging into a different material. Therefore, it is desirable to incorporate a quartic curvature into the surface shape to correct system spherical aberration adaptively. In the following, wavefront aberration theory will be used to discuss the aberration correction capability of the membrane mirror. Limitations on use of the membrane mirror will also be discussed.

Wavefront Aberration Theory

Wavefront aberrations are defined as the deviation of the actual constant phase wavefront produced by the optical system from a perfect sphere centered on the image point. A corrective element is designed to add a variable optical path delay to the wavefront in order to just cancel the aberration and produce a wavefront that is again perfectly spherical. A reflective element with surface shape $s(x, y)$ adds a correction $w(x, y) = 2s(x, y)$.

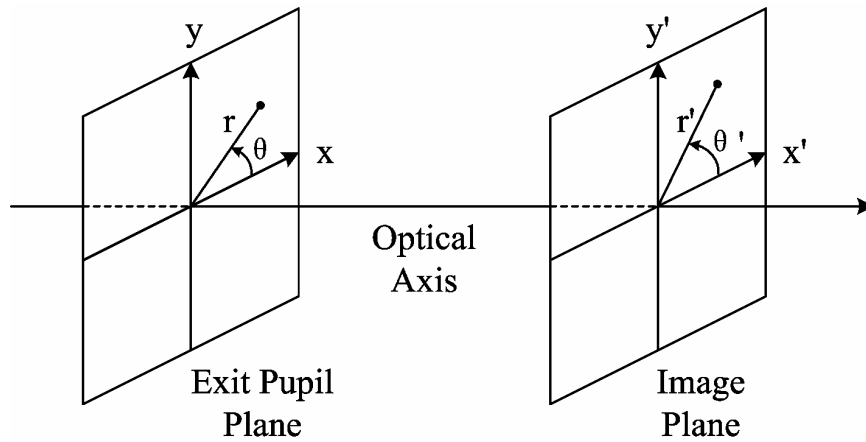


Figure 2-17. Coordinate system used to describe wavefront aberrations.

For the purpose of computation, a particular plane must be specified for observation of the wavefront; and it is typically the exit pupil plane of the optical system. Figure 2-17 illustrates the coordinate system used to describe the wavefront aberrations. The primary (Seidel) aberrations for an axially symmetric optical system can be expressed as [40]

$$w(x, y; x', y') = a_s r^4 + a_c (x'x + y'y)r^2 + a_a (x'x + y'y)^2 + a_f r'^2 r^2 + a_d r'^2 (x'x + y'y),$$

where $r^2 = x^2 + y^2$ and $r'^2 = x'^2 + y'^2$. The five terms in this expression represent spherical, coma, astigmatism, field curvature (defocus) and distortion (wavefront tilt), which are listed in Table 2-7.

Table 2-7. Primary (Seidel) aberrations.

Spherical aberration	$a_s r^4$
Coma	$a_c (x'x + y'y)r^2$

Astigmatism	$a_a(x'x + y'y)^2$
Field curvature (defocus)	$a_f r'^2 r^2$
Distortion (wavefront tilt)	$a_d r'^2 (x'x + y'y)$

In the expression of wavefront aberration, spherical aberration and field curvature (defocus) are axially symmetric in the exit pupil plane coordinates. Therefore it is possible to correct these two aberrations by deforming the membrane mirror accordingly. In addition, spherical aberration is independent of the image point location, so it can be corrected by introducing a static fourth-order term into the surface shape. Similarly, field curvature can be compensated with a second-order term. However, field curvature is dependent on the image point location, so the membrane mirror has to be adjusted pixel-by-pixel in real-time for a scanned-beam imaging system to correct the field curvature. Distortion is correctable with the scanning mechanism. Coma and astigmatism, on the other hand, are not axially symmetric in the exit pupil plane coordinates, thus must be corrected by other means. In conventional microscopy that has small field angles, coma dominates over astigmatism and is usually corrected by the objective lens.

On-axis Imaging

A parabolic mirror behaves as an infinite conjugate optical element. That is, a plane wave parallel to the optical axis is focused to an on-axis point, which is defined as the focal point of the parabolic mirror. An on-axis infinite object is imaged without aberration by a parabolic mirror. However, an off-axis infinite object suffers from coma and astigmatism. Assume a plane wave makes an angle φ with the optical axis and is

incident on the parabolic mirror. The wavefront aberration of the reflected beam at the mirror plane can be expressed as [25]

$$w(\varphi, r, \theta) = \frac{1}{4f^2} \varphi r^3 \cos(\theta) - \frac{1}{2f} \varphi^2 r^2 \cos^2(\theta),$$

where the first term represents coma and the second term is astigmatism. In this equation, polar coordinate (r, θ) is used on the exit pupil where the aberration is calculated. f is the focal length of the mirror. For non-infinite objects, parabolic mirrors can suffer from all types of aberrations. Coma and astigmatism introduced by the 3-D mirror when it is rotated about the axis can be calculated using the equation above. Given the optical aperture of 700 μm , the minimum focal length of 10 mm and the maximum mechanical tilt angle of 5° , we obtain coma 0.02 waves and astigmatism 0.09 waves for 500 nm illumination. Such amount of aberrations is insignificant for microscopy, indicating that $\pm 5^\circ$ scan angles will not degrade imaging quality.

Based on the discussion above, we conclude that the 3-D mirror must be used in an on-axis arrangement with moderate scan angles to prevent degradation of imaging quality. For applications where the 3-D mirror is used for focus control with a variable parabolic shape, the optical system must also have an infinite conjugate ratio to avoid aberrations. However, non-parabolic shape can compensate for non-infinite conjugate operation.

CHAPTER 3

FABRICATION OF THE MEMS 3-D MIRROR

Starting with an introduction to the silicon micromachining technology, this chapter presents the process steps used to fabricate the 3-D MEMS scan mirrors. The design of the fabrication process flow must consider a number of factors including target device performance, fabrication process limitations, material properties, material compatibilities and some practical concerns. The 3-D mirrors were fabricated at the Stanford Nanofabrication Facility (SNF) and Washington Technology Center (WTC) with nine photo masks. The fabrication process involved surface micromachining, bulk micromachining, wet chemical etch, reactive ion etch (RIE, also known as plasma etch) and deep reactive ion etch (DRIE).

Introduction to Silicon Micromachining Technology

Micromachining refers to the technologies of making mechanical structures and devices at the scale of microns. Micromachining uses the same suite of materials and techniques as microelectronics, which is a very well developed technology of producing electronic circuitry on silicon chips. Photolithography is the primary technique used to define the shape of micromachined structures in three steps – deposition, lithography and etching. The three sequential steps constitute a process cycle, each cycle forming a structural layer. Figure 3-1 shows the process cycle for producing one structural layer.

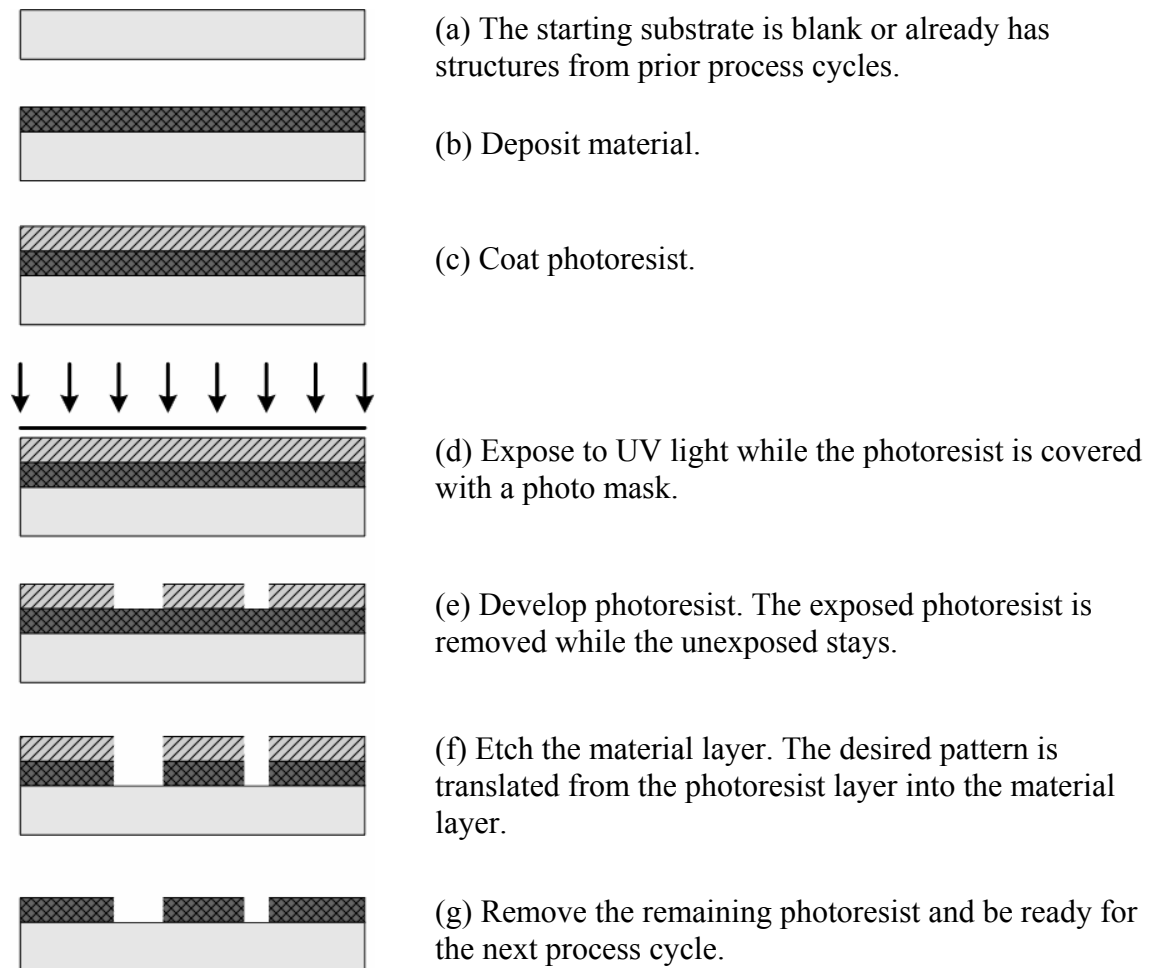


Figure 3-1. Process steps to create a structural layer.

The process cycle starts with a blank substrate (or a substrate with structures established in prior cycles). The first step is material deposition. Available materials include polysilicon, silicon oxide, silicon nitride, metals, etc. Deposition techniques include thermal oxidation, low pressure chemical vapor deposition (LPCVD), plasma enhanced chemical vapor deposition (PECVD), evaporation, sputtering, etc.

To pattern the deposited material layer, a mask layer with the desired pattern must be first overlaid on the material layer. This procedure is known as “pattern transfer”

meaning transferring the pattern in the mask layer to the material layer. Typically, the mask layer is made of photoresist, which is a photo-sensitive polymer. Photoresist is usually applied by spinning a liquid solution onto the substrate, and is then hardened by baking. After coated with photoresist, the substrate is covered with a photo mask and exposed to UV light. During development, exposed regions of the (positive) photoresist are removed by the developer, thus the corresponding regions of the underlying material layer are open. The thickness of the photoresist coated is determined by the subsequent etch step, which etches the material layer and also the photoresist though usually at a much slower rate. Once the thickness requirement is satisfied, a thinner photoresist is desired because it yields better pattern resolution.

The last step is to create the pattern into the material layer by etching. There are two etch techniques commonly used in micromachining – chemical wet etch and plasma dry etch. Most chemical solutions etch materials isotropically, while plasma etch can be anisotropic or isotropic depending on the recipe. Because the etchant etches the material as well as the photoresist, the etch rate ratio between the etched material and the photoresist must be large enough so that the photoresist is not completely etched away.

After the etching is complete, the photoresist can be washed away by photoresist stripper. Commonly used strippers include mixture of sulfuric acid and hydrogen peroxide ($\text{H}_2\text{SO}_4:\text{H}_2\text{O}_2$), oxygen plasma and some ready-for-use chemical solutions such as PRX-127 and SVC-175 (manufactured by Rohm and Haas Electronic Materials Company). The choice of stripper is determined by the materials on the substrate and the photoresist used. The basic principle is that the photoresist must be cleaned completely while the material cannot be damaged.

Modified Surface Micromachining

As described in the deformable membrane design section, a cavity must be created between the membrane and the silicon substrate to allow movement of the membrane. Surface micromachining is a commonly used technique to build this structure where a sacrificial layer is deposited beneath the membrane layer and is later removed leaving the membrane free to move. To etch the sacrificial material, small holes through the membrane must be created. One disadvantage associated with the surface micromachining technique is that the cavity depth is limited by the thickness of the sacrificial layer. In addition, too thick sacrificial layer can cause step-up problem at the boundary, which can cause initial curvature of the deformable membrane and can lead to failure of the membrane around the perimeter. Realized membrane deflection was limited to approximately 1 μm with a sacrificial layer thickness of a few microns using the surface micromachining technique.

The modified micromachining process incorporates a bulk silicon etch after the sacrificial layer etch. This technique uses a sacrificial layer of phosphosilicate glass (PSG) under the free-standing membrane for rapid lateral etch, then the post-release silicon etch step is performed to achieve the desired cavity depth. The two step release process for creating a cavity is illustrated in Figure 3-2. By using this technique, the depth of the cavity can be tailored to specific requirements while the sacrificial layer thickness can be minimized to avoid the step-up problem. As little as 100 nm PSG has proven effective for rapid lateral etch between etch holes on a 30 μm grid spacing [22].

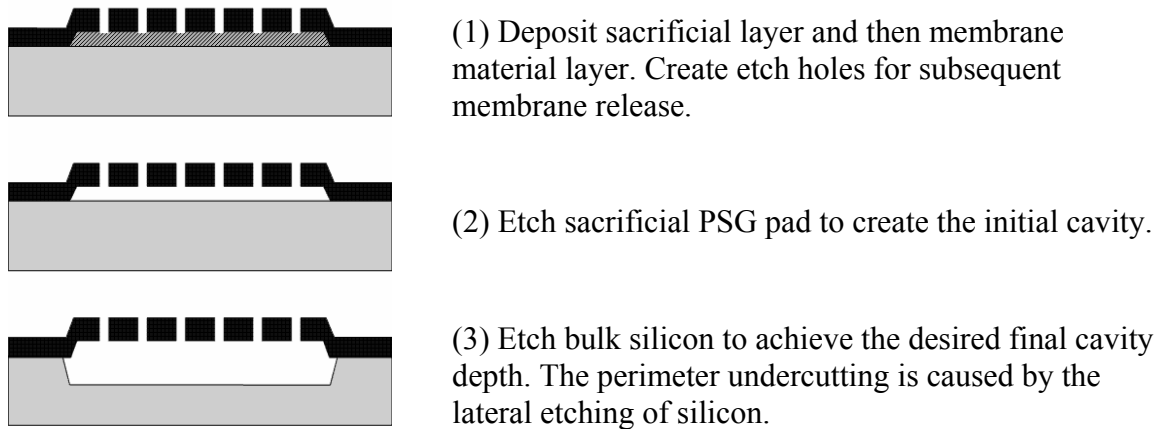


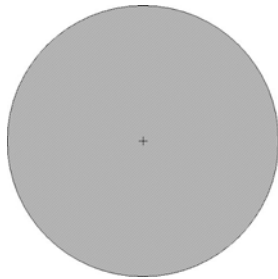
Figure 3-2. Modified surface micromachining process for creating a cavity of variable depth.

Design of Photo Masks

The patterns are originally designed in the photo mask layout stage. Layout software such as Tanner Tools L-Edit or Auto CAD can be used to design the masks. The physical mask is made of a quartz plate with chrome coating while openings in the chrome are transparent to UV light. A mask writer is used to write a mask layout data file into the chrome-coated quartz plate. In the fabrication stage, the patterns are first transferred from the photo mask into the photoresist and then into the structural material layer.

Masks for a Single Mirror

Nine photo masks were made to fabricate the 3-D mirrors and are shown in Figure 3-3; each of them corresponds to one of the structural layers. The numbering of the masks is in the order of the sequence of the fabrication steps. The process using these masks is described in section 3.4.



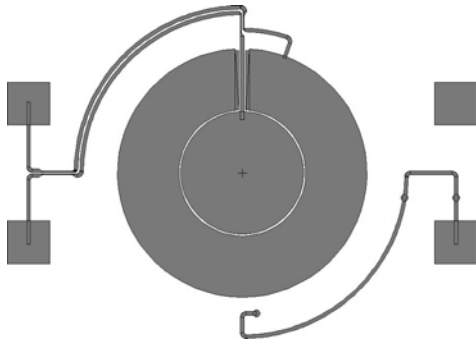
Mask 1. Sacrificial PSG pad.

[Features are too small to show]

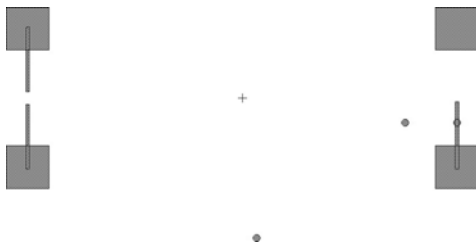
Mask 2. Implantation windows through the silicon nitride layer.

[Features are too small to show]

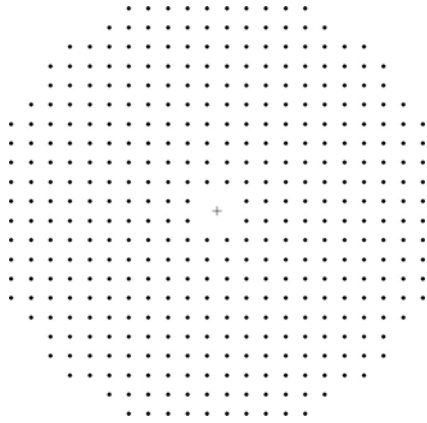
Mask 3. Implantation windows through the silicon thermal oxide layer.



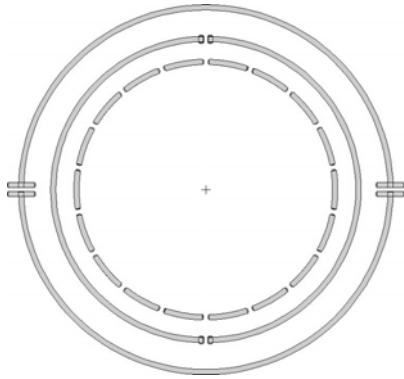
Mask 4. Metal electrodes.



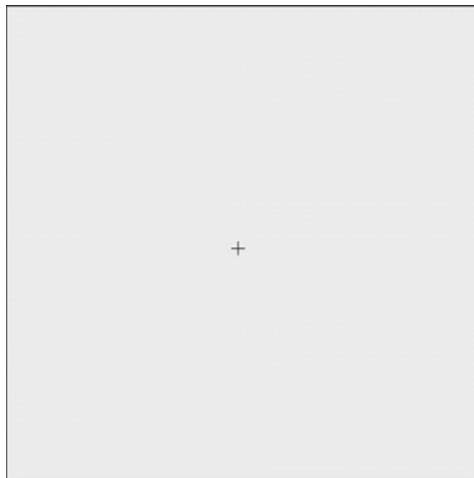
Mask 5. Metal liftoff (thick metal).



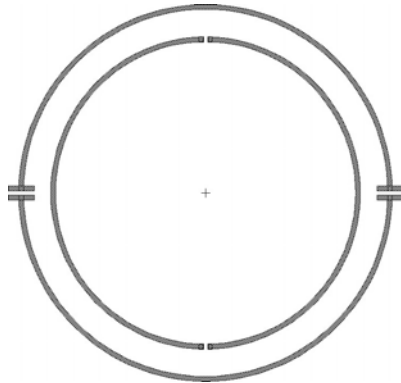
Mask 6. Etch holes through the metal and silicon nitride layers.



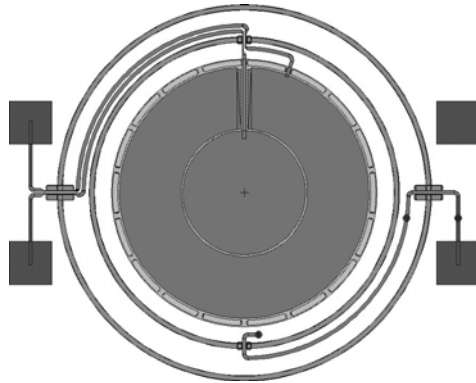
Mask 7. Silicon nitride mechanical layer outline.



Mask 8. KOH etch window on the backside (this figure scales 1/2 compared to other masks).



Mask 9. DRIE trenches.



Composite of masks (excluding mask 8 of backside KOH etch window).

Figure 3-3. Photo masks of the 3-D mirror. The numbering of the masks is in the order of the sequence of the fabrication steps.

Masks for Batch Fabrication of Mirrors on 4-inch Wafers

To carry out batch fabrication of the 3-D mirrors on 4-inch wafers, the single-mirror masks were repeated to create a standard 4-inch mask. First, nine identical mirrors were grouped into one die, as illustrated in Figure 3-4 (a), where the top and left lines were designed for dicing the wafer into smaller dies before the post-fabrication release etches. Thirty-two dies with variant designs were then arranged on a 4-inch quartz/chrome photo mask. Composite of the batch fabrication masks is shown in Figure

3-4 (b). Alignment marks were also designed into the masks to align each layer to the previous layers.

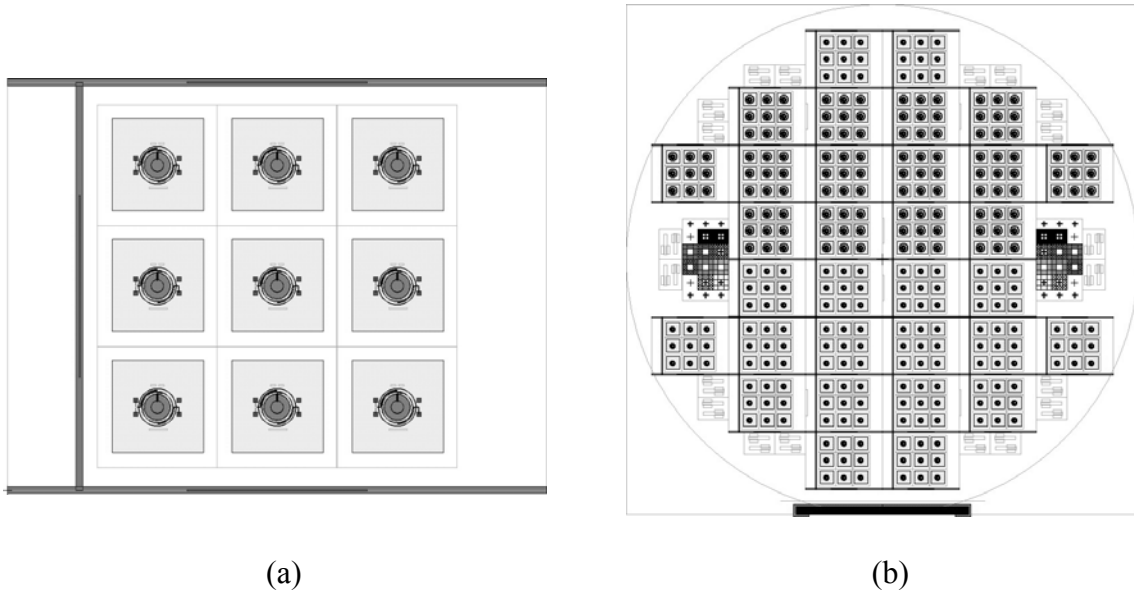


Figure 3-4. Standard 4-inch photo mask layout. (a) A single die on the 4-inch mask; (b) Standard 4-inch photo mask.

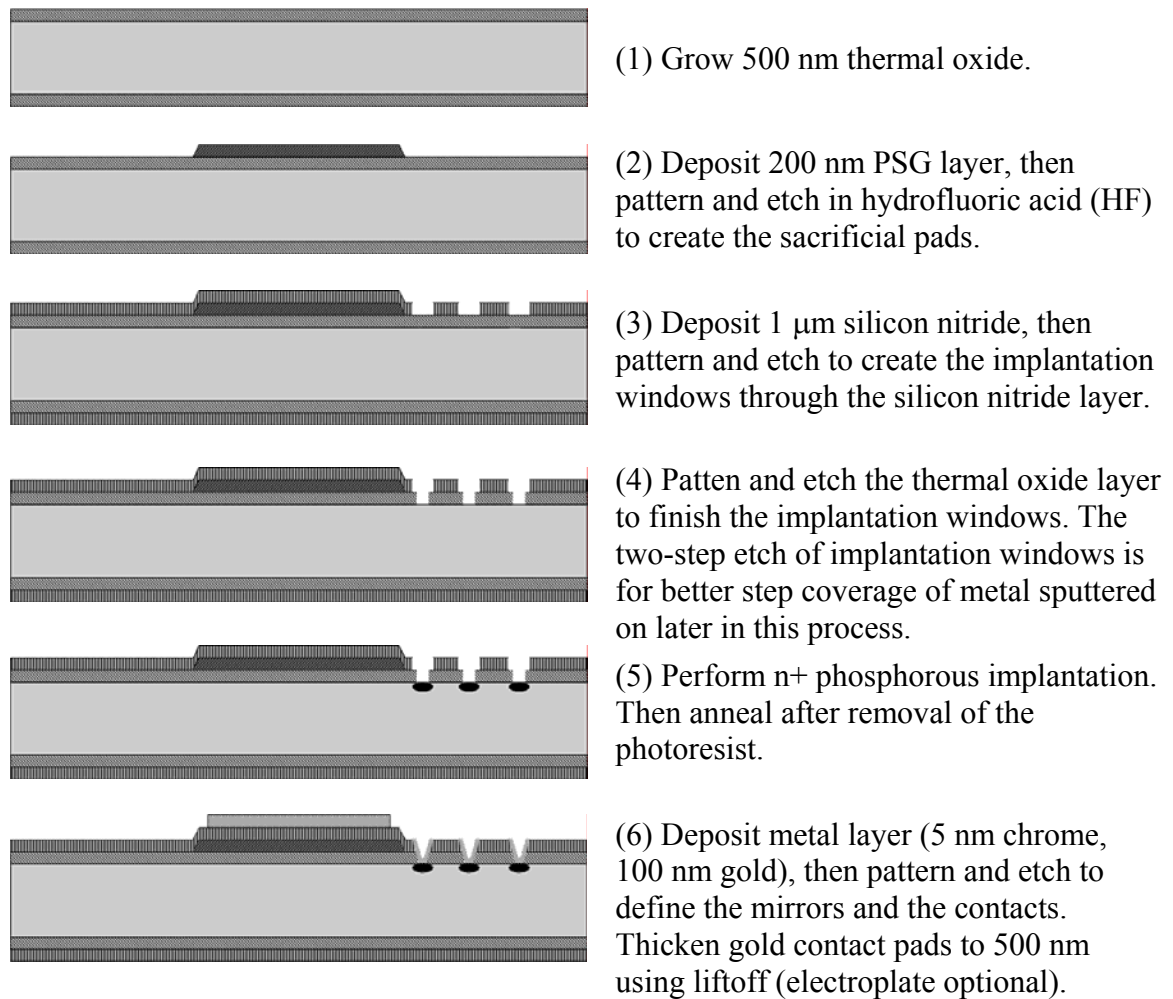
Batch Fabrication Process

The fabrication process of the 3-D mirrors can be roughly broken into two stages – batch fabrication and post-fabrication device release. The batch fabrication process was carried out at the Stanford Nanofabrication Facility (Stanford, CA). In this stage, the fabrication was done in a batch mode, that is, all the mirrors on one wafer experienced exactly the same process. On the other hand, the post-fabrication release process can be different for each mirror, thus providing a freedom to tailor the mirror characteristics for different requirements. The device release was carried out in the Micro Optics and Imaging Lab of the Montana State University after the wafer was diced into smaller dies,

each of which has nine identical mirrors on it. The two stages of the fabrication process are described in this section and the next section, respectively. Figure 3-5 illustrates the entire process flow.



– Batch fabrication process



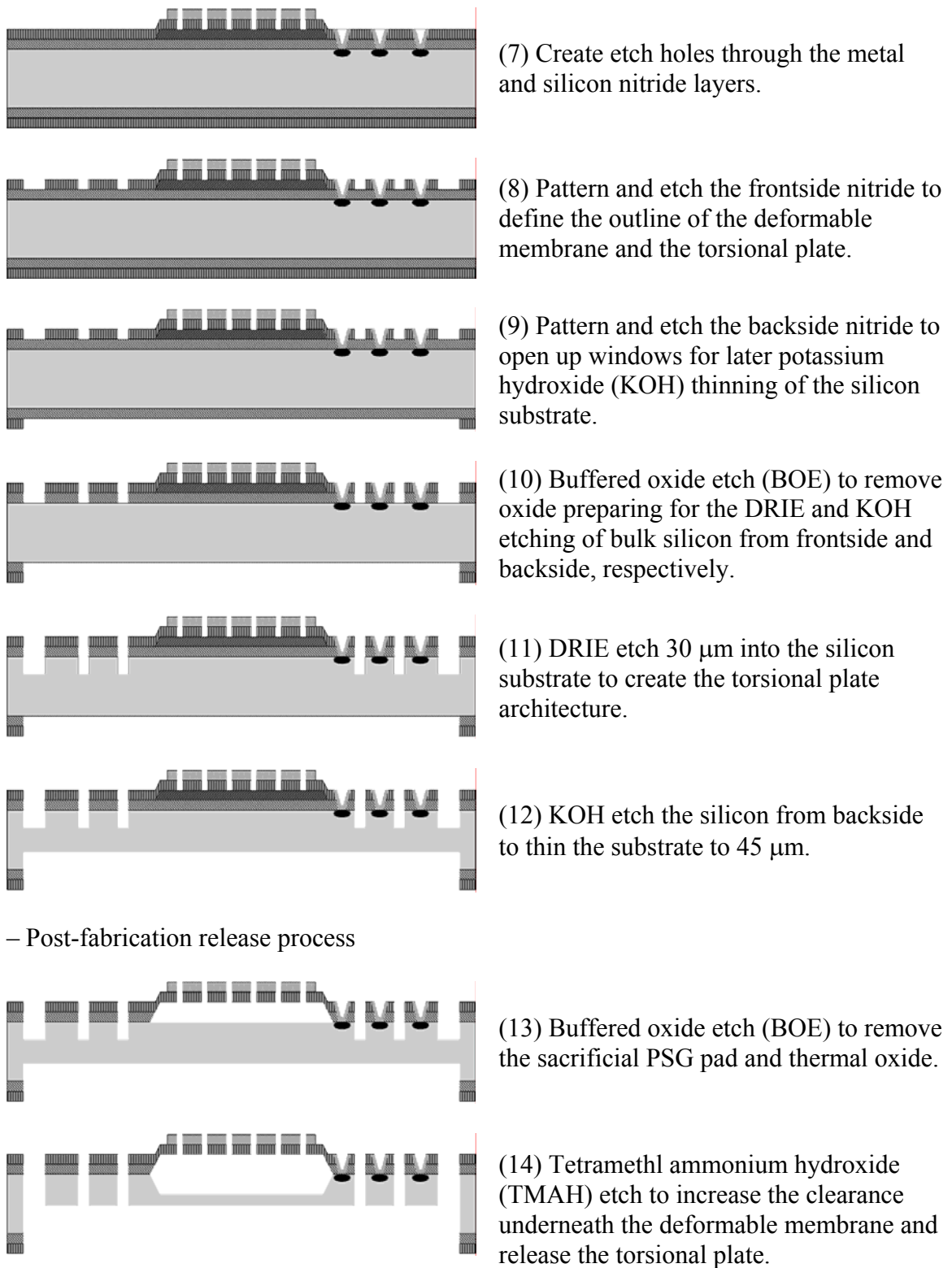


Figure 3-5. Fabrication process flow of the 3-D mirror.

The starting wafers were <100> n-type double-side polished with a thickness of 460 μm and a diameter of 100 mm. In the potassium hydroxide (KOH) thinning step the silicon substrate was etched from the backside while most other steps were performed on the frontside therefore both sides of the wafers need to be polished. In addition, the substrate thickness was expected to be uniform across the whole wafer after the KOH etching thus the total thickness variation (TTV) of the starting wafers was chosen to be less than 3 μm .

The first step in the fabrication process was to grow a 500 nm thermal oxide layer on the silicon substrate using a wet process at 1000 $^{\circ}\text{C}$, which provides electrical isolation between the silicon and the metal layers. Before growing the thermal oxide, a pre-diffusion clean process was performed to clean the wafers completely, which included a sulfuric peroxide ($\text{H}_2\text{SO}_4:\text{H}_2\text{O}_2$) clean, a hydrofluoric acid (HF) dip, and a $\text{H}_2\text{O}:\text{HCl}:\text{H}_2\text{O}_2$ clean. The sulfuric peroxide solution removed the organic contaminants from the wafers. The HF dip removed the chemical oxide put on during the sulfuric peroxide step. The $\text{H}_2\text{O}:\text{HCl}:\text{H}_2\text{O}_2$ removed any metal contaminants that might be on the wafers (it is most effective if done after stripping off the chemical oxide). The pre-diffusion clean was performed prior to deposition of any material on the wafers and will not be repeated in the following description of the process.

Upon the thermal oxide layer, the sacrificial layer of 200 nm phosphosilicate glass (PSG) with 8% phosphorus was deposited at 400 $^{\circ}\text{C}$. Then the PSG layer was patterned and etched with HF to form round sacrificial pads. The size of the PSG pad represents the actual size of the deformable membrane. HF etches PSG much faster than thermal oxide thus it was chosen to establish the sacrificial layer. The sacrificial pad was used to

provide a space to etch the underlying bulk silicon effectively in the post-fabrication release step. The silicon nitride layer establishing the deformable membrane overlies on the PSG layer therefore the deformable membrane will have a step-up sidewall around the perimeter of the PSG pads. The sidewall can cause initial curvature of the membrane and device failure on the perimeter thus thinner PSG pas is desired. On the other hand, too thin PSG layer can increase release etch times and produce more thermal oxide undercut beneath the silicon nitride layer. The PSG layer thickness of 200 nm was chosen depending on previous experiments, which minimizes the initial curvature and does not significantly increase the release times.

The structural layer of the 3-D mirrors was made of low-stress LPCVD silicon nitride. Mechanical behavior of the deformable membrane and torsional hinges is determined by material properties and thickness of the silicon nitride layer. Silicon nitride is a non-stoichiometric, silica rich ratio of silicon to nitrogen. It is designed to have a minimum residual stress. The silicon nitride deposition recipe LSN900 was used for building the 3-D mirrors. LSN900 ran at 900 °C, 269.6 mTorr, with dichlorosilane (DCS) flow at 148 sccm, ammonia (NH₃) flow at 41 sccm. Deposition rate was about 10.4 nm per minute. Residual stress of roughly 40 MPa was determined from wafer bow measurements. According to analytical and numerical simulations, a 1 μm thick silicon nitride layer was deposited to achieve the target device specifications. After deposition of silicon nitride, contact holes were etched through the silicon nitride and thermal oxide layers, followed by an n+ phosphorous implantation into the silicon substrate through the contact holes. The n+ implantation was to ensure good electrical contact between the silicon substrate and the grounding metal regions deposited and patterned later in this

process. Isotropic reactive ion etch (RIE) of silicon nitride was used to form sloping sidewalls so that metal deposition would have a good step coverage over the contact holes. This nitride-etch recipe used 100 sccm SF₆ gas, with the pressure at 300 mTorr and the RF power at 500 watts, providing an etch rate of approximately 50 nm per minute. Thermal oxide was then etched by 6:1 buffed oxide etch (BOE). The implantation can damage the crystal cells of the silicon substrate thus an anneal at 900 °C was performed to restore the crystal structure after removal of the photoresist.

The metal layer was made of 5 nm chrome and 100 nm gold, which was sputtered upon the silicon nitride layer. The metal layer serves as both the actuation electrodes for deflecting the membrane mirror and the optical reflecting surface. Choice of metal was mainly determined by two factors – reflectance and compatibility with the subsequent process. Aluminum has the highest reflectance in the visible and near infrared spectrum but cannot be used since it is attacked by the silicon etchant. Gold was chosen because it is resistant to the device release process in addition to a relatively high reflectance in the spectrum of interest. Chrome was used as an adhesion material and compatible with the release process as well. Chrome has a very high tensile stress that can cause initial curvature of the membrane thus its thickness must be minimized. The metal layer was patterned with wet etching of gold and chrome to form the actuation electrodes and the electrical traces and pads.

The electrical contact pads on the device frame were used to reach outside electrical connections. The connections are finished by gold wire bonding. To successfully perform wire bonding, the contact pads were thickened to 500 nm by using lift-off technique. The extra metal layer was also added to the regions of ion implants to

insure step coverage. Etch holes through the metal and silicon nitride layers were created by wet etching of gold and chrome and reactive ion etch (RIE) of silicon nitride.

After creating the electrodes and the etch holes, the frontside nitride layer was patterned to define the outline of the deformable membrane and the torsional hinges using RIE, which is also referred as plasma dry etch. RIE etch is usually anisotropic meaning that it etches much faster in the vertical direction than in the lateral direction, thus does not raise undercutting problems. This is one advantage of RIE etch compared to chemical wet etch, which is isotropic thus producing more undercutting. One disadvantage of RIE etch is that the etching rate across the wafer is not as uniform as wet etch. One can rotate the wafer while etching to improve the etching uniformity. In addition, when an etching need to be all the way through a material layer, an over-etch may be necessary to account for variations in etch rate and film thickness. In fabrication of the 3-D mirrors, all etches through the silicon nitride layer or the oxide layer were given a 10% over-etch.

Following the frontside silicon nitride patterning, silicon nitride on the backside of the mirrors was patterned with square windows. This etch was performed to prepare for backside KOH etching of bulk silicon. BOE etch was then performed to remove oxide in silicon nitride openings and expose silicon for DRIE and KOH etch.

To create the torsional hinge structure, trenches were etched into the silicon substrate from the frontside using DRIE, which is able to create very deep trenches with an aspect ratio up to 30. The structural trenches of the 3-D mirrors were about 15 μm wide and 30 μm deep.

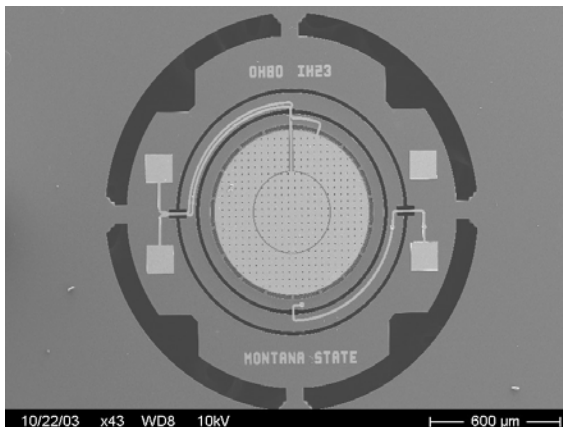
On the backside, KOH etch was performed to thin the silicon substrate to 45 μm . During KOH etching, the frontside of the wafer was protected from KOH solution. After this etch, the bottom of the structural trenches was only 15 μm away from the backside, and the remaining silicon would be completely removed in the subsequent TMAH bulk silicon etch to release the mirrors.

Post-fabrication Release Process

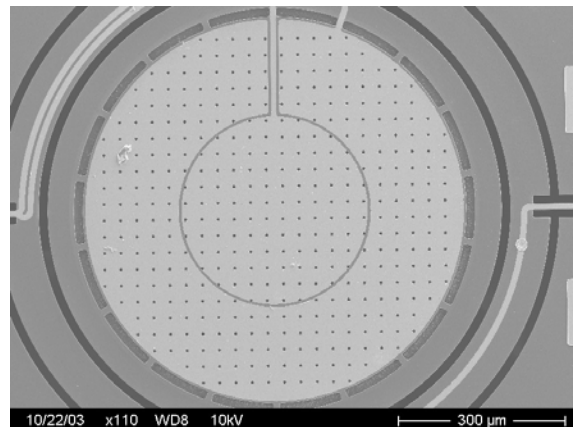
The post-fabrication release process consists of two steps: sacrificial PSG pad and thermal oxide layer etch and bulk silicon etch. PSG and thermal oxide were etched using 6:1 BOE. The mirror has an array of circular holes of 3- μm diameter, spaced at 30 μm , through the metal electrodes and the deformable membrane to allow the BOE solution to penetrate and etch. Because the PSG etching was very fast, the thermal oxide layer etched mainly from the top rather than laterally. The etch rate of the 8% PSG is about 600 nm/minute for 6:1 BOE for open surfaces [26]. The PSG etch rate for the mirror cavity was slower due to geometrical constraints that reduced the diffusion rate of the etchant and the etched products [27]. It took about 70 minutes to completely remove the PSG pad and thermal oxide underneath the membrane.

Bulk silicon was etched using tetramethyl ammonium hydroxide (TMAH) to release the torsional plates from the frame and achieve a desired depth of the cavity beneath the deformable membrane. TMAH is an anisotropic etchant of silicon. Its etch rate ratio (1 0 0)/(1 1 1) ranges from 10 to 50 depending on the concentration and temperature. The anisotropic etch can produce a rugged perimeter around the circular cavity causing nonuniform perimeter support to the deformable membrane. Another

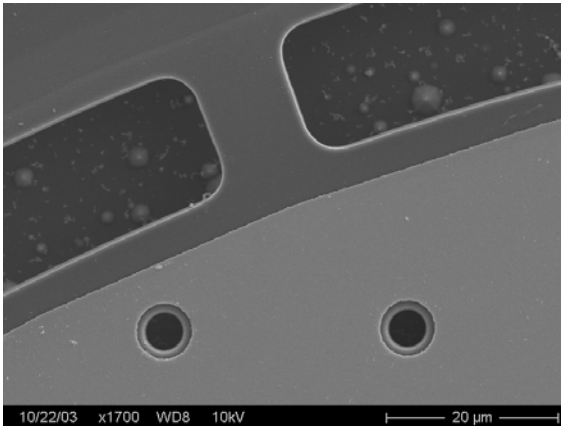
problem associated with TMAH etching is that the hydrogen gas produced by the reaction can accumulate to form large gas bubbles and rupture the overlying membrane [24]. Accumulation of hydrogen gas on the underside membrane surface was prevented by adding surfactant NCW-601A (manufactured by Wako Pure Chemical Industries, Ltd., Japan) into TMAH solution [24]. Adding surfactant also reduced the etch rate and produced a more isotropic silicon etch thus improved the membrane perimeter uniformity. The mirrors were successfully released with 12 w.t.% TMAH and 0.5% NCW-601A at 70 °C. The etch rate at this condition was about 3 $\mu\text{m}/\text{hour}$. The depth of the cavity was targeted at 8 ~ 12 μm for a maximum deflection of 4 μm at the membrane center. Insofar, the mirror has been successfully fabricated and released. Figure 3-6 shows scanning electron micrographs (SEM) of a released 3-D mirror.



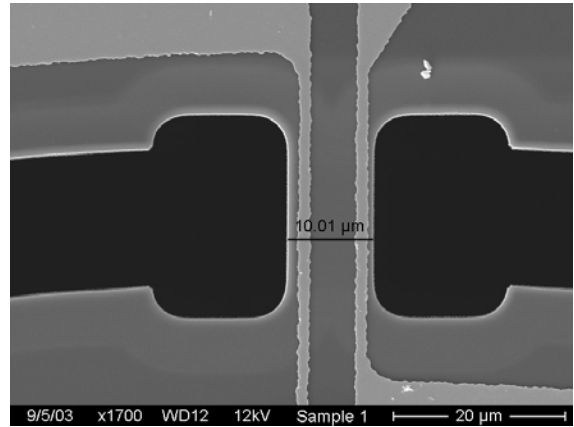
(a) A released 3-D mirror.



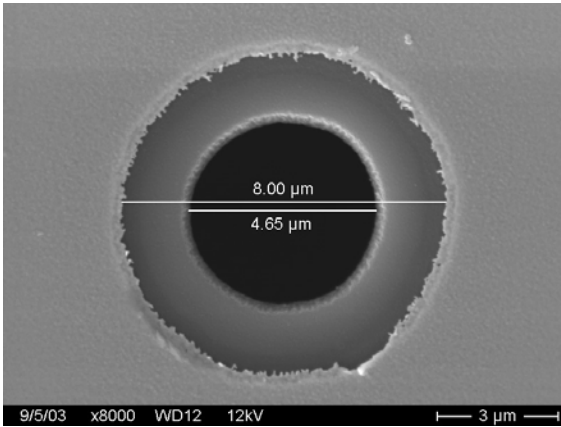
(b) The central mirror plate.



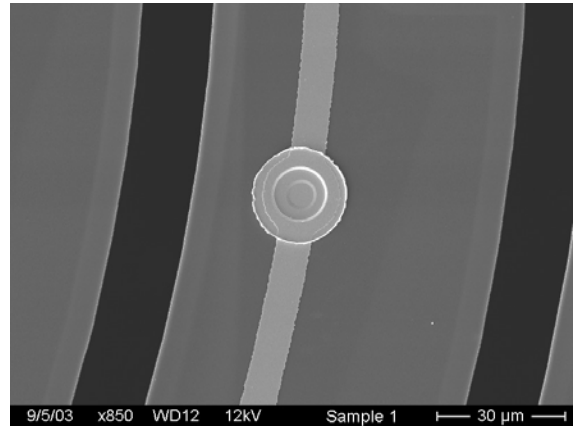
(c) The segmented perimeter.



(d) The inner torsional hinge.



(e) An etch hole through the membrane.



(f) An n+ implantation area covered by metal.

Figure 3-6. Scanning electron micrographs of a released 3-D mirror.

CHAPTER 4

CHARACTERIZATION OF THE MEMS 3-D MIRROR

This chapter describes experimental characterization of the torsional plate and the deformable membrane of the 3-D mirror. For the torsional plate, static and resonant operations were characterized for both uniaxial and biaxial scanning. For the deformable membrane, the maximum deflection and the surface shape were measured. The measured performance characteristics were then used to derive imaging capability such as lateral and depth resolutions. Biaxial scanning and focus control was operated simultaneously to demonstrate the capability of the mirror to move the focus of a laser beam throughout a three dimensional space. Lissajous scan patterns were obtained for this demonstration.

Characterization of the Torsional Plate

The torsional plate of the 3-D mirror is capable of biaxial scanning about two orthogonal axes. Characterization of static and dynamic torsion behavior of the torsional plate is covered in this section. The torsion behavior is dependant on mechanical properties of the structural materials as well as the geometrical architecture and dimensions. These parameters are discussed in Chapter 2 and listed in Table 2-2 and Table 2-3. The same mirror was used for all the experiments described in this section. Its inner hinges were 10 μm wide by 23 μm long, and outer hinges were 10 μm by 80 μm .

Drive Electrodes

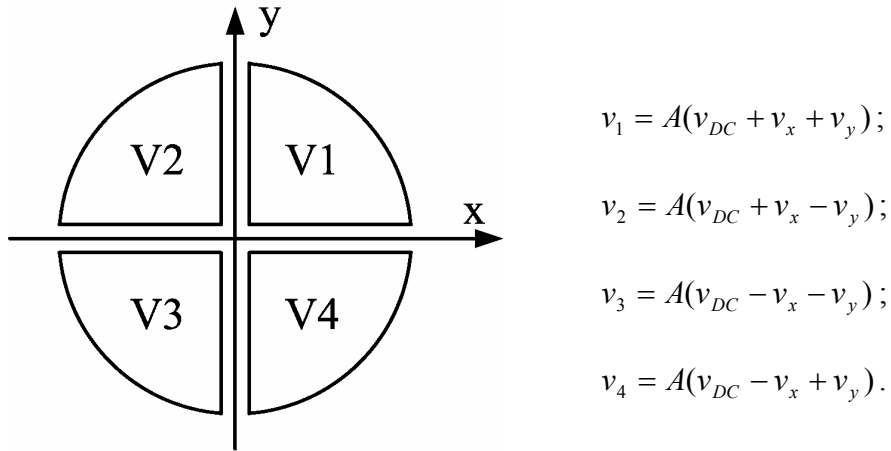


Figure 4-1. Four-quadrant drive electrodes for biaxial scanning.

The drive electrodes for biaxial scanning are on the chip carrier beneath the 3-D mirror, with the gap distance between the mirror and the electrodes being approximately 150 μm . The electrodes consist of four quadrants v_1 , v_2 , v_3 and v_4 , as illustrated in Figure 4-1. The four drive voltages v_1 , v_2 , v_3 and v_4 are generated by a four-channel signal mixer/amplifier, which mixes a DC bias v_{DC} with two differential voltages v_x and v_y according to the expressions above, where A is the gain of the signal mixer. The differential voltages v_x and v_y are for driving the 3-D mirror to rotate about the x- and y-axes, respectively. In dynamic or quasi-static operation, v_x and v_y are usually sinusoidal. Because the electrostatic attractive force is proportional to the square of the drive voltage, the DC bias v_{DC} is used to keep all the drive voltages unipolar so that the mirror response is at the same frequency as the differential voltage rather than twice of that frequency. In

the following discussion, $A = 1$ is assumed; therefore v_{DC} , v_x and v_y represent the voltages directly applied on the mirror rather than those inputting to the signal mixer. If only one axis is driven at a time, the drive voltages will be $v_1 = v_2 = v_{DC} + v_x$ and $v_3 = v_4 = v_{DC} - v_x$ for scanning only about the x-axis (inner axis); or $v_4 = v_1 = v_{DC} + v_y$ and $v_2 = v_3 = v_{DC} - v_y$ for the y-axis (outer axis).

Method for Measuring Angular Displacement

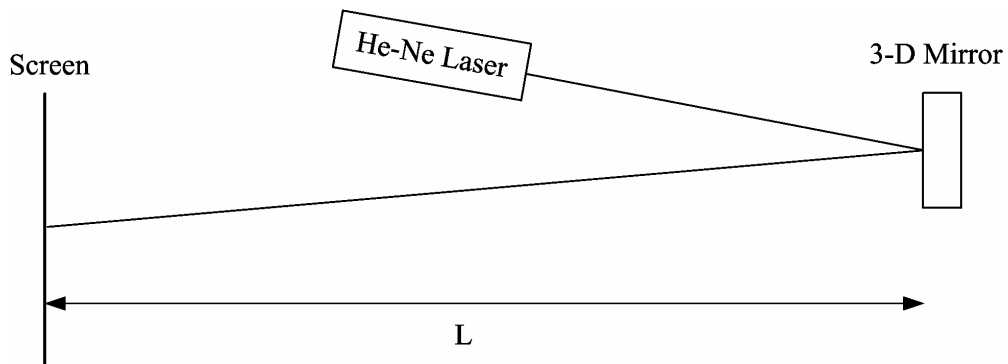


Figure 4-2. Setup for measuring angular displacements.

In characterization of the torsion behavior of the 3-D mirror, a simple optical setup illustrated in Figure 4-2 is used to measure the angular displacement. A laser beam is pointed to the 3-D mirror and then reflected by the mirror onto the screen, so the angular displacement of the 3-D mirror can be derived from the lateral displacement of the light spot on the screen and the distance between the mirror and the screen according to (small angle approximation)

$$\theta = \frac{D}{2L} \frac{180^\circ}{\pi},$$

where θ is the mechanical angular displacement of the 3-D mirror, D is the displacement of the light spot on the screen and L is the distance between the mirror and the screen. The factor 2 in the denominator accounts for the optical angular displacement of the light beam being twice of the mechanical angular displacement of the mirror.

Dependence of Resonant Frequency on DC Bias

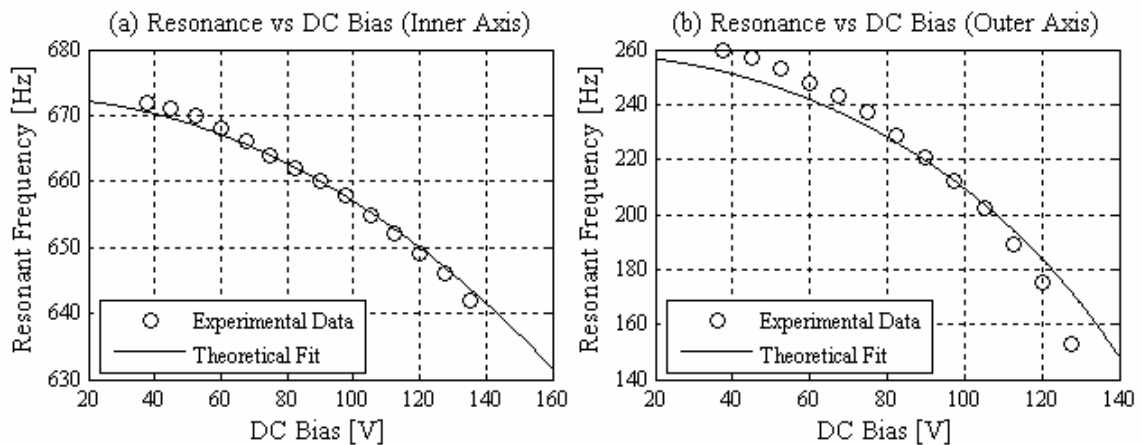


Figure 4-3. Dependence of resonant frequency on DC bias. The circles are experimental data, and the solid lines are theoretical fittings. (a) Inner axis, $A_x = 2$ V; (b) Outer axis, $A_y = 2$ V.

The resonant frequencies of the inner and outer scanning axes of the 3-D mirror are important characteristics and must meet the target specifications. The inner axis resonance was designed to be more than 600 Hz to achieve the required imaging resolution of 300x300 pixels/frame at a refresh rate of 2 frames/second; while the outer axis resonance was chosen to be near 200 Hz to lower the drive voltage and improve the shock and vibration immunity. They are governed by the following equations (refer to Chapter 2).

$$f_i = \frac{1}{2\pi\sqrt{I_i}} \sqrt{2K_i - \frac{\pi\epsilon_0 R_{ip}^4}{4D_0^3} v_{DC}^2} ;$$

$$f_o = \frac{1}{2\pi\sqrt{I_o}} \sqrt{2K_o - \frac{\pi\epsilon_0 (R_{opo}^4 - R_{opi}^4 + R_{ip}^4)}{4D_0^3} v_{DC}^2} .$$

Refer to Table 2-3 and Figure 2-5 for definitions of the parameters used in the above equations. As the equations suggest, the resonant frequencies decrease with the DC bias (v_{DC}), following an elliptic curve. This dependence provides a freedom to adjust the resonant frequencies after the mirror has been mounted.

In experimental measurement of this relationship, the DC bias was scanned with a set of consecutive values and the differential voltage (v_x or v_y) was a small sinusoidal voltage with a fixed amplitude. The drive voltages had a form $v_1 = v_2 = v_{DC} + A_x \sin(2\pi f_x t)$ and $v_3 = v_4 = v_{DC} - A_x \sin(2\pi f_x t)$ for scanning about the inner axis; or $v_4 = v_1 = v_{DC} + A_y \sin(2\pi f_y t)$ and $v_2 = v_3 = v_{DC} - A_y \sin(2\pi f_y t)$ for the outer axis. For each DC bias, the scanning was tuned to resonance by adjusting the frequency of the differential voltage (f_x or f_y). The differential voltage amplitude (A_x or A_y) was fixed to 2 volts throughout the measurement for both the inner and outer axes. Figure 4-3 plots the measured results, where the circles represent experimental data, and the solid lines are theoretical fittings. To calculate theoretical fittings according to analytical equations, experimental (best-fit) values, rather than theoretically calculated or designed values, of the mirror-electrodes distance D_0 (130 μm), the moments of inertia I_i (1.19E-15 $\text{kg}\cdot\text{m}^2$) and I_o (2.21E-15 $\text{kg}\cdot\text{m}^2$), and the spring constants K_i (1.07E-8 $\text{N}\cdot\text{m}$) and

K_o ($2.91\text{E-}9$ N·m) were used. Later in this chapter, fitting analytical equations to experimental data will be discussed.

Frequency Response

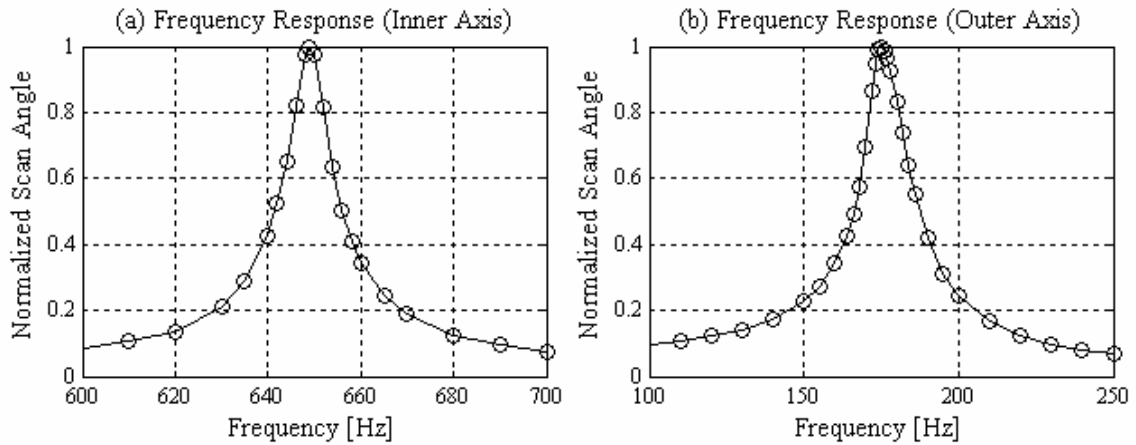


Figure 4-4. Frequency response measurement. $v_{DC} = 120$ V. (a) Inner axis, $A_x = 4$ V; (b) Outer axis, $A_y = 2$ V.

Frequency response is the dependence of the scan angle on the frequency of the differential voltage at a given DC bias. In this measurement, the DC bias was set to 120 volts for both the inner and outer axes while the differential voltage amplitude was 4 volts for scanning the inner axis and 2 volts for the outer axis. Figure 4-4 plots the measured frequency response. It can be seen that, under the given test conditions, the resonant frequencies were 649 Hz and 175 Hz for the inner and outer axes, respectively. In scanned-beam imaging systems, this result provides a line resolution of approximately 325 lines/frame if the inner axis is operated at resonance (649 Hz) and the outer axis is driven by a sawtooth waveform at 2 Hz. These plots were also used to measure the Q-factors of the scanning axes, which are defined as the center frequency divided by

FWHM's (full width at half maximum) of the frequency response curves. The measured results are listed in Table 4-1.

Table 4-1. Measured Q-factors of the inner and outer scanning axes.

Q-factor of the inner axis	$Q_i \approx 45$
Q-factor of the outer axis	$Q_o \approx 8$

One-sided DC Drive

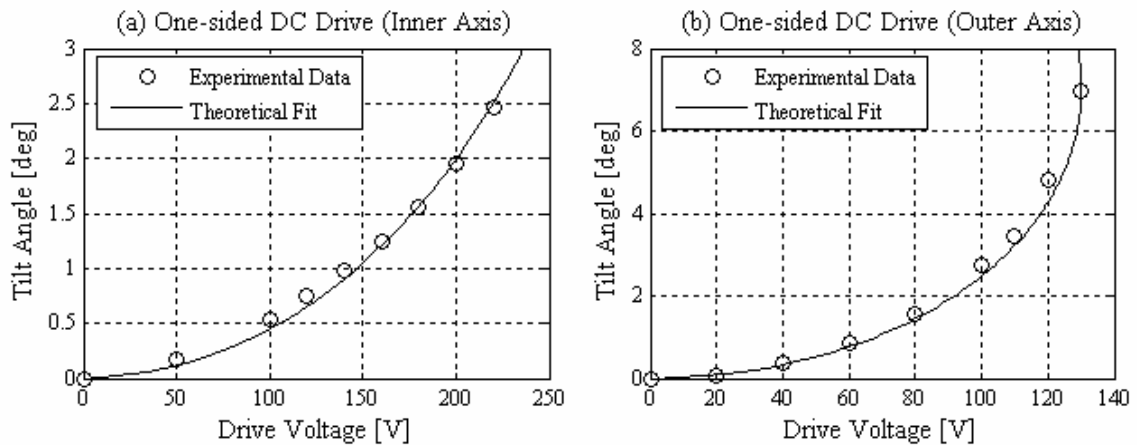


Figure 4-5. Tilt angle versus one-sided DC voltage. The circles are experimental data, and the solid lines are theoretical fittings.

The maximum angular displacements about the two orthogonal axes are another set of important specifications in addition to the resonant frequencies. A simple method to measure the achievable angular displacements is to drive the mirror about one axis at a time by applying a DC voltage to half side of it. That is, $v_1 = v_2 = V$ and $v_3 = v_4 = 0$ while the mirror is tilted about the inner axis; or $v_4 = v_1 = V$ and $v_2 = v_3 = 0$ about the outer axis. The measured mechanical tilt angle versus the one-sided DC drive voltage is

plotted in Figure 4-5, where the circles represent experimental data, and the solid lines are theoretical fittings. Theoretical fittings will be discussed later in this chapter. The quadratic-like relationship is due to the electrostatic attractive torque being proportional to the square of the drive voltage.

Quasi-static Scan

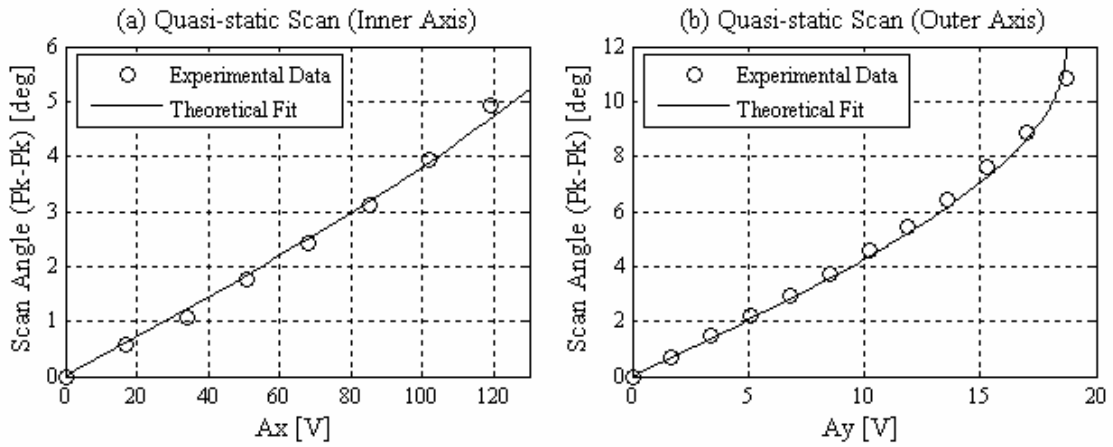


Figure 4-6. Peak-to-peak mechanical scan angle versus differential voltage amplitude (A_x or A_y) at quasi-static scan. The circles are experimental data, and the solid lines are theoretical fittings. $v_{DC} = 120$ V. (a) Inner axis, $f_x = 20$ Hz; (b) Outer axis, $f_y = 20$ Hz.

In real operation, the 3-D mirror is driven with a DC bias mixed with two differential voltages corresponding to scans about the two orthogonal axes respectively. For scanning about only one axis at a time, driven with a sinusoidal differential voltage, the drive voltages can be expressed as $v_1 = v_2 = v_{DC} + A_x \sin(2\pi f_x t)$ and $v_3 = v_4 = v_{DC} - A_x \sin(2\pi f_x t)$ for scanning about the inner axis; or $v_4 = v_1 = v_{DC} + A_y \sin(2\pi f_y t)$ and $v_2 = v_3 = v_{DC} - A_y \sin(2\pi f_y t)$ for the outer axis. In this measurement, the DC bias v_{DC} was set to 120 volts while the differential voltage

frequency (f_x or f_y) were 20 Hz, which was low enough for quasi-static scan. Figure 4-6 plots the measured peak-to-peak mechanical scan angle versus the differential voltage amplitude (A_x or A_y) at quasi-static scan for the inner and outer axes, respectively. The circles represent experimental data, while the solid lines are theoretical fittings. Theoretical fittings will be discussed later in this chapter.

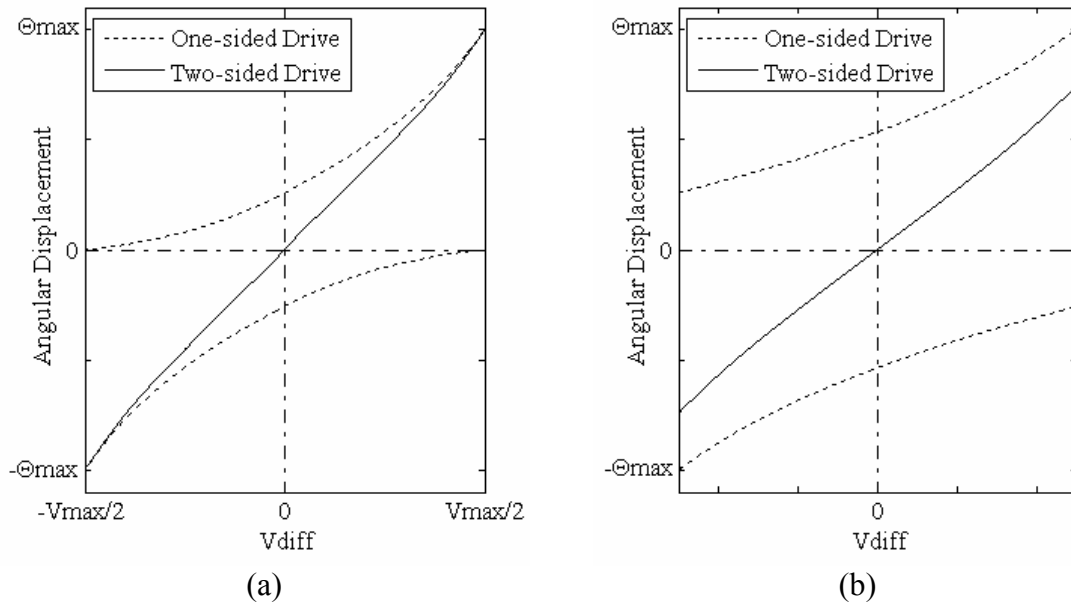


Figure 4-7. Illustration of linearization of two-sided drive. (a) $v_{DC} = V_{max} / 2$; (b) $v_{DC} > V_{max} / 2$.

It can be seen that, compared to one-sided drive, two-sided drive produces a much more linear relationship between the scan angle and the differential voltage, which is only curved when the outer axis is approaching the snap-down point. The linearization is a desirable operating characteristic and has been predicted by the device mechanical model developed in Chapter 2. Here, a graphical analysis is used to illustrate the linearization.

Suppose Θ_{\max} is the maximum angular displacement obtained by the maximum one-sided voltage V_{\max} used to drive the mirror. For two-sided drive, $v_l = v_{DC} + v_{diff}$ is applied to one half side of the mirror, while $v_r = v_{DC} - v_{diff}$ to the other side. If the DC bias v_{DC} is set to $V_{\max} / 2$, then the differential voltage v_{diff} can run from $-V_{\max} / 2$ to $V_{\max} / 2$. For the two extreme cases of $v_{diff} = \pm V_{\max} / 2$, the two-sided drive becomes one-sided drive; and the angular displacement is $\pm \Theta_{\max}$, respectively. For intermediate values of v_{diff} , the effect of the two-sided drive is the sum of two one-sided drives, one of which drives the mirror to positive angular displacement with voltage v_l ; and the other drives the mirror to negative angular displacement with voltage v_r . Figure 4-7 (a) shows the two-sided drive and the two one-sided drive components. It can be seen that the two non-linear curves of the one-sided drives combine to a very linear curve for the two-sided drive. This phenomenon results from the symmetric nature of the two-sided drive. Figure 4-7 (b) illustrates the case of $v_{DC} > V_{\max} / 2$, which also comes to a very linear response. In this situation, when $v_l = V_{\max}$, $v_r > 0$ and vice versa, therefore, at those points, the angular displacement is less than Θ_{\max} .

Resonant Scan

In quasi-static operation, the outer axis has achieved more than 10° peak-to-peak mechanical scan angle within reasonable drive voltages. However, it was not the case for the inner axis. In Figure 4-6 (a), the peak-to-peak scan angle was only 4° when the differential voltage amplitude reached 120 volts. In real applications, the drive voltages

should be kept low because high voltages are often not practical and could break the fragile MEMS mirror by electrical shorting (break-down) or destruction when the mirror snaps down. Fortunately, resonant scan can significantly lower drive voltages. Therefore, the inner axis resonance was designed near the operating frequency.

To measure the resonant scan behavior, the 3-D mirror was operated in the same way as the quasi-static scan except for that the frequency of the differential voltage was set to resonance. For the inner axis, the DC bias was 120 volts and the differential voltage frequency was 649 Hz. For the outer axis, they were 40 volts and 260 Hz. Figure 4-8 plots the measured peak-to-peak mechanical scan angle versus the differential voltage amplitude (A_x or A_y) at resonant scan for the inner and outer axes, respectively. It can be seen that the resonant response is very linear, which is a desirable operating characteristic and can be predicted analytically.

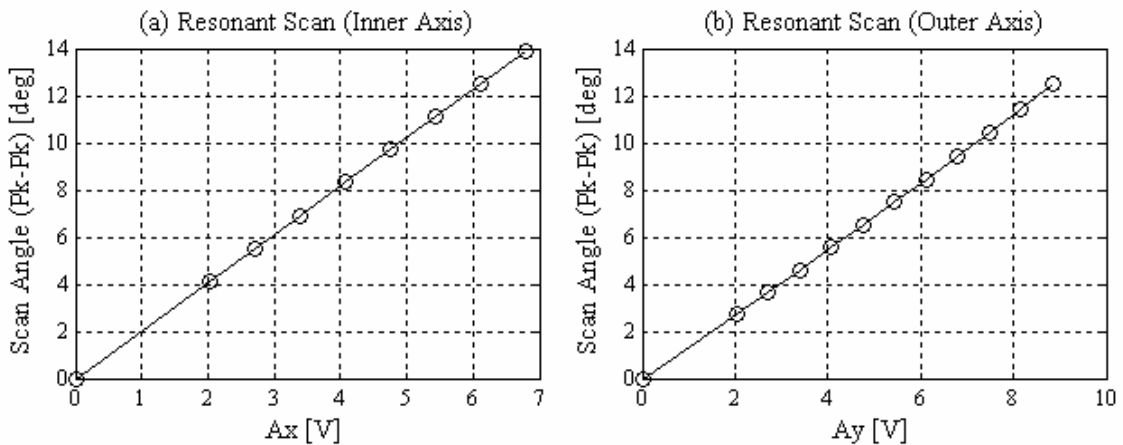


Figure 4-8. Peak-to-peak mechanical scan angle versus differential voltage amplitude (A_x or A_y) at resonant scan. (a) Inner axis, $v_{DC} = 120$ V, $f_x = 649$ Hz; (b) Outer axis, $v_{DC} = 40$ V, $f_y = 260$ Hz.

Simultaneous Biaxial Scanning

In previous measurements, the 3-D mirror was scanned only about one axis at a time to characterize the inner and outer scan axes separately. In real applications, the two orthogonal axes are usually driven simultaneously with the inner axis scanning resonantly and the outer axis quasi-statically. For sinusoidal differential voltages, the biaxial drive voltages can be expressed in the following form for the four-quadrant drive electrodes.

$$v_1 = v_{DC} + A_x \sin(2\pi f_x t) + A_y \sin(2\pi f_y t); \quad v_2 = v_{DC} + A_x \sin(2\pi f_x t) - A_y \sin(2\pi f_y t);$$

$$v_3 = v_{DC} - A_x \sin(2\pi f_x t) - A_y \sin(2\pi f_y t); \quad v_4 = v_{DC} - A_x \sin(2\pi f_x t) + A_y \sin(2\pi f_y t).$$

Biaxial drive with these voltages can cause cross coupling between the two scanning axes due to nonlinear dependence of the scan angle on the mirror-electrodes distance and the drive voltages, which distorts the scan pattern from an ideal rectangle. For our case, the inner axis scans at its resonance, which is much higher than the resonant and operating frequencies of the outer axis; therefore the cross coupling effect does not affect the outer axis significantly.

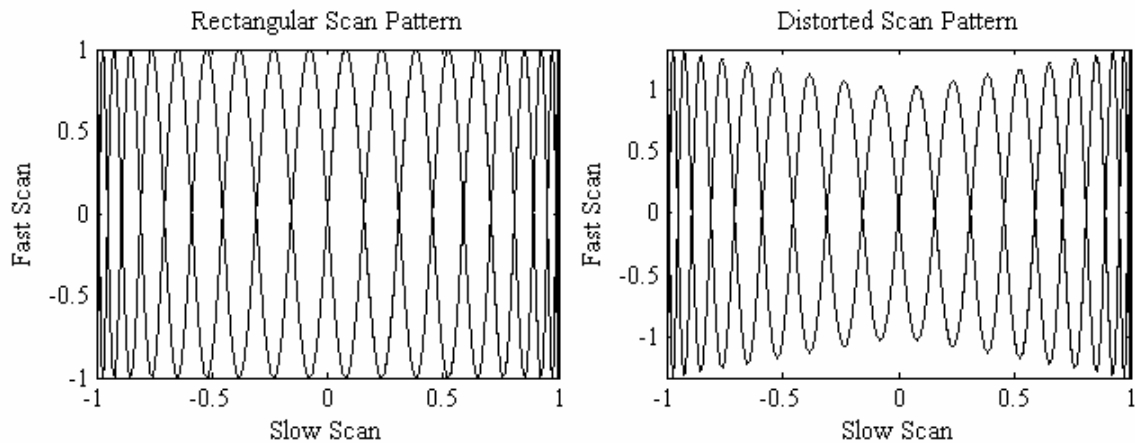


Figure 4-9. Rectangular and distorted scan patterns.

Figure 4-9 is a representative graph to show the cross coupling effect, where the left graph shows an ideally rectangular scan pattern, and the right graph is a distorted pattern, in which the fast axis achieves larger scan angles when the slow axis has a larger angular displacement (pincushion distortion). A distortion coefficient can be defined as follows to describe this effect quantitatively.

$$Distorsion = \left(\frac{\theta_1 + \theta_2}{2\theta_0} - 1 \right) \times 100\%,$$

where θ_0 , θ_1 and θ_2 are scan angles of the fast axis when the slow axis has zero, most negative or most positive angular displacements, respectively.

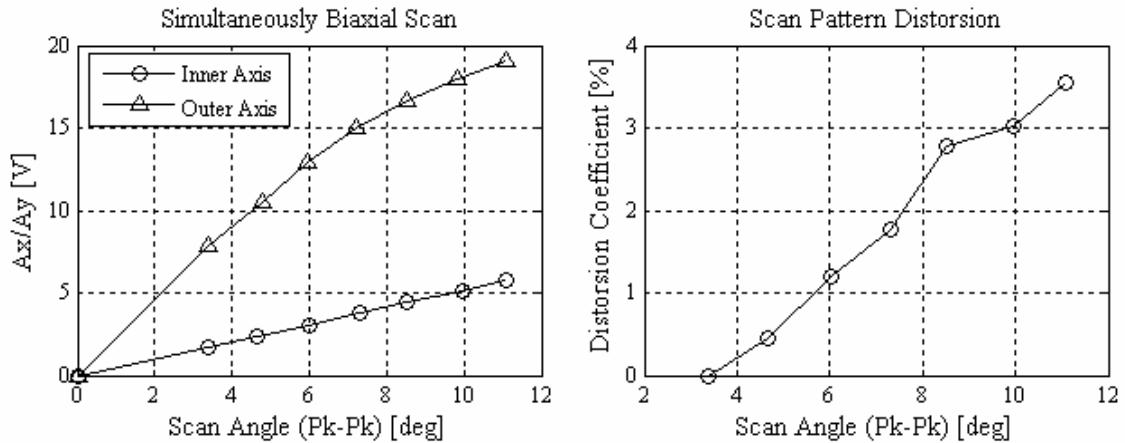


Figure 4-10. Simultaneously biaxial scan. $v_{DC} = 120$ V, $f_x = 650$ Hz, $f_y = 25$ Hz.
 (a) Differential voltage amplitude (A_x or A_y) versus peak-to-peak mechanical scan angle;
 (b) Distorsion coefficient versus peak-to-peak mechanical scan angle.

To measure the scan distortion of the 3-D mirror, the two orthogonal axes were scanned simultaneously, with the inner axis near resonance ($f_x = 650$ Hz) and the outer axis quasi-statically ($f_y = 25$ Hz). The fast scan frequency was chosen to be a multiple of

the slow one to maintain a stationary scan pattern. In this measurement, the DC bias v_{DC} was set to 120 volts while the differential voltage amplitudes A_x and A_y were scanned with a set of consecutive values for maintaining square scan patterns with increasing scan angles. Figure 4-10 plots A_x and A_y in pairs as well as the distortion coefficient versus the peak-to-peak mechanical scan angle. It can be seen that the distortion coefficient is less than 4% for scan angles over 10° (peak-to-peak). When the 3-D mirror is used in a scanned-beam imaging system, pincushion distortion in the scan pattern produces barrel distortion in the image, which can be corrected by subsequent digital processing. To obtain an ideally rectangular scan pattern, the differential voltage amplitude A_x can be made decreasing while the slow scan angle is increasing to balance out the cross coupling effect.

Deriving Mechanical Parameters from Measured Torsion Behavior

The torsion behavior of the 3-D mirror can be predicted according to the device mechanical model and the equation of motion (refer to Chapter 2) with known mechanical parameters. Mechanical parameters affecting the torsion behavior include the device geometrical dimensions, the moments of inertia of the silicon plates, the spring constants of the hinges, and the mirror-electrodes distance. Actual values the moments of inertia and the spring constants may deviate from the theoretically calculated values due to variations in material properties, silicon plate dimensions, silicon nitride film thickness, etc. In the meantime, the mirror-electrodes distance can also deviate from the design value and cannot be easily measured once the mirror is mounted. However, it is possible to derive these mechanical parameters from the measured torsion behavior by

fitting theoretical curves to experimental data. To clarify dependence of the torsion behavior on the mechanical parameters, they are expressed in forms of pseudo-functions in Table 4-2 (refer to Chapter 2 for the analytical expressions), where D_0 is the mirror-electrodes distance; I_i and I_o are the moments of inertia of the inner and outer plates; K_i and K_o are the spring constants of the inner and outer hinges. The corresponding experimentally measured graphical curves are also expressed in forms of pseudo-functions.

Table 4-2. Dependence of torsion behavior on mechanical parameters.

	Theoretical curves	Experimental curves
Resonant frequency vs. DC bias (inner axis)	$f_i = f_i(v_{DC}; D_0, I_i, K_i)$	$f_i^{\text{exp}} = f_i^{\text{exp}}(v_{DC})$
Resonant frequency vs. DC bias (outer axis)	$f_o = f_o(v_{DC}; D_0, I_o, K_o)$	$f_o^{\text{exp}} = f_o^{\text{exp}}(v_{DC})$
Scan angle vs. differential voltage at quasi-static scan (inner axis)	$\theta_i = \theta_i(A_x; D_0, K_i)$	$\theta_i^{\text{exp}} = \theta_i^{\text{exp}}(A_x)$
Scan angle vs. differential voltage at quasi-static scan (outer axis)	$\theta_o = \theta_o(A_y; D_0, K_o)$	$\theta_o^{\text{exp}} = \theta_o^{\text{exp}}(A_y)$

To find the optimum values of D_0 , I_i , I_o , K_i and K_o that best-fit the theoretically calculated curves to the experimentally measured curves, a merit function is defined as follows.

$$\begin{aligned}
M(D_0, I_i, I_o, K_i, K_o) = & \\
& \frac{1}{v_{DCx2} - v_{DCx1}} \int_{v_{DCx1}}^{v_{DCx2}} (f_i(v_{DC}; D_0, I_i, K_i) - f_i^{\text{exp}}(v_{DC}))^2 dv_{DC} + \\
& \frac{1}{v_{DCy2} - v_{DCy1}} \int_{v_{DCy1}}^{v_{DCy2}} (f_o(v_{DC}; D_0, I_o, K_o) - f_o^{\text{exp}}(v_{DC}))^2 dv_{DC} + \\
& \frac{1}{A_{x2} - A_{x1}} \int_{A_{x1}}^{A_{x2}} (\theta_i(A_x; D_0, K_i) - \theta_i^{\text{exp}}(A_x))^2 dA_x + \\
& \frac{1}{A_{y2} - A_{y1}} \int_{A_{y1}}^{A_{y2}} (\theta_o(A_y; D_0, K_o) - \theta_o^{\text{exp}}(A_y))^2 dA_y
\end{aligned}$$

In this expression, all of the experimental curves are normalized to range [0, 1] and their corresponding theoretical curves are scaled accordingly. Parameters v_{DCx1} , v_{DCx2} , v_{DCy1} , v_{DCy2} , A_{x1} , A_{x2} , A_{y1} , and A_{y2} represent the minimum and maximum experimental points. In the process known as regression, parameters D_0 , I_i , I_o , K_i and K_o are adjusted based on the value of the merit function until a smallest value is obtained, thus producing a best-fit with the corresponding parameters giving the smallest value of the merit function known as the best-fit parameters [28]. Table 4-3 lists the experimental (best-fit) values of D_0 , I_i , I_o , K_i and K_o derived from the experimental data along with the designed or theoretically calculated.

Table 4-3. Experimental and theoretical values of the mechanical parameters.

Mechanical parameters	Experimental (best-fit) values	Theoretical/ designed values
D_0 (mirror-electrodes distance) [μm]	130	150
I_i (moment of inertia of the inner plate) [$\text{kg}\cdot\text{m}^2$]	1.19E-15	1.42E-15

I_o (total moment of inertia of the inner plate and the gimbal ring) [kg·m ²]	2.21E-15	3.25E-15
K_i (spring constant of the inner hinges) [N·m]	1.07E-8 8.53E-9 (one-sided DC drive)	1.82E-8
K_o (spring constants of the outer hinges) [N·m]	2.91E-9 3.11E-9 (one-sided DC drive)	4.10E-9
Note: The material properties in Table 2-2 and the device dimensions in Table 2-3 (with inner hinge length $L_{ih} = 23 \mu\text{m}$) were used for calculating the theoretical values of the mechanical parameters.		

The smaller experimental values of the moments of inertia I_i and I_o result from the thinner final device thickness and silicon undercutting in the release process which reduce the mass of the mirror plates. The smaller experimental values of the spring constants K_i and K_o can be caused by variations in silicon nitride material properties and film thickness. Another reason is silicon undercutting beneath the hinges, which make the hinges have longer effective lengths.

The experimental values of D_0 , I_i , I_o , K_i and K_o were used to draw the theoretical fitting curves according to the analytical equations for the torsion behavior. Inconsistence between the theoretical and experimental curves is due to the initial mirror tilt and misalignment between the mirror and the drive electrodes, as well as the incomplete electric field analysis which neglects angle-dependent effects. The spring constants used to plot the theoretically fitting curves for the one-sided DC drives are a bit different because they are not included in the merit function. Due to the asymmetric

nature of the one-sided DC drive, it is more sensitive to the initial mirror tilt and misalignment than the symmetric quasi-static scan driven by a DC bias and a differential voltage, although either of them can be used to find the experimental values of D_0 , K_i and K_o .

Summary

The 3-D mirror has achieved more than 10° peak-to-peak mechanical scan angles about both axes, with the inner axis scanning resonantly and the outer axis quasi-statically. Given the optical aperture of $700\ \mu\text{m}$, this angular scan range corresponds to $N_x = N_y = 488$ resolvable spots assuming the illumination wavelength is $500\ \text{nm}$. In the measurements, the DC bias was set to 120 volts and the differential voltage was less than 7 volts for the inner axis and less than 20 volts for outer axes, respectively. This angular scan range is useful for a lot of applications. When the 3-D mirror is used in a scanned-beam imaging system, the scan angles translate into optical resolutions where greater scan angles represent finer resolutions. Simultaneously biaxial scan was characterized for the cross coupling effect between the inner and outer axes. The distortion coefficient was less than 4% for square scan patterns of more than 10° peak-to-peak mechanical scan angles, which is insignificant for most applications and can be corrected electrically or digitally.

Characterization of the Deformable Membrane

The optical reflecting surface at the center of the 3-D mirror is made of a gold-coated silicon nitride deformable membrane. The membrane mirror works as a positive

lens of variable focal length and can also correct residual spherical aberration by bending the membrane with a quartic curvature accordingly. A tabletop Mirau interferometer is used to measure the surface shape of the membrane. A cross section of the measured surface shape is fit to a polynomial with quadratic and quartic terms as below.

$$z = a_2 r^2 + a_4 r^4.$$

The coefficient a_2 is related to the effective focal length by $f = 1/4a_2$ and a_4 represents the primary spherical aberration of the mirror introduced to the wavefront. In some applications, the coefficient a_4 should be kept close to zero to minimize aberration. In other cases, finite a_4 may be used to correct the system aberration. For all cases, inaccuracy of the surface shape will introduce aberrations into the system. The magnitude of acceptable aberration is determined by the intended application. Here, $\lambda/10$ is adopted as a target maximum amount of optical aberration which can be introduced by the membrane mirror. Because the mirror introduces twice the aberration into the reflected optical wavefront, $\lambda/20$ is the maximum allowable mirror surface aberration. The range of variable focal length is determined by the maximum membrane deflection at a given diameter and the ability to zero out aberration at that deflection.

Imaging Interferometer

Deflection of the deformable membrane is on the order of a few microns, which meets the surface profiling capability of an optical interferometer using a HeNe laser or diode laser illumination source. Therefore, a tabletop imaging interferometer illustrated in Figure 4-11 is used to measure the surface shape of the membrane. When the circular bended membrane is perfectly normal to the optical axis, the fringes show up as

concentric rings where each ring is separated by a height difference of one half of the illumination wavelength. With this configuration, a measure of the surface profile can be obtained by measuring the fringe spacing.

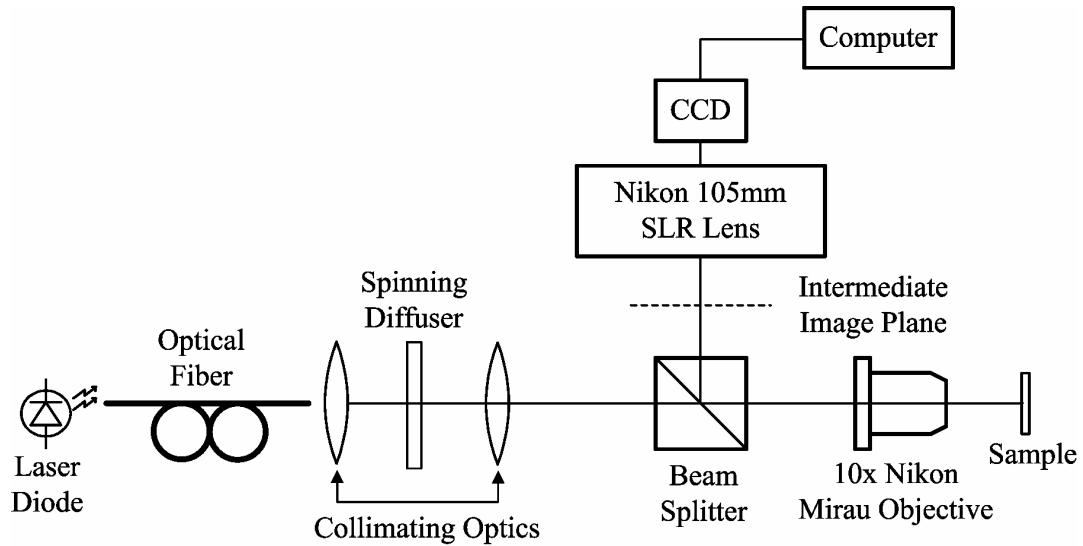


Figure 4-11. Optical profilometer setup using a Mirau interferometer objective lens.

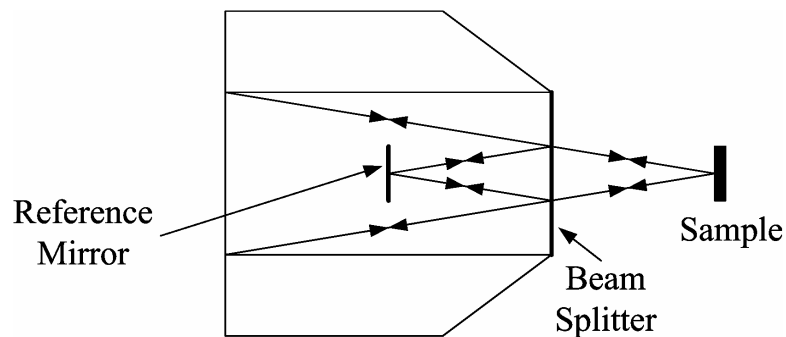


Figure 4-12. Schematic of the Mirau interferometer.

The kernel of the tabletop imaging interferometer is a Mirau interferometric Nikon M-Plan 10x DI microscope objective, which is shown in Figure 4-12. The illumination source is a Philips CQL806 30mW laser diode with an operating wavelength

of 675 nm and a temporal coherence length of several millimeters, which provides a sufficient depth of field to make clear interference patterns for the membrane with deflections of a few microns. The light is coupled into a single mode fiber to provide a Gaussian light source and is then collimated to match the size of the membrane. The spinning diffuser is used to reduce the spatial coherence of the laser source, which can produce speckles on the image. The light passes through the beamsplitter and the interferometric objective and then reaches the membrane surface. The reflected light from the membrane surface interferes with the reflected light from the reference mirror inside the interferometric objective and is redirected by the beamsplitter to the imaging end. The interference pattern is imaged onto the CCD camera by the 105 mm Nikon SLR lens.

Phase-shift Interferometry

In a regular interferometer, the surface height difference between neighboring fringes is $\lambda/2$, which is in submicron order for a illumination source of visible spectrum. This is not quite sufficient for measuring small deflections. To improve the measurement accuracy, phase-shift interferometry is used. For a height difference h between the sample and reference surfaces, the phase difference between the beams reflected from these two surfaces is $\varphi = 4\pi h / \lambda$. In phase-shift interferometry, the phase difference is computed from multiple interference images obtained when the sample is translated along the optical axis, thus the relative phase is shifted, by a known amount. For the five-frame method, interference images are taken for five relative phase shifts of $-\pi$, $-\pi/2$, 0 , $\pi/2$, and π . Given the intensity of each interference image is $I_1(x, y)$, $I_2(x, y)$, $I_3(x, y)$, $I_4(x, y)$, and $I_5(x, y)$, the phase profile of the sample surface is given by [41]

$$\varphi(x, y) = \tan^{-1} \left\{ \frac{2[I_2(x, y) - I_4(x, y)]}{2I_3(x, y) - I_5(x, y) - I_1(x, y)} \right\}.$$

As the phase profile obtained by this method has an ambiguity of $2N\pi$ (N is an integer), the unwrapping calculation is carried out on the assumption that the height changes continuously. The measurement accuracy of surface shape using phase-shift interferometry can achieve sub-nanometer order [29]. The tabletop phase-shift imaging interferometer used for characterizing the deformable membrane had an accuracy of about 5 nm, which is sufficient for measuring surface shapes of the membrane.

Membrane Deflection Measurement

For the 3-D mirror tested in this section, the silicon nitride deformable membrane has a diameter of 750 μm , a thickness of approximately 1 μm and a residual stress of roughly 40 MPa, with the depth of the cavity between the membrane and the silicon substrate being about 12 μm . Refer to the membrane design section of Chapter 2 for detailed design parameters of the deformable membrane. In this measurement, the membrane was actuated with uniform load, that is, the inner and outer electrodes were applied to the same actuation voltage simultaneously. Figure 4-13 shows an interference image of the membrane mirror with no applied voltage and again with an actuation voltage of 240 volts. Each fringe represents a height difference of $\lambda/2$, which is 337.5 nm for the illumination source in use. Figure 4-14 plots line-profiles corresponding to the interference images.

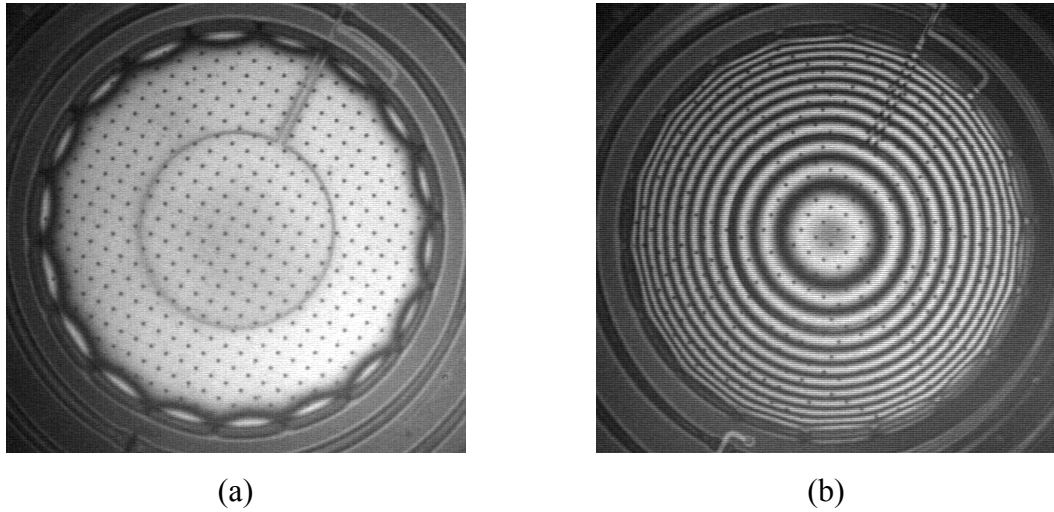


Figure 4-13. Surface interference images. (a) Actuation voltage = 0 V; (b) Actuation voltage = 240 V.

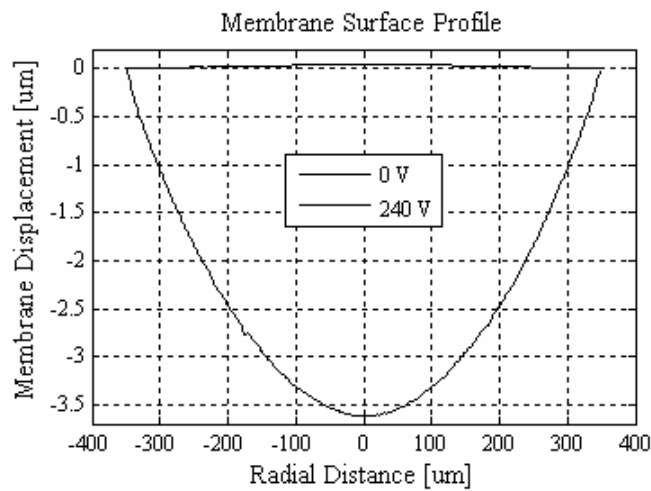


Figure 4-14. Surface line-profiles of the deformable membrane. The top line was actuated at 0 volt and the bottom line at 240 volts.

Figure 4-15 plots the membrane center displacement versus the actuation voltage. This mirror achieved a maximum displacement of $3.74 \mu\text{m}$ at the membrane center with an actuation voltage of 242 volts. Pull-in effect limited the maximum displacement to approximately $4 \mu\text{m}$. The effective focal length f_{mir} of the mirror is equal to half the

radius of curvature of the membrane and is given by $f_{mir} = D^2/16\delta$ where $D = 700 \mu\text{m}$ is the diameter of the membrane and δ is the center displacement. From this relationship, we obtain a range of focal lengths from $f_{mir} = \infty$ for $\delta = 0$ (no displacement) to $f_{mir} = 8.2 \text{ mm}$ for $\delta = 3.74 \mu\text{m}$.

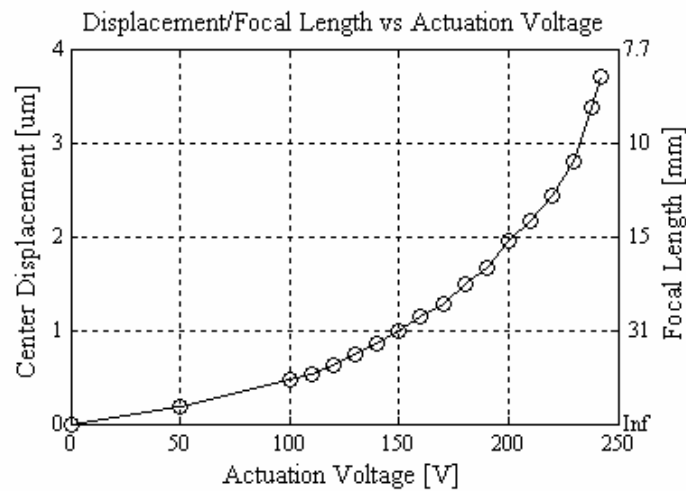


Figure 4-15. Membrane deflection/focal length versus actuation voltage.

Spherical Aberration Measurement

For an infinite conjugate ratio, a concave mirror must have a parabolic surface shape to achieve aberration-free on-axis imaging. However, the actual surface shape of the deformable membrane mirror may deviate from a perfect parabola. This will introduce spherical aberration to the reflected optical wavefront. The top line in Figure 4-16 plots the optical aberration of the membrane mirror with uniform loading, where the aberration is expressed in number of waves at 675 nm wavelength. The mirror surface aberration is half of the optical aberration. Surface shape data suggest that the margin of

the membrane mirror deviates more from a parabola and thus introduces more aberrations, which indicates that the aberration can be reduced by limiting the pupil size rather than using the full pupil. The bottom line in Figure 4-16 shows the optical aberration when using 90% pupil of the membrane mirror. This results in aberrations below 0.12λ through the full range of deflection. To achieve aberrations below $\lambda/10$, the membrane can be actuated with nonuniform loading by applying different voltages to the inner and outer electrodes [22].

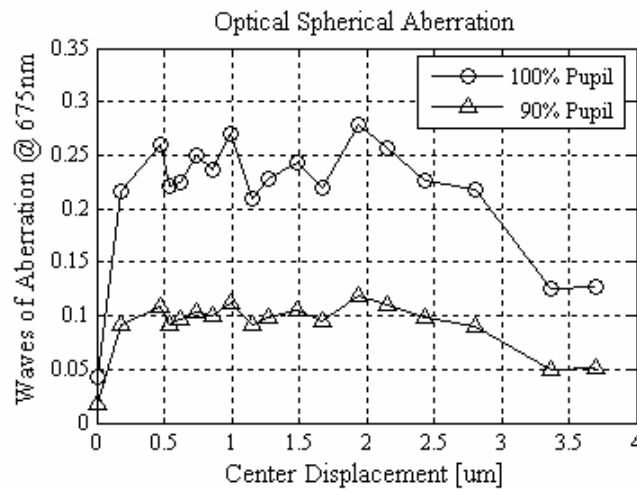


Figure 4-16. Optical spherical aberration with uniform loading. The top line is for full pupil, and the bottom line is for 90% pupil.

Initial Shape of the Membrane

Another important characteristic of the deformable membrane is the initial shape, which designates the surface shape when no actuation voltage applied. The membrane shows some initial curvature due to a stress gradient in the silicon nitride film and the metal bi-layer (gold/chrome). The low-stress silicon nitride (~ 40 MPa tensile stress)

allows for lower-voltage actuation than more highly stressed films, but initial flatness could be improved with a higher stress in the film. Figure 4-17 plots the initial surface shape with no applied actuation voltage, which shows that the maximum displacement across the membrane is less than 50 nm peak-to-peak. The solid line is the measured surface shape and the dotted line is the fourth-degree polynomial fit.

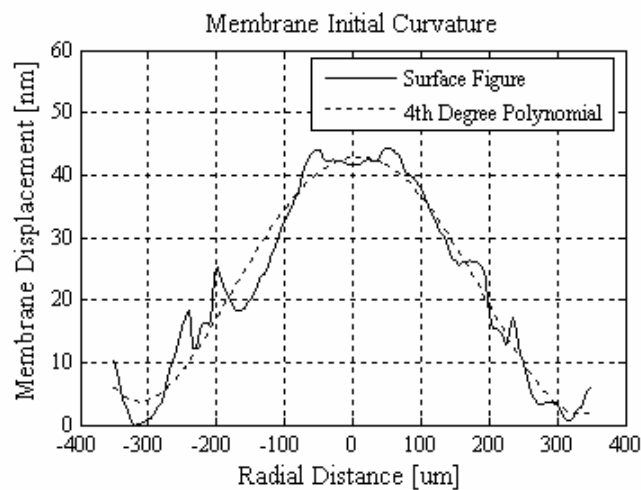


Figure 4-17. Initial surface shape of the membrane. The solid line is the measured surface shape, and the dotted line is the fourth-degree polynomial fit.

Lateral and Depth Resolution of the 3-D Mirror

Characterization results of the 3-D mirror have been discussed in previous sections. The mirror has achieved a zero-to-peak mechanical scan angle of more than $\pm 5^\circ$ for both axes and the deformable membrane can deflect over $3.5 \mu\text{m}$ with a $12 \mu\text{m}$ cavity underneath it. When the 3-D mirror is used in an optical imaging system, these numbers translate to lateral and depth resolutions. Discuss here is in a general sense rather than for a specific application, and the computation only provides an evaluation of the

performance of the mirror. In Chapter 5, optical resolutions will be calculated specifically in the context of a confocal laser scanning microscope.

Lateral Resolution

For a uniformly illuminated circular mirror of diameter D , the far-field diffraction pattern is the Airy function with an angular full width at half maximum $\theta_{FWHM} \cong \lambda / D$.

For a mirror with zero-to-peak mechanical scan angle θ_{scan} the lateral number of resolvable spots may be computed as

$$N_x = N_y = \frac{4\theta_{scan}}{\theta_{FWHM}} = \frac{4D\theta_{scan}}{\lambda},$$

where the optical scan angle is assumed to be twice the mechanical scan angle. This is true for both scan axes with near-normal incidence of the optical beam. For the mirror described here with $D = 700 \mu\text{m}$ and $\theta_{scan} = 5^\circ$, we calculate $N_x = N_y = 488$ resolvable spots using this criterion with $\lambda = 0.5 \mu\text{m}$.

Depth Resolution

A similar measure for z-axis motion of the beam focus is the number of depth-of-focus distances over which the focus can be moved. This measure is dependent on the optical system. Considered here is that a membrane mirror with variable focal length f_{mir} is located near a primary focusing lens with focal length f_{lens} so that the wavefront curvature induced by the membrane mirror is added to the wavefront curvature provided by the primary lens. Furthermore, it is assumed that the focal length of the membrane mirror is large compared to that of the primary lens, and that the incident Gaussian beam

is collimated. In that case, after reflecting from the membrane mirror and passing through the lens, the location of the beam focus s is given by

$$s = \left(\frac{1}{f_{lens}} + \frac{1}{f_{mir}} \right)^{-1}.$$

For a range of values of f_{mir} from infinity to f_{min} the corresponding range of focus is

$$\Delta s = s_{max} - s_{min} = \frac{f_{lens}^2}{f_{lens} + f_{min}}.$$

The depth-of-focus d can be taken as twice the Rayleigh range of the Gaussian beam. If the membrane mirror is illuminated by a Gaussian beam with the $1/e^2$ intensity radius coincident with the mirror radius, then $d = 8\lambda s^2 / \pi D^2 = 8\lambda f_{lens}^2 / \pi D^2$ for $f_{mir} = \infty$. The focus control number of depth-of-focus distances $N_z = \Delta s / d$ can be expressed in terms of the membrane center displacement δ using $f_{min} = D^2 / 16\delta_{max}$ to find

$$N_z = \frac{\Delta s}{d} = \frac{\pi D^2}{8\lambda f_{min} (1 + f_{lens} / f_{min})} = \frac{2\pi\delta_{max}}{\lambda(1 + f_{lens} / f_{min})}.$$

This formula neglects the effect on d of aperture clipping of the Gaussian beam. If assuming $f_{lens} \ll f_{min}$ and using $\delta_{max} = 3.7 \mu\text{m}$, $\lambda = 0.5 \mu\text{m}$, we find for this membrane mirror a range of focus adjustment of $N_z = 46$ depth-of-focus distances. While this result is based on a simplified analysis and depends on the optical system in which the membrane mirror is used, the computation illustrates the relative range of focus adjustment that is possible using the membrane mirror.

Three-Dimensional Beam Position Demonstration

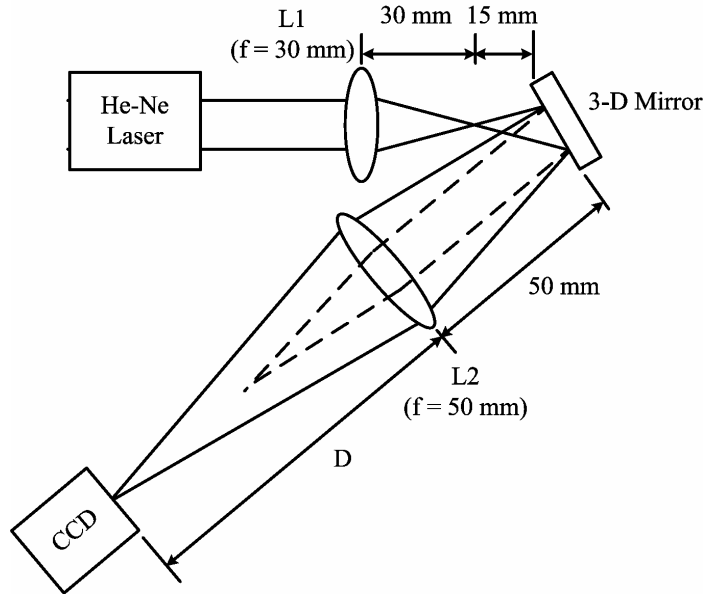


Figure 4-18. Setup for testing biaxial scanning with focus control.

Biaxial scanning along with focus control was demonstrated with the setup illustrated in Figure 4-18. The illuminating beam from a He-Ne laser is focused approximately 15 mm in front of the 3-D mirror by lens L1. The beam is reflected by the scan mirror, and then focused onto the CCD camera through lens L2. Focus adjustment is achieved with a DC voltage (V_F) applied to both the inner and outer electrodes of the deformable membrane (uniform actuation). Biaxial scanning is driven by the four-channel signal mixer/amplifier, which mixes a DC bias with two sinusoidal voltages v_x and v_y to drive the mirror scanning about the two orthogonal axes simultaneously. Stationary lissajous scan patterns can be generated with the fast scan frequency (inner hinges) being a multiple of the slow scan frequency (outer hinges). The deformable

membrane behaves as a flat mirror when the focus voltage V_F is zero. In this case, the scan pattern is focused approximately 20 cm behind lens L2. When the membrane mirror is deflected by a finite focus voltage, it is equivalent to a positive lens and will focus the scan pattern closer to lens L2.

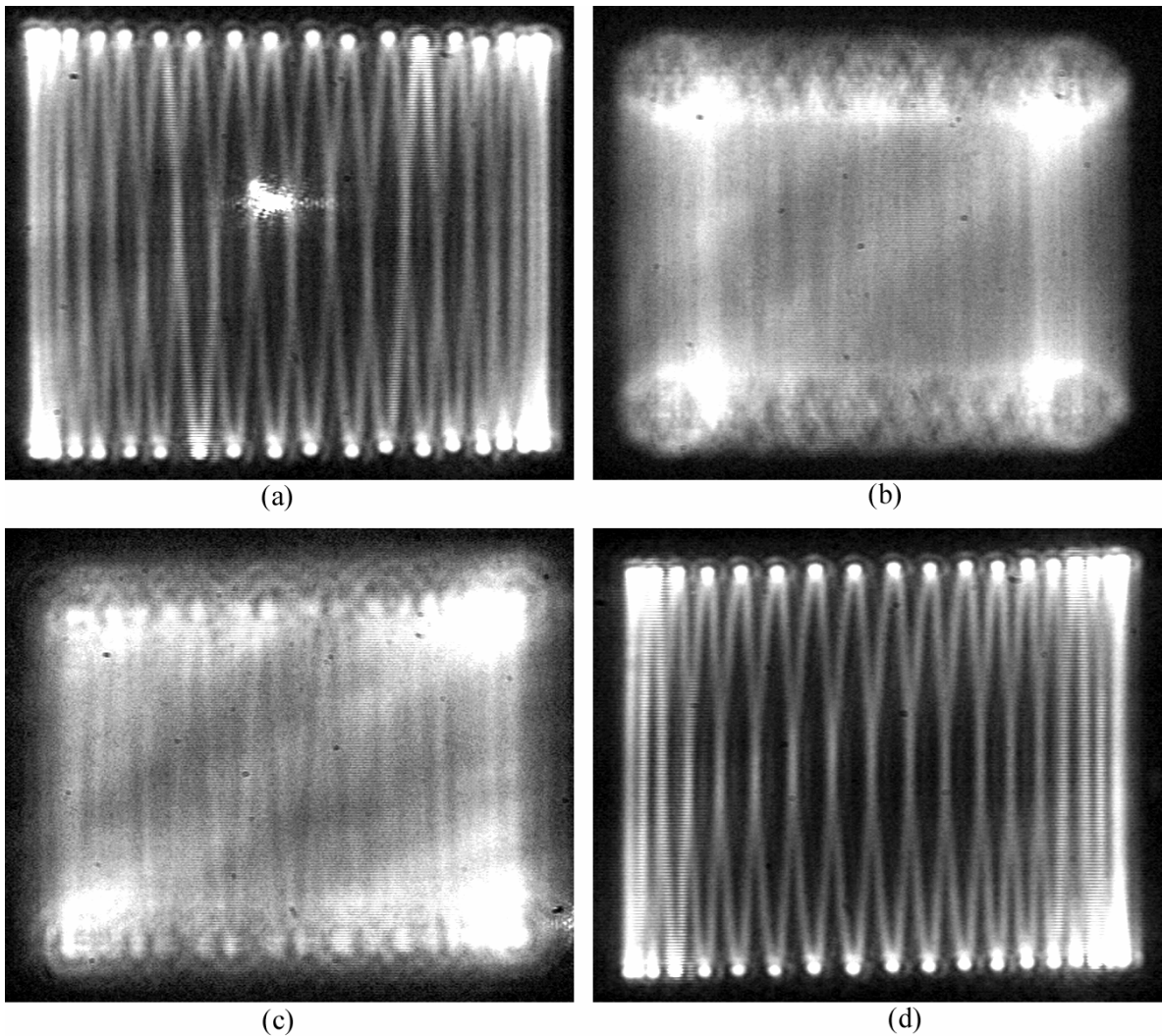


Figure 4-19. Lissajous scan patterns. (a) $V_F = 0$ volt, $D = 19$ cm; (b) $V_F = 0$ volt, $D = 7$ cm; (c) $V_F = 170$ volts, $D = 19$ cm; (d) $V_F = 170$ volts, $D = 7$ cm.

Figure 4-19 shows four scan patterns, two with the focus voltage at 0 volt ($f_{mir} = \infty$) and two at 170 volts ($f_{mir} = 21$ mm). Best focus was observed with the CCD camera 19 cm and 7 cm behind lens L2 for the two focus voltage settings. Both in-focus and out-of-focus scan patterns were taken at each position for comparison. These lissajous scan patterns demonstrate the ability of the 3-D mirror to move the focus of a laser beam in a three-dimension space with one single optical surface. This allows for more simplified optical system design and more compact instrument size. In Chapter 5, the 3-D mirror will be used as a beam scanning and focus control engine for confocal laser scanning microscopy.

CHAPTER 5

CONFOCAL IMAGING USING THE 3-D MIRROR

Scanned-beam imaging system is one of the fields that can benefit from the 3-D mirror, which moves the focus of a laser beam in three dimensions with one single optical surface, potentially reducing the number of elements used in an optical system and simplifying the system design. This chapter employs confocal laser scanning microscopy (CLSM) as an application example of the 3-D mirror to study its performance. Followed by an introduction to confocal laser scanning microscopy, use of the 3-D mirror in a tabletop confocal laser scanning microscope is demonstrated to study its imaging capability and limitations. In the last section of this chapter, a miniature confocal laser scanning microscope built with the 3-D mirror and a micro objective lens is experimented with to examine the optical design of the MSU endoscopic confocal microscope.

Introduction to Confocal Laser Scanning Microscopy

Compared to conventional optical microscopy, confocal microscopy provides advantages that include the ability to control depth of field and collect sequential optical sections from thick specimens (optical sectioning). The basic key to the confocal approach is the use of a confocal lens system for imaging and spatial filtering technique to eliminate out-of-focus light.

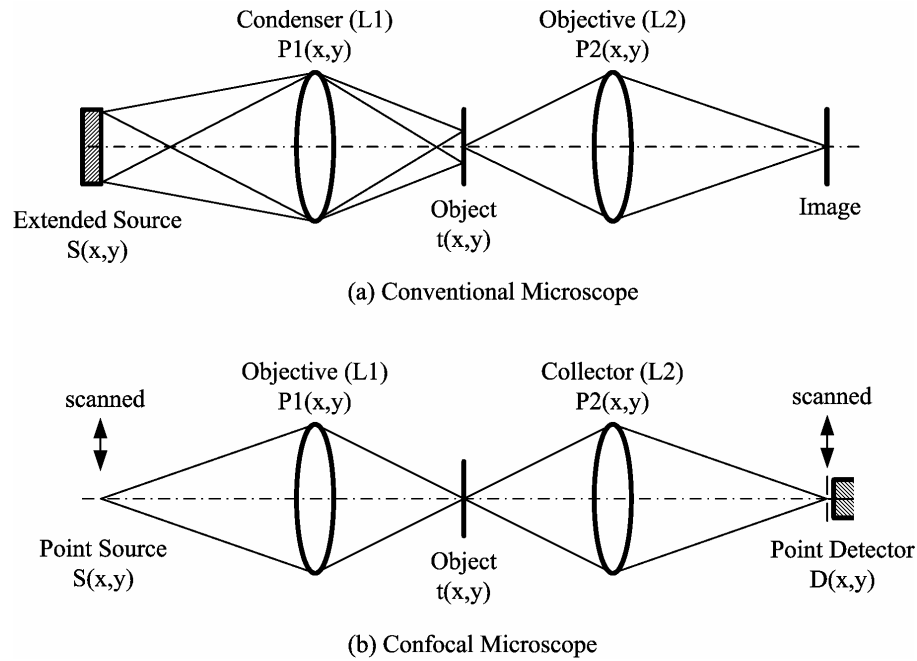


Figure 5-1. Optical arrangements of microscopes. (a) Conventional microscope. (d) Confocal microscope.

Figure 5-1 (a) illustrates the schematic of a conventional microscope, in which the object is illuminated by an extended source through a condenser. The object is then imaged by the objective lens and the final image is viewed through an eyepiece. In this case the imaging resolution is determined primarily by the objective lens, while the aberrations of the condenser are unimportant. Figure 5-1 (b) is the optical system of a confocal microscope, where the point source illuminates a single point of the object, and the point detector collects light only from the same point. An image is built up by raster-scanning the source and detector in parallel. In this configuration both lenses play equal parts in the imaging. Both theory and experiment have proved improvement of the imaging quality as two lenses are employed simultaneously to image the object. The term “confocal” is used to indicate that both lenses are focused on the same point on the object.

The differences between the conventional and confocal microscopes are listed in Table 5-1, where I is the intensity of the image; t is the amplitude transmittance of the object; h_1 and h_2 are the point spread functions of lens L1 and lens L2. In summary, the basic requirements for a confocal microscope are point source illumination (spatially coherent), point detection, a confocal lens system and a method of scanning the object.

Table 5-1. Comparison of conventional and confocal microscopes [30].

	Illumination source	Incident wave on the object	Detector	Image formation
Conventional Microscope	Extended source (incoherent)	The entire object is illuminated uniformly.	A large-area detector is located at the image plane.	$I(x, y) = h_2 ^2 \otimes t ^2$
Confocal Microscope	Point source (coherent)	Only one point on the object is illuminated at a time.	A point/pinhole detector is located at the image point conjugate to the illuminated object point.	$I(x, y) = h_1 h_2 \otimes t ^2$

The confocal microscope behaves as a coherent optical system in which the image of a point object is given by the product of the point spread function of the objective lens and that of the collector lens. This results in a sharpened image of a single point with extremely weak outer rings. A more important advantage of the confocal microscope is its depth discrimination, which allows optical sectioning of a thick specimen. Light from the specimen is focused through a small aperture, thus ensuring that information is obtained only from one particular plane of the specimen. On the other hand, a large depth

of field is often desirable for the conventional microscope, such as when observing rough surfaces.

Tabletop Confocal Microscope Using the 3-D Mirror

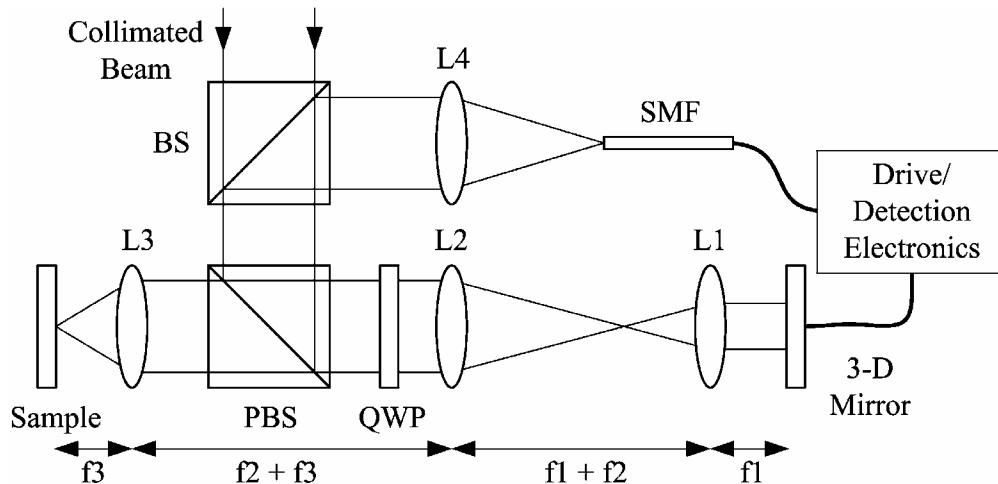


Figure 5-2. Tabletop confocal microscope using the 3-D mirror as the beam scanning and focus control device.

To demonstrate the imaging capability and limitations and measure the imaging performance of the 3-D mirror, it was used as the beam scan and focus control device in a tabletop confocal laser scanning microscope (CLSM). The optical setup is illustrated in Figure 5-2. A collimated and linearly polarized laser beam is directed onto the 3-D mirror through the beamsplitter (BS), the polarizing beamsplitter (PBS) and the beam reducer telescope (combination of lenses L_1 and L_2). The reflected beam from the 3-D mirror goes through the beam expander and is focused onto the sample by the objective lens (L_3). Scattered light from the sample retraces the optical path, is descanned by the 3-D mirror, and is then directed by the beam expander, the beamsplitters and the collector lens

(L₄) into a single mode fiber (SMF) with the core aperture of the fiber as the detector pinhole. The quarter wave plate (QWP) changes the polarization orientation of the beam so it can propagate appropriately through the polarizing beamsplitter in the desired direction. Focus control was achieved with a DC voltage (V_F) applied to both the inner and outer focus control electrodes. Biaxial scanning was driven by a four-channel signal mixer/amplifier, which mixes a DC bias with two differential voltages for actuation of x- and y-axis scanning respectively. Refer to Chapter 4 for details of the actuation method.

Imaging Performance Calculation

The theory of confocal microscopy is applied here to calculate the performance of the tabletop confocal microscope to theoretically examine the imaging capability of the 3-D mirror. First, the numerical aperture of the focused beam subtending at the objective lens (L₃) is

$$NA = \frac{Df_2}{2f_1f_3},$$

where D is the usable aperture diameter of the 3-D mirror and f_1 , f_2 and f_3 are the focal lengths of lenses L₁, L₂ and L₃.

To evaluate the lateral and depth resolutions, the Sparrow criterion for resolving two neighboring points and the 3-dB width of the depth response (assume the object is a plane reflector) are used in the following equations [30].

$$d_r(\text{Sparrow}) = \frac{0.5\lambda}{NA} = \frac{\lambda f_1 f_3}{Df_2};$$

$$d_z(3dB) = \frac{0.45\lambda}{1 - \cos \theta_0} \approx \frac{0.9\lambda}{NA^2} = \frac{3.6\lambda f_1^2 f_3^2}{D^2 f_2^2}.$$

The field of view is defined as the area on the focal plane of the objective lens across which the focus can be moved by scanning the 3-D mirror. It can be obtained by ray optics and expressed as

$$FOV = \frac{4f_1f_3\theta_{scan}}{f_2},$$

where θ_{scan} is the zero-to-peak mechanical scan angle of the 3-D mirror.

Similarly, the focus range designates the axial distance over which the focus can be moved by deforming the mirror surface. Using ray optics and considering the effective focal length of the 3-D mirror is given by $f_{mir} = D^2 / 16\delta$, the focus range is given as

$$\Delta z = \frac{16f_1^2f_3^2\delta_{max}}{D^2f_2^2},$$

where δ_{max} is the maximum membrane deflection of the 3-D mirror.

Given the calculations above, the lateral number of resolvable spots and the axial number of resolvable depth-of-focus distances are obtained as

$$N_x = N_y = \frac{FOV}{d_r(Sparrow)} = \frac{4D\theta_{scan}}{\lambda};$$

$$N_z = \frac{\Delta z}{d_z(3dB)} = \frac{4.4\delta_{max}}{\lambda}.$$

The 3-D mirror has an optical pupil diameter $D = 700 \mu\text{m}$, zero-to-peak mechanical scan angle $\theta_{scan} = 5^\circ$ and maximum membrane deflection $\delta_{max} = 3.7 \mu\text{m}$. Given illumination wavelength $\lambda = 0.5 \mu\text{m}$, we obtain $N_x = N_y = 488$ resolvable spots and $N_z = 32$ depth-of-focus distances. It should be noted these two resolution equations are generic for

confocal laser scanning microscopy although they are derived from the specific setup illustrated in Figure 5-2.

Imaging Experiment

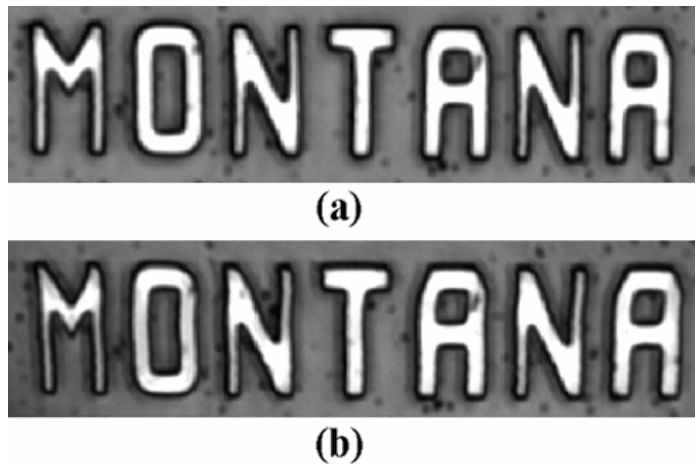


Figure 5-3. Images taken with the CLSM. (a) No focus voltage. (2) 200 volts focus control voltage.

For imaging experiments discussed in this section, the CLSM illustrated in Figure 5-2 was configured with $f_2 / f_1 = 6$ and $f_3 = 20$ mm. Figure 5-3 shows images taken with the CLSM. The size of the word “MONTANA” was about $250 \times 50 \mu\text{m}^2$, which was made up of a patterned gold film on a silicon nitride layer. Figure 5-3 (a) was taken with no voltage applied on the membrane of the 3-D mirror and Figure 5-3 (b) with 200 volts applied, which deflected the membrane center $1.1 \mu\text{m}$ from the initial position corresponding to an effective focal length $f_{mir} = 28$ mm and a shift in focus $\Delta z = 0.4$ mm. In this case the planar sample was translated 0.4 mm closer to the objective lens for the second image to appear in focus. For imaging, the inner axis of the 3-D mirror was

operated with a sinusoidal signal of about 600 Hz while the outer axis with a triangular signal at 2 Hz.

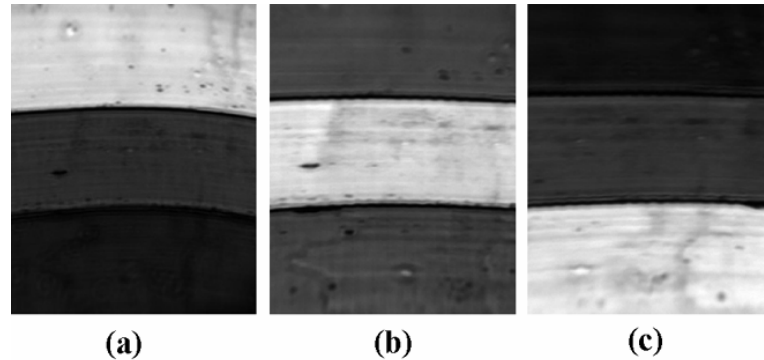


Figure 5-4. Images of a grating with 50 μm high steps taken with the CLSM. (a) Focus on the furthest step. (b) Focus on the middle step. (c) Focus on the nearest step.

In Figure 5-4, a gold-coated grating was imaged with the CLSM to demonstrate the depth discrimination. The grating had a 125 μm pitch with a 50 μm step height. Given $\lambda = 635 \text{ nm}$, $f_2 / f_1 = 6$ and $f_3 = 20 \text{ mm}$, the depth-of-focus $d_z(3dB)$ was about 52 μm and well matched the step height of the grating. The image field-of-view was 350x250 μm^2 , containing three steps of the grating from top to bottom. The top step was furthest from the objective lens and the bottom one was nearest. In Figure 5-4 (a), there was no focus control voltage on the 3-D mirror, thus it worked as a flat mirror and the beam was focused on the furthest step, resulting in an image of white top, gray middle and black bottom. With 85 volts applied on the membrane, the focus of the beam was brought closer to image the middle step, resulting in Figure 5-4 (b). Figure 5-4 (c) was taken with a focus control voltage of 115 volts. The inner axis of the 3-D mirror was operated at

resonance (~ 600 Hz) with sinusoidal signal, and the outer axis was driven with 1 Hz triangular signal, which gave a frame rate of one frame per second. For this imaging demonstration, the lateral mechanical scan range was limited to $\pm 1.5^\circ$ (inner) $\times \pm 1.1^\circ$ (outer), and the membrane maximum displacement was $\delta = 0.3 \mu\text{m}$.

Incorporate the 3-D Mirror into a Miniature Confocal Microscope

An endoscopic confocal laser scanning microscope was presented in Chapter 1. It is one of the target applications of the 3-D mirror and is being developed as an example of incorporating the 3-D mirror into a miniaturized optical instrument. The endoscopic microscope mainly consists of two optical components – the 3-D mirror and the micro objective lens. The 3-D mirror has been described and characterized in detail in previous chapters. To help understand the imaging property of the endoscopic microscope, a brief description of the micro objective lens will be given as follows. A detailed description of design and characterization of this lens was presented by N. El Ferradi [32].

Micro Objective Lens

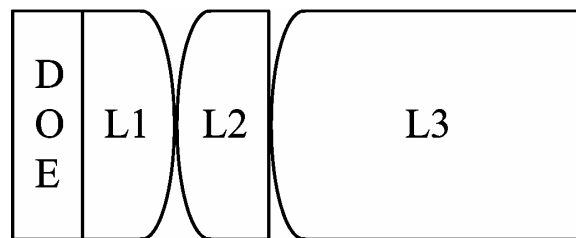


Figure 5-5. Four-element 0.4 NA, 4X, achromatic, water immersion micro objective lens.

The objective lens consists of four elements – one diffractive binary optical element (DOE) and three refractive plano-convex lenses, as illustrated in Figure 5-5.

Lens L1 primarily collimates the laser beam emerging from the single mode fiber while lenses L2 and L3 focus the beam while introducing minimal spherical aberration and coma. The primary function of the diffractive element is to cancel out the chromatic aberration of the plano-convex lenses to produce an achromatic objective lens. The specifications of the four optical elements of the objective lens are listed in Table 5-2.

Table 5-2. Specifications of the four elements of the objective lens.

Lens element	Material	Index of refraction	Diameter/ Tolerance	Thickness/ Tolerance	Radius of curvature/ Tolerance
L1	BK7	1.517	1.600 / - 0.005 mm	0.650 / - 0.005 mm	2.500 / -0.005 mm
L2	BK7	1.517	1.600 / - 0.005 mm	0.650 mm	3.500 / -0.005 mm
L3	LASFN9	1.850	1.600 / - 0.005 mm	2.200 / - 0.005 mm	1.500 / -0.005 mm
DOE	Fused Silica	1.464	1.600 mm	0.500 mm	$\varphi = -591.1r^2 + 174.22r^4$ (phase profile, r is in millimeters).

It is well known that a positive lens focus shorter wavelengths closer to the lens than longer wavelengths due to the normal material dispersion (the index of refraction decreases with wavelength). A common practice to make an achromatic lens is to form a doublet by combining a positive element and a negative element which have opposite signs of chromatic aberration. It is necessary to use two glasses with different dispersion characteristics so that the weaker negative lens can balance the aberration of the stronger positive lens. Another way to balance the chromatic aberration is by using a diffractive

optical element, which is equivalent to a positive lens but has greater focusing power for longer wavelengths, simply because diffraction increases with wavelength. The diffractive element was chosen over a refractive element because it can achieve a more compact and flexible design. In addition, an aspheric phase profile can be defined for the diffractive element to compensate residual spherical aberrations. The miniature confocal microscope was designed to image in bright-field and fluorescence modes with the illumination wavelength at 488 nm. In fluorescence imaging mode, the back-scattered emission wave is 515 nm. Therefore, the diffractive optical element was optimized for 488 nm and 515 nm to ensure that the excitation and emission waves share a common focal point, which is necessary for confocal fluorescent imaging.

The effective focal length of the objective lens is 1.25 mm. Given the configuration of the endoscopic microscope, the objective lens has a numerical aperture of 0.4, a magnification of 4x and a sub-micron spot size for both on-axis and off-axis [32]. The ranges of the mechanical scan angle and the membrane deflection of the 3-D mirror correspond to a field of view of 200 μm and a focus range of 100 μm .

Imaging Experiment

To examine the optical design of the MSU endoscopic confocal laser scanning microscope, a confocal microscope was built using the 3-D mirror and the micro objective lens, as illustrated in Figure 5-6. This demonstration microscope employed the same optical design as the endoscopic microscope, but the 3-D mirror was not inserted into the packaging tube and a ferrule was not used. The optical design and working

principle of the endoscopic microscope was described in Chapter 1 and illustrated in Figure 1-1.

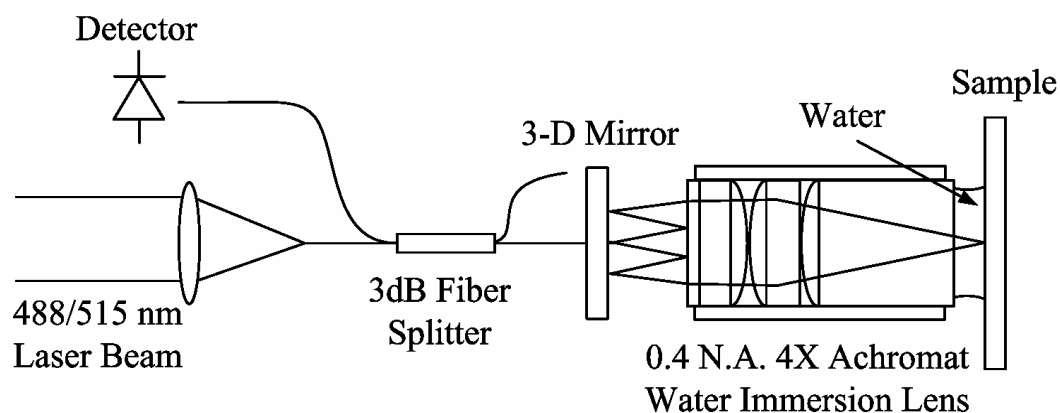
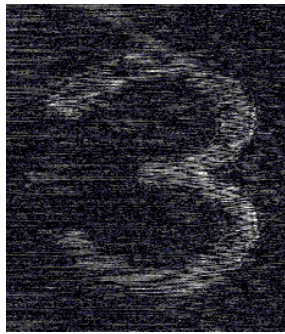


Figure 5-6. Demonstration miniature confocal microscope.

This experiment verified the working principle of the endoscopic microscope. One the other hand, it also exposed some technical problems that must be solved before a useful imaging system can be made using the 3-D mirror and the micro objective lens. One problem was the imperfect alignment of the multiple elements of the micro lens. To ease inserting these elements into the packaging tube, the diameter of the tube was chosen to be slightly larger than those of the lens elements. The downside of this choice was that it made alignment difficult. Another problem was that the lens elements did not have antireflection coatings. With so many air-glass interfaces in the system, back reflections became significant. Both misalignment and back reflections limited the overall optical throughput below 1%. An even worse problem was that the back reflection was much stronger than the signal, thus resulting in an interference image submerged in a strong background. To form a visible image using the interference images, multiple images were taken and superposed according to the following equation.

$$I(x, y) = \frac{1}{N} \sum_{k=1}^N |I_k(x, y) - \overline{I_k}|,$$

where $I_k(x, y)$ is the intensity of the k^{th} interference image; $\overline{I_k}$ is the average intensity across the whole image. The images shown in Figure 5-7 were made using this technique for $N = 1$ and $N = 100$, respectively. The sample was an USAF resolution target, and the field of view of the images was about $100 \times 100 \mu\text{m}^2$.



(a)



(b)

Figure 5-7. Images taken with the miniature confocal microscope. (a) $N = 1$; (b) $N = 100$.

This experiment indicated that misalignment and back reflections of the micro objective lens must be resolved before a useful imaging system can be built. For perfect alignment, a housing tube with tighter size and tolerance must be used. To reduce back reflections, antireflection coatings must be applied to the lens elements. In fluorescence imaging, back reflections may not be a concern because it can be filtered out. Of course, reduced background is definitely an advantage for all cases.

CHAPTER 6

CONCLUSION

Summary of the 3-D Mirror Performance

The MEMS 3-D scan mirror has been successfully fabricated and operated. The overall device size is 1.5 mm, with a usable optical aperture of 700 μm . This novel device incorporates a deformable membrane mirror into the center of a torsional scanning plate, providing biaxial beam scanning and focus control simultaneously with one single optical surface. In other words, this MEMS device is able to move the focus of a laser beam in three dimensions. It is anticipated that optical microsystems needing both beam scanning and focus control will benefit from such a novel technology. With multiple functions combined at one single miniature device, the 3-D mirror technology simplifies design of optical microsystems and results in more compact instrument size.

Confocal laser scanning microscopy is one of many fields to which the 3-D mirror can contribute and is employed as an example to examine and demonstrate the capabilities of the 3-D mirror. Two primary specifications of a confocal microscope are lateral and depth resolutions. The lateral resolution is determined by the maximum scan-angle-mirror-size product, while the depth resolution is determined by the maximum membrane center displacement. Both the inner and outer scanning axes of the torsional plate achieved more than 5° zero-to-peak mechanical scan angles; and the deformable membrane achieved a maximum center displacement of more than 3.7 μm , corresponding to an adjustable focal length from infinity to approximately 8 mm. For a confocal laser

scanning microscope with illumination wavelength at 500 nm, we calculate $N_x = N_y = 488$ resolvable spots for lateral resolution, and $N_z = 32$ depth-of-focus distances for depth resolution. To drive the 3-D mirror, the inner axis is operated near resonance (~ 650 Hz) by a sinusoidal signal; while the outer axis is quasi-statically (e.g., 2 Hz) by a sawtooth signal. This will provide a line resolution of 325 lines/frame at a refresh rate of 2 frames/second. Considering the optical resolution discussed above, a frame resolution of 488x325 pixels is achieved. The resulting performance characteristics of the 3-D mirror are well matched to the intended application – the MSU endoscopic confocal laser scanning microscope, and similar devices could prove useful in a variety of optical microsystems needing beam pointing and focus control.

In addition to beam scanning and focus control, the 3-D mirror can also compensate residual spherical aberration in the optical system. The deformable membrane employs two concentric annular actuation electrodes, which provides two degrees of freedom to control the surface shape of the mirror. Himmer has shown that the two-zone actuation is able to provide a spherical aberration correction up to 4 waves at 500 nm illumination [22].

The thin-film deformable membrane puts limitations on high speed scanning because dynamic inertial forces may distort the membrane to introduce optical aberrations. Assuming 500 nm illumination and maximum membrane distortion of $\lambda/8$ ($\lambda/4$ optical aberration), the maximum scan frequency is limited to 9100 Hz for the 3-D mirror. Higher scan frequency can be achieved with thicker silicon nitride film or higher residual stress.

Future Work

Design and Process Variations for Mirror Performance Improvement

Experimental characterization and imaging demonstration have verified the operating principle of the 3-D mirror and manifested its potential applications in optical microsystems needing both focus control and beam scanning. Variations in geometries, materials, process techniques enable implementation of 3-D mirrors suitable for a variety of optical instruments needing different mirror specifications. Improvements in mirror performance can also be achieved by varying the design and process parameters. Generally speaking, larger scan angles, higher resonant frequency of the inner axis, larger membrane deflection range and lower actuation voltage are desired.

Silicon nitride film thickness and residual stress play important roles in the behavior of the torsional plate and that of the deformable membrane. The torsional plate may benefit from thicker silicon nitride film and higher residual stress, which results in higher scanning frequencies. On the other hand, the deformable membrane may want thinner silicon nitride film and lower residual stress to lower the actuation voltage. The current design of the 3-D mirror employs a uniform silicon nitride film across the whole device. Its thickness and residual stress were chosen as a compromise of the two contradictory requirements. A two-step silicon nitride deposition may be employed to optimize the deformable membrane and the torsional hinges separately. The first silicon nitride layer can be chosen according to the requirements of the deformable membrane. A second silicon nitride layer overlying on the first layer may be added to increase the thickness of the torsional hinges.

Another problem observed was that the focus control voltage affected the initial tilt angle, mostly about the outer axis. This problem became significant when the focus control voltage was over 200 volts. This problem was caused by the asymmetric disposition of metal traces on the focus-control electrode layer, leading to an asymmetric electrostatic field and an attendant torque on the gimbal ring. This can be resolved with careful re-routing of those traces.

Packaging the Endoscopic Confocal Microscope

The 3-D mirror was demonstrated along with the micro objective lens to examine the optical design of the MSU endoscopic confocal laser scanning microscope. This experiment verified the working principle of the endoscopic microscope. However, a packaging solution must be developed before the endoscopic microscope can be built using the 3-D mirror and the micro objective lens.

To house the 3-D mirror into the packaging tube, it is mounted on a customized ferrule/carrier. The customized ferrule is used to hold the single mode fiber and carry the mirror. Metal electrodes and traces are made on the ferrule to provide electrical actuation of the mirror. Figure 6-1 shows a rendering of the 3-D mirror and the ferrule. The ferrules that are currently used were manufactured by InnovaQuartz, Inc. They were produced by fusing two quartz tubes. The inner tube has an inner diameter of 126 μm and an outer diameter of 1200 μm ; the outer tube 1200 μm and 1600 μm . By inserting the inner tube into the outer one and displacing them by 150 μm , a sink on one end is created. The flat side of the ferrule was made by polishing. To make electrodes and traces on a ferrule, chrome and gold were first sputtered on it, and then were patterned by photolithography

and wet etching. Patterning metal on such a structure is a challenge since two perpendicular sides are to be processed and the end has a sink structure (rather than a flat surface). InterVia 3D-P electrodeposited resist was used to pattern the ferrules. Figure 6-2 shows images of a patterned ferrule. In patterning, chippings in the surface caused by polishing made the patterning yield very low. Another problem is that the narrow tracks on the flat side make subsequent cabling rather difficult.

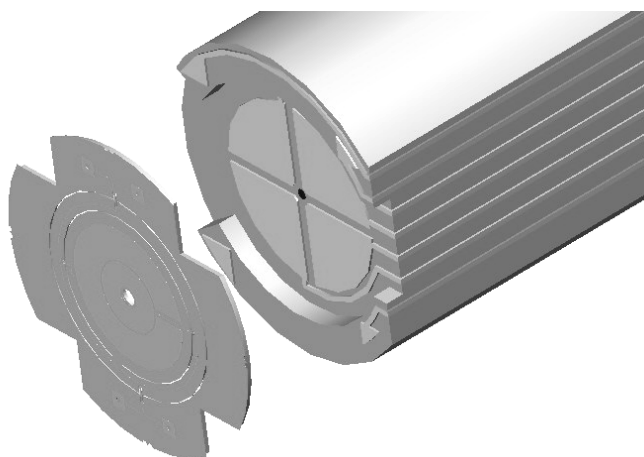
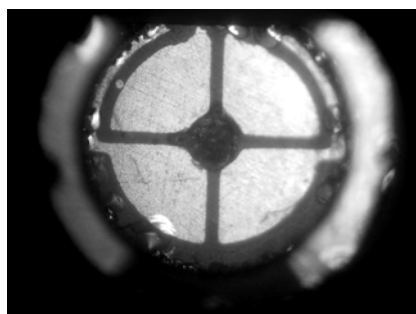
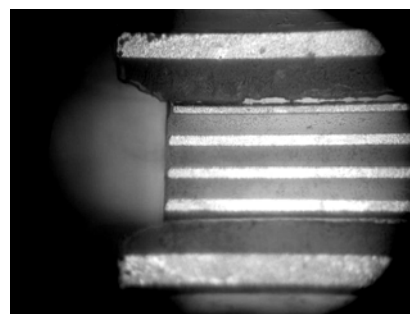


Figure 6-1. Rendering of the 3-D mirror and the ferrule/carrier.



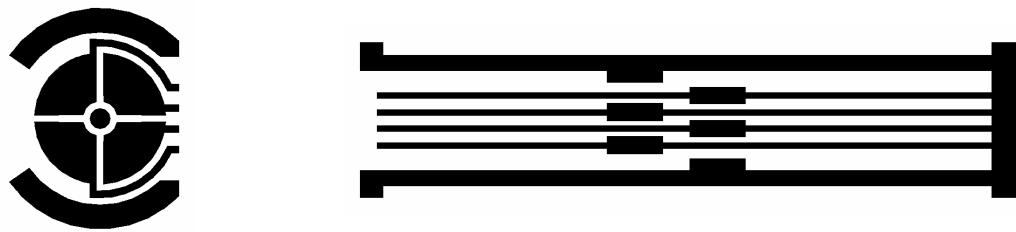
(a)



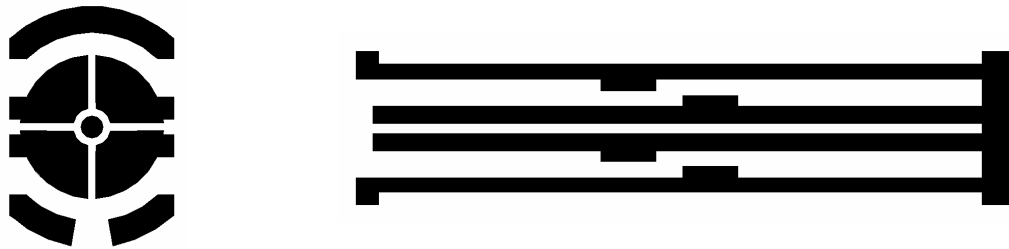
(b)

Figure 6-2. A ferrule with gold electrodes and traces. (a) The mirror carrier end; (b) The flat side.

Other materials (e.g. ceramic) and production technologies might be used to build ferrules with higher quality. Ferrules might also be machined with two flat sides to reduce difficulties in patterning electrodes. Two-flat-side design removes the two thin tracks on the perimeter in the sink and makes other tracks much wider. Figure 6-3 shows the current and proposed new photo masks for patterning ferrules.



(a) Current photo masks for patterning ferrules.



(b) New photo masks for patterning ferrules.

Figure 6-3. Current and new photo masks for patterning ferrules.

Another challenge in packaging the endoscopic confocal microscope is alignment of multiple elements of the micro objective lens and the 3-D mirror. To ease inserting elements into the housing tube, it was chosen to be slightly larger. However, the demonstration miniature microscope indicated tighter tolerance is needed. Back reflections from air-glass interfaces of the objective lens interfere with the image light. They can be minimized by applying antireflection coatings on the glass elements.

Potential Applications

This dissertation mainly considers using the MEMS 3-D mirrors for confocal laser scanning microscopy. However, beam scanning and focus adjustment are common needs to many optical microsystems. Similar devices can be designed for many different applications. For example, so-called 3-D optical switch architectures have a different pathlength between fibers depending on which fiber is addressed [10]. A variable-focus element could allow optimization of coupling for each configuration of the switch. Optical disk read/write heads armed with both beam scanning and focus control are able to access multiple layers of the storage-media. The performance of scanned-beam display systems can be improved by MEMS scanners with added focus adjustment.

In addition to confocal microscopy, optical coherence tomography (OCT) is another example of non-invasive diagnostic technique for examining biological systems *in-situ*. Standard OCT scheme based on a low time-coherence Michelson interferometer (LCI) employs separate lateral scan and depth scan [39]. A MEMS 3-D mirror might be used to miniaturize the instrument. Focus adjustment may also improve the performance of its fixed focal length imaging system.

REFERENCES CITED

- [1] D. W. Wine, M. P. Helsel, L. Jenkins, H. Urey, and T. D. Osborn, "Performance of a biaxial MEMS-based scanner for microdisplay applications," Proc. SPIE, Vol. 4178, pp. 186-196, 2000.
- [2] M. Liang, "Performance characterization of a single bi-axial scanning MEMS mirror based head-worn display," Proc. SPIE, Vol. 4773, July 2002.
- [3] H. Urey, "Torsional MEMS scanner design for high-resolution scanning display systems," Proc. SPIE, Vol. 4773, pp. 27-37, 2002.
- [4] D. Dickensheets and G. Kino, "Silicon-micromachined scanning confocal optical microscope," IEEE J. Microelectromechanical Systems, Vol. 7, No. 1, pp. 38-47, March 1998.
- [5] D. Dickensheets, P. Himmer, R. Friholm, and J. Lutzenberger, "Miniature high-resolution imaging system with 3-dimensional MOEMS beam scanning for Mars exploration," Proc. SPIE, Vol. 4178, pp. 90-97, Sept. 2000.
- [6] H. Miyajima, K. Murakami, and M. Katashiro, "MEMS optical scanners for microscopes," IEEE J. Selected Topics in Quantum Electronics, Vol. 10, No. 3, pp. 514-527, May/June 2004.
- [7] I. Watanabe, Y. Ikai, T. Kawabe, H. Kobayashi, S. Ueda, J. Ichihara, and Y. Nakamura, "Precise track-following control using a MEMS tracking mirror in high-density optical disk drives," Jpn. J. Appl. Phys., Vol. 42, Part 1, No. 2B, pp. 904-907, Feb. 2003.
- [8] M.-H. Kiang, O. Solgaard, K. Y. Lau, and R. S. Muller, "Electrostatic combdrive-actuated micromirrors for laser-beam scanning and positioning," J. Microelectromechanical Systems, Vol. 7, No. 1, pp. 27-37, March 1998.
- [9] J. J. Bernstein, W. P. Taylor, J. D. Brazzle, C. J. Corcoran, G. Kirkos, J. E. Odhner, A. Pareek, M. Waelti, and M. Zai, "Electromagnetically actuated mirror arrays for use in 3-D optical switching applications," J. Microelectromechanical Systems, Vol. 13, No. 3, pp. 526-535, June 2004.
- [10] R. Helkey, J. Bowers, O. Jerphagnon, V. Kaman, A. Keating, B. Liu, C. Puserla, D. Xu, S. Yuan, X. Zheng, S. Adams, and T. Davis, "Design of large, MEMS-based photonic switches," Optics and Photonics News, Vol. 13, No. 5, pp. 40-43, May 2002.

- [11] C.-H. Ji, Y. Yee, J. Choi, S.-H. Kim, and J.-U. Bu, "Electromagnetic 2 x 2 MEMS optical switch," *IEEE J. Selected Topics in Quantum Electronics*, Vol. 10, No. 3, pp. 545-550, May/June 2004.
- [12] P. B. Chu, S.-S. Lee, S. Park, M.-J. Tsai, I. Brener, D. Peale, R. A. Doran, and C. Pu, "MOEMS: enabling technologies for large optical cross-connects," *Proc. SPIE*, Vol. 4561, pp. 55-65, Oct. 2000.
- [13] H. Schenk, P. Durr, D. Kunze, H. Lakner, and H. Kuck, "An electrostatically excited 2D-micro-scanning-mirror with an in-plane configuration of the driving electrodes," *Proc. IEEE, Thirteenth Annual International Conference on Micro Electro Mechanical Systems*, pp. 473-478, 2000.
- [14] T. Kiessling, A. Wolter, H. Schenk, and H. Lakner, "Bulk micro machined quasistatic torsional micro mirror," *Proc. SPIE*, Vol. 5348, pp. 211-220, Jan. 2004.
- [15] J. Lutzenberger and D. Dickensheets, "Vertical stiffening members for flatness control of surface-micromachined structures," *Proc. SPIE*, Vol. 4561, pp. 238-246, Oct. 2001.
- [16] T. Kaiser, J. Lutzenberger, R. Friholm, P. Himmer, and D. Dickensheets, "Silicon nitride biaxial pointing mirrors with stiffening ribs," *Proc. SPIE*, Vol. 4561, pp. 276-282, Oct. 2001.
- [17] G. Vdovin, D. W. de Lima Monteiro, O. Akhzar-Mehr, S. Sakarya, O. Soloviev, and P. M. Sarro, "Silicon micro-optics for smart light," *Proc. SPIE*, Vol. 5348, pp. 135-149, Jan. 2004.
- [18] D. Dayton, S. Restaino, J. Gonglewski, J. Gallegos, S. McDermott, S. Browne, S. Rogers, M. Vaidyanathan, and M. Shilko, "Laboratory and field demonstration of a low cost membrane mirror adaptive optics system," *Optics Communications*, Vol. 176, pp. 339-345, 2000.
- [19] O. Albert, L. Sherman, G. Mourou, T. Norris, and G. Vdovin, "Smart microscope: an adaptive optics learning system for aberration correction in multiphoton confocal microscopy," *Optics Letters*, Vol. 25, No. 1, pp. 52-54, 2000.
- [20] F. Gonte, A. Courteville, and R. Dandliker, "Optimization of single-mode fiber coupling efficiency with an adaptive membrane mirror," *Optical Engineering*, Vol. 41, No. 5, pp. 1073-1076, 2002.
- [21] P. Himmer, D. Dickensheets, and R. Friholm, "Micromachined silicon nitride deformable mirrors for focus control," *Optics Letters*, Vol. 26, No. 6, Aug. 2001.

- [22] P. Himmer, "Silicon nitride deformable mirrors for focus and spherical aberration correction in micro-optical systems," Doctoral Dissertation, Montana State University, Bozeman, MT, Nov. 2002.
- [23] M. Sheplaak and J. Dugundji, "Large deflections of clamped circular plates under initial tension and transitions to membrane behavior," *J. Applied Mechanics*, Vol. 65, pp. 107-115, March 1998.
- [24] R. Friholm, "Silicon nitride membrane mirrors for focus control," M.S. Thesis, Montana State University, Bozeman, MT, 2001.
- [25] V. Mahajan, "Aberration theory made simple," SPIE Optical Engineering Press, Vol. TT6, 1991.
- [26] K. Williams and R. Muller, "Etch rates for micromachining processing," *IEEE J. Microelectromechanical Systems*, Vol. 5, No. 4, 1996.
- [27] J. Buhler, F. P. Steiner, and H. Bates, "Silicon dioxide sacrificial layer etching in surface micromachining," *J. Micromechanical Microengineering*, Vol. 7, pp. R1-R13, 1997.
- [28] W. H. Press, B. P. Flannery, S. A. Teukolsky, and W. T. Vetterling, "Numerical recipes in FORTRAN: The art of scientific computing," 2nd Ed., Cambridge University Press, 1992.
- [29] D. Malacara, M. Servin, and Z. Malacara, "Interferogram analysis for optical testing," New York: Marcel Dekker, 1998.
- [30] T. Corle and G. Kino, "Confocal scanning optical microscopy and related imaging systems," Academic Press, 1996.
- [31] T. Wilson and C. Sheppard, "Theory and practice of scanning optical microscopy," Academic Press, 1984.
- [32] N. El Ferradi, "Objective lens for a miniature endoscopic confocal microscope," M.S. Thesis, Montana State University, Bozeman, MT, 2005.
URL: http://www.montana.edu/etd/available/unrestricted/El_Ferradi_0505.pdf
- [33] W. C. Young, "Roark's formulas for stress and strain," 6th Ed., McGraw-Hill, 1989.
- [34] T.-S. Lim, C.-H. Ji, C.-H. Oh, H. Kwon, Y. Yee, and J. U. Bu, "Electrostatic MEMS variable optical attenuator with rotating folded micromirror," *IEEE J. Selected Topics in Quantum Electronics*, Vol. 10, No. 3, pp. 558-562, May/June 2004.

- [35] D. T. Neilson, H. Tang, D. S. Greywall, N. R. Basavanhally, L. Ko, D. A. Ramsey, J. D. Weld, Y. L. Low, F. Pardo, D. O. Lopez, P. Busch, J. Prybyla, M. Haueis, C. S. Pai, R. Scotti, and R. Ryf, "Channel equalization and blocking filter utilizing microelectromechanical mirrors," *IEEE J. Selected Topics in Quantum Electronics*, Vol. 10, No. 3, pp. 563-569, May/June 2004.
- [36] F. Oohira, M. Iwase, T. Matsui, M. Hosogi, I. Ishimaru, G. Hashiguchi, Y. Mihara, and A. Iino, "Self-hold and precisely controllable optical cross-connect switches using ultrasonic micro motors," *IEEE J. Selected Topics in Quantum Electronics*, Vol. 10, No. 3, pp. 551-557, May/June 2004.
- [37] R. M. Goldstein, H. A. Zebker, and C. L. Werner, "Satellite radar interferometry: two-dimensional phase unwrapping," *Radio Science*, Vol. 23, No. 4, pp. 713-20, July-Aug. 1988.
- [38] P. J. Brosens, "Dynamic mirror distortions in optical scanning," *Applied Optics*, Vol. 11, pp. 2988-2989, 1972.
- [39] A. F. Fercher, W. Drexler, C. K. Hitzenberger, and T. Lasser, "Optical coherence tomography—principles and applications," *Reports on Progress in Physics*, Vol. 66, pp. 239–303, 2003.
- [40] D. Dickensheets, P. Ashcraft, and P. Himmer, "Pixel-by-pixel aberration correction for scanned-beam micro-optical instruments," *Proc. SPIE*, Vol. 3878, pp. 48-57, Sept. 1999.
- [41] K. Creath, "Calibration of numerical aperture effects in interferometric microscope objectives," *Applied Optics*, Vol. 28, No. 15, pp. 3333-3338, Aug. 1989.
- [42] W. Alexander and J. F. Shackelford, "CRC materials science and engineering handbook," 3rd Ed., CRC Press, Dec. 2000.
- [43] E. Wong, N. Latta, H. Parmar, R. Kaur, and J. McVittie, "Low stress nitride," <http://snf.stanford.edu/Equipment/tylanlpcvd/LowStressNitride.pdf>
- [44] Y. Shao and D. Dickensheets, "MOEMS 3-D scan mirror for single-point control of beam deflection and focus," *SPIE J. Microlith., Microfab., Microsyst.*, Vol. 4, No. 4, Oct.-Dec. 2005.
- [45] Y. Shao, D. Dickensheets, and P. Himmer, "3-D MOEMS mirror for laser beam pointing and focus control," *IEEE J. Selected Topics in Quantum Electronics*, Vol. 10, No. 3, pp. 528-535, May-June 2004.
- [46] Y. Shao and D. Dickensheets, "MEMS three-dimensional scan mirror," *Proc. SPIE*, Vol. 5348, pp. 175-183, Jan. 2004.

[47] Y. Shao and D. Dickensheets, "MEMS 3D mirror for confocal laser scanning microscopy," 2004 IEEE/LEOS International Conference on Optical MEMS, Takamatsu, Kagawa, Japan, pp. 216-217, Aug. 2004.